Application of Reaction-Diffusion Manifolds (REDIM) for the Simulation of Laminar Diffusion Flames

Zur Erlangung des akademischen Grades eines
DOKTORS DER INGENIEURWISSENSCHAFTEN (Dr.-Ing)

von der KIT-Fakultät für Maschinenbau des
Karlsruher Instituts für Technologie (KIT)
genehmigte

DISSERTATION

von

M.Sc. Ningyi Li

Tag der mündlichen Prüfung:	26.03.2024
Hauptreferent:	Prof. Dr. rer. nat. habil. Ulrich Maas
Korreferent:	Prof. Dr.-Ing. Henning Bockhorn

Acknowledgements

During the process of completing this dissertation, I received a lot of help from many people, including my supervisors, colleagues, and family. I would like to sincerely thank them for their assistance.

In the first place, I am deeply grateful to my supervisor Prof. Dr. rer. nat. habil. Ulrich Maas, whose guidance, encouragement, and support have been invaluable throughout my doctoral time. His passion for combustion theory has ignited a similar flame in me. I am grateful for the inspiration and motivation that he has provided. His expertise, interest, and dedication have challenged me to grow both personally and academically, and I am fortunate to have had such a committed and inspiring advisor.

The research was carried out in the Institute of Technical Thermodynamics (ITT) of the Department of Mechanical Engineering of Karlsruhe Institute of Technology (KIT). I would like to express my gratitude to all the members of ITT KIT for creating a enjoyable and positive atmosphere. Special thanks for the in-depth discussion with PD. Dr. Viatcheslav Bykov and Dr.-Ing. Robert Schiessl on combustion. Many thanks to Dr. Chunkan Yu, Dr. Christina Strassacker, and Dr. Prashant Shrotriya for the discussion of REDIM. Additionally, I would like to thank Dr. Thorsten Zirwes from SCC KIT for the great help in the EBIdnsFoam solver.

There are also many people outside the university to whom I want to appreciate. Especially thank my parents, who have always believed in me and supported me. Finally, thank you all for your contributions towards helping me attain this significant milestone in my academic career.

Abstract

The time scales of chemical reactions involved in combustion processes typically span several orders of magnitude. The implementation of detailed reaction mechanisms in combustion simulations generally introduces a large number of species conservation equations and nonlinear chemical source terms, which leads to stiffness of the governing equation systems and prohibitive computational cost. Therefore, there is a need for reduced kinetic models to simplify computation. In the last few decades, several reduction methods have been developed to simplify the description of the reaction mechanism in order to reduce computational costs. Among these methods, the reaction-diffusion manifolds (REDIM) method is a reduction model that takes into account the coupling of molecular diffusion and chemical reaction to reduce computing time, and can be implemented in different combustion simulations.

The REDIM method offers two significant advantages: It requires little knowledge of the chemical kinetics about the combustion in the generation of REDIM, and the REDIM model encompasses both steady and transient processes (e.g., ignition and extinction). In this work, the REDIM method using generalized and physical coordinates is implemented within the OpenFOAM framework. The REDIM reduced chemistry is used for the first time to investigate local extinction, flame liftoff, fuel leakage, flame dynamic and alterations of soot precursors in response to flow oscillations across a wide frequency range.

The main focus of this thesis is to validate the performance of REDIM reduced chemistry in simulating combustion phenomena. The REDIM method is applied in calculations of 2D counterflow/jet flames. Compared with the results of detailed mechanism, the REDIM reduced chemistry can reproduce the respective system dynamics of different combustion systems very well. Furthermore, the REDIM method has the significant advantage to reduce the computational cost by one order of magnitude compared to the detailed simulations.

Kurzfassung

Die Zeitskalen chemischer Reaktionen, die an Verbrennungsprozessen beteiligt sind, umfassen typischerweise mehrere Größenordnungen. Die Implementierung detaillierter Reaktionsmechanismen in Verbrennungssimulationen führt im Allgemeinen zu einer großen Anzahl von Artenerhaltungsgleichungen und nichtlinearen Termen chemischer Quellen, was zu einer Steifheit der maßgeblichen Gleichungssysteme und zu unerschwinglichen Rechenkosten führt. Daher besteht ein Bedarf an reduzierten kinetischen Modellen, um die Berechnung zu vereinfachen. In den letzten Jahrzehnten wurden mehrere Reduktionsmethoden entwickelt, um die Beschreibung des Reaktionsmechanismus zu vereinfachen und den Rechenaufwand zu senken. Unter diesen Methoden ist die REDIM-Methode (Reaction-Diffusion Manifolds) ein Reduktionsmodell, das die Kopplung von molekularer Diffusion und chemischer Reaktion berücksichtigt, um die Rechenzeit zu reduzieren, und in verschiedenen Verbrennungssimulationen implementiert werden kann.

Die REDIM-Methode bietet zwei wesentliche Vorteile: Sie erfordert nur geringe Kenntnisse über die chemische Kinetik der Verbrennung bei der Erzeugung von REDIM, und das REDIM-Modell umfasst sowohl stationäre als auch transiente Prozesse (z. B. Zündung und Flammenlöschung). In dieser Arbeit wird die REDIM-Methode unter Verwendung verallgemeinerter und physikalischer Koordinaten innerhalb des OpenFOAM-Frameworks implementiert. Die reduzierte REDIM-Chemie wird zum ersten Mal verwendet, um lokale Extinktion, Flammenabheben, Kraftstoffleckage, Flammendynamik und Veränderungen von Rußvorläufern als Reaktion auf Strömungsoszillationen über einen weiten Frequenzbereich zu untersuchen.

Der Schwerpunkt dieser Arbeit liegt auf der Überprüfung der Leistungsfähigkeit der REDIM-reduzierten Chemie bei der Simulation von Verbrennungsphänomenen. Die REDIM-Methode wird bei Berechnungen von 2D-Gegenstrom-/Jet-Flammen angewendet. Im Vergleich zu den Ergebnissen detaillierter Mechanismen kann die REDIM-reduzierte Chemie die jeweilige Systemdynamik verschiedener Verbrennungssysteme sehr gut reproduzieren. Darüber hinaus hat die REDIM-Methode den erheblichen Vorteil, dass sie den Rechenaufwand im Vergleich zu detaillierten Simulationen um eine Größenordnung reduziert.

Contents

1 Introduction

1.1 Background and motivation

Replacing fossil fuels (e.g. oil, natural gas, coal, etc.) with renewable energy carriers is the foremost imperative of our time in order to mitigate global warming. Despite the emerging technologies for utilizing renewable energy, further improvement is required before its full potential can be realized. Consequently, combustion will continue to play a significant role in energy provision for the next 20-30 years [1]. Currently, more than 80 % of the world's primary energy is provided by burning fossil fuels, according to the report of British Petroleum [2]. Figure 1.1 shows the share of fossil fuels in worldwide primary energy consumption in 2019 (the first column of the bar chart) and prediction in 2050 (1 EJ = 10^{18} Joules). In the figure, the "Accelerated", "Net Zero", and "New Momentum" columns represent the three primary scenarios that include a broad range of potential outcomes during the world transitions to a lower-carbon energy system over the next three decades. These three scenarios represent three different levels of carbon emission policies to be implemented over the next 30 years, resulting in varying total energy consumption in the future.

For a long time, researchers have mainly used experimental research to study the combustion process, therefore, combustion was basically an experimental science [3]. Although combustion theory was still limited to describe basic phenomena, as well as its qualitative analysis in 1970s, numerical simulation of combustion process has gradually developed and become a powerful tool to develop the combustion technology and guide the design of combustion devices with the rapid development of computer technology in the past several decades [4–6]. Combustion is a complex process controlled by a variety of physical and chemical factors, which is an interdisciplinary subject involving many research fields [7]. To describe the combustion process, scientists and researchers have proposed numerous theoretical models based on different methods. These theoretical models can be solved through numerical simulations. The numerical solutions of the models can be compared with the corresponding experimental results, and the results can then be used to further

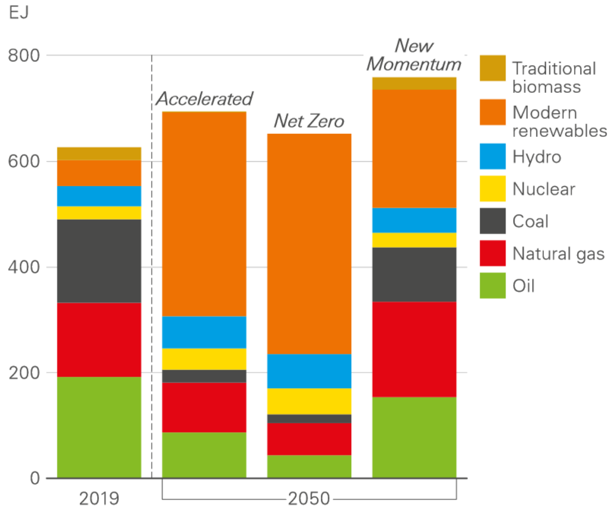

Figure 1.1: Primary energy consumption in 2019 and prediction in 2050 [2].

test, develop, and optimize these theoretical models [8]. At the same time, the theoretical models can also investigate the characteristics of the combustion process, predict new combustion phenomena, and deeply reveal the nature of combustion. In this way, scientific theory and the actual combustion process can be linked, representing a new method of using theory as a direct guide to combustion experiment and burner design, thereby reducing the cost of the experiments and the workload of engineering design [6].

As combustion research progresses, the role of numerical simulation in this field is becoming increasingly significant [9]. Owing to the intricate nature of the combustion process, although physical and mathematical models of the process and corresponding numerical calculation methods and techniques for turbulent flow, heat and mass transfer, chemical reaction, multiphase flow, pollutant generation, etc., have been developed in the past decades, these models still represent an approximation and simplification of the real combustion processes based on various viewpoints and aspects, that cannot fully solve the actual combustion problems in engineering [10–13]. Therefore, considering the importance of numerical simulation, it is necessary to further develop combustion models with better performance, which can promote the development of combustion technology and serve the technical practice. From this point of view, combustion, especially numerical combustion, remains a promising discipline. Furthermore, combustion is fascinating in that it integrates all of the thermal sciences nicely, as well as bringing chemistry into the engineering practice [12].

Numerical simulation of various physical processes, e.g. fluid flow and heat transfer, aerodynamics and flight tests, combustion and radiation, etc., can be divided into three groups:

- Direct Numerical Simulation (DNS) directly solves the Navier-Stokes equations and is able to resolve the smallest eddies and time scales of turbulence in the flow without introducing any models [14]. Although the DNS has a high solution accuracy, its computational cost is very expensive due to the very fine grids and small time steps.

- Large Eddy Simulation (LES) is a numerical calculation method widely used in industrial applications. LES can resolve most of the turbulent kinetic energy of turbulence, and only needs to simulate the small turbulent scales [15]. This means that it has relatively high accuracy and the computational cost is less than DNS.

- Reynolds-averaged Navier-Stokes (RANS) [7, 16] method are time-averaged equations to model the motion for fluid flow, which is a technique with lower computational cost than LES. However, the RANS method sometimes cannot meet the required accuracy for simulations of complicated flow patterns, such as swirling flows, breakdowns of large-scale vortical structures, and pollutants [17].

This thesis mainly focuses on the comparison of laminar flames calculated with detailed and reduced mechanisms at low Reynolds numbers. Considering its high solution accuracy and the absence of any introduced models, DNS is employed for the corresponding calculations in this work.

The time scales of chemical reactions in combustion processes often vary widely, spanning several orders of magnitude [7]. The implementation of detailed mechanism in the simulation of combustion introduces generally a large number of species conservation equations (sometimes exceeding 1000 species equations) and nonlinear chemical source terms, which leads to stiffness of the governing equation system and prohibitively computational cost. Figure 1.2 shows the size of detailed and reduced mechanisms for selected hydrocarbon fuels. It can be seen that the number of species and reactions increase with the size of fuel molecules, generally increasing in an exponential trend [18]. To give a particular example, the detailed combustion mechanism of methyl decanoate (a biomass fuel substitute) involves 3036 species and 8555 reactions [19]. The computational cost of using this mechanism is prohibitive. Therefore, in order to reduce the computational cost, many methods, for example, sensitivity analysis [20], Jacobian analysis [21] and principal component analysis [22] etc., are used to reduce the reaction mechanisms. Furthermore, there exists another category of techniques that rely on invariant manifolds to simplify the reaction mechanisms, such as intrinsic low-dimensional manifolds (ILDM) [23], flamelet generated manifolds (FGM) [24], method of invariant manifold (MIM) [25], flame prolongation of ILDM (FPI) [26] and reaction-diffusion manifolds (REDIM) [27].

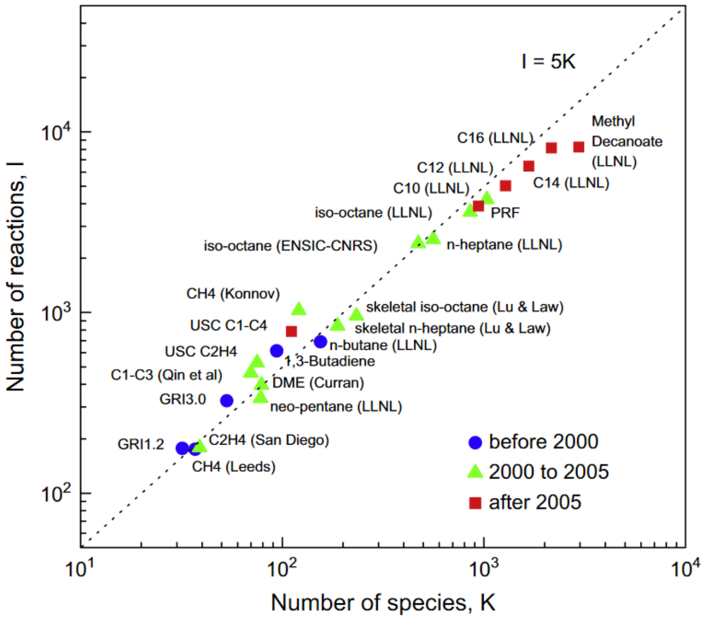

Figure 1.2: Size of detailed and reduced mechanisms for selected hydrocarbon fuels [18].

In contrast to other reduction approaches (e.g. ILDM or MIM), REDIM applies the concept of invariant manifolds while taking into account the coupling of molecular transport and chemical reaction processes. The REDIM is a general method for reducing reaction mechanisms, which can be implemented in different combustion scenarios. In previous work [28–34], the REDIM method was assessed for use in different flame configurations such as premixed flames, steady and transient counterflow flames and turbulent flames. The results show very good agreement with detailed computations and experimental measurements. Therefore, in the thesis, the REDIM method as the simplified mechanism is used to perform corresponding calculations.

The counterflow flame configuration [7] is extensively employed in numerical combustion studies to assess the accuracy of mathematical models. In practical devices, the study of counterflow flames is a three-dimensional (3D) problem, however 3D simulation needs higher computational cost. Therefore, this problem can be simplified to a two-dimensional (2D) flame based on the symmetry of laminar counterflow flame. An important objective of this thesis is to evaluate the performance of the REDIM method by studying a 2D axisymmetric laminar counterflow diffusion flame. Jet diffusion flame [12] is a versatile flame configuration that can be applied to a wide range of practical combustion devices, including gas turbines and commercial burners. Their significance lies in their ability to elucidate the interplay between complex transport phenomena and detailed chemical reactions, making it a valuable tool for modelling turbulent reacting flows, studying flow-thermochemistry interaction, and gaining insights into the generation of pollutants, etc.

One phenomenon present in jet flames is that if the exit velocity is sufficiently high, the jet flame will be lifted from an attached position at the nozzle. The liftoff height is the shortest distance between the burner exit and the flame front, and it will increase as the inlet velocity of the nozzle is raised until the flame eventually blows off [12, 35]. In practical burners, flame liftoff typically needs to be avoided for various reasons. First, it may result in unburnt fuel leakages or incomplete combustion; and when flame liftoff exceeds the limit, fuel mixture will become difficult to ignite; Precisely controlling the location of a lifted flame is challenging, often leading to worse heat-transfer characteristics; moreover, lifting flame can generate noise [12, 36]. Therefore, in the design of practical burners, blowoff limits are an important design criterion . Extensive research has been conducted on the lifting phenomenon of jet flames, and Refs. [35, 37] summarized three different theories to explain this phenomenon and to establish the liftoff height:

- Theory 1:
  The local velocity in the flow at the point where the laminar flame speed reaches its maximum is equal to the local laminar flame speed of a premixed flame, i.e., $v(s_{\mathrm{L,max}}) = s_{\mathrm{L}}$ [38, 39].

- Theory 2:
  The local strain rates in the flow is larger than the extinction strain rate in a laminar diffusion flame, i.e. $a > a_{\mathrm{extinction}}$ [40, 41].

- Theory 3:
  The ratio of the time (t_{mixing}) associated with the mixing of hot products into fresh mixture and the critical chemical time (t_{critical}) required for ignition is less than some critical value ϵ, i.e., $\frac{t_{\mathrm{mixing}}}{t_{\mathrm{critical}}} < \epsilon$ [42].

Time-varying laminar jet flames serve as a means of exploring the intricate interplay between chemical reactions and fluid flow, effectively bridging the gap between laminar and turbulent combustion. Furthermore, research has been conducted to examine the disparities in soot formation between steady-state and oscillating flames. Results from both experimental measurements and calculations have shown that soot production can be four to five times greater in an oscillating flame than in a steady flame with the same average mass flow rate [43–46].

1.2 Objectives of this study

The main focus of this thesis is to use the REDIM reduced chemistry in simulating steady and non-steady laminar premixed and diffusion flames. Firstly, the REDIM table is established based on various combustion scenarios (section 3.3.7). The REDIM method in generalized and physical coordinates is applied in OpenFOAM. The accuracy of REDIM is evaluated by comparing the results of the detailed mechanism with those obtained from the REDIM method with two different coordinate calculations, in order to interpret the influence of coordinate selection (section 4.3).

The investigation also encompasses analyzing the impact of various factors under steady conditions, such as mesh sizes, progress variables, reaction mechanisms, and global strain rates, on the precision of REDIM. In addition to comparing results in steady state, it is also interesting to evaluate how REDIM performs under non-steady state conditions, such as extinction, while the standard flamelet method necessitates incorporating an additional extinction regime to simulate this process.

Simplified mechanisms significantly reduce computational effort, enabling the practical handling of more intricate burner systems. This thesis investigates whether the REDIM reduced chemistry can serve as an efficient tool for flame simulations in such complex combustion systems. Challenges such as flame lifting and fuel leakage often occur in complex combustion systems, and additional research is required to determine whether the REDIM method can provide an accurate description of these phenomena. Time-varying laminar jet flames bridge the gap between laminar and turbulent combustion, and dramatically increase soot formation. This thesis explores the application of REDIM in effectively capturing the variation of flame structure induced by fuel flow oscillation across a wide frequency range and predicting soot precursor formation in the oscillating flame. Moreover, we investigate the relationship between perturbation amplitude and frequency-dependent dissipative processes.

The main goal of using reduction methods is to decrease the computational effort required for combustion while preserving a high level of accuracy. This would allow for the handling of more intricate and practical engineering problems. Hence, we employ a method of comparison, known as the relative CPU time, to assess the computational cost of the detailed mechanism and the REDIM method.

1.3 Outline

The thesis is organized as follows. Chapter 2 introduces fundamental theories used in combustion, which consists of basic flame types in section 2.1, governing equations in section 2.2 and numerical solution of conservation equations in section 2.3. Reaction mechanisms are discussed in chapter 3. Several reduction methods for chemical reactions are introduced: quasi-steady state assumptions (QSSA), partial-equilibrium assumptions (PEA), intrinsic low-dimensional manifolds (ILDM), flamelet generated manifolds (FGM) and reaction-diffusion manifolds (REDIM). The main focus of section 3.3 presents the mathematical background of the REDIM reduced chemistry, the implementation procedure of the REDIM method and an example of constructing REDIM table for a diffusion methane/air flame. In chapter 4, the implementation of detailed and reduced chemistry in OpenFOAM (EBIdnsFoam and REDIMFoam) is discussed. Their application on generic test cases is presented to validate the two solvers. The application of REDIM method to 2D counterflow flames is discussed in chapter 5. Steady and non-steady state results obtained by detailed and reduced mechanisms are compared. In chapter 6, the REDIM reduced chemistry is used to perform simulations for 2D jet diffusion flames in complex burner systems. The results of temperature, selected species, flame lifting, fuel leakage and soot precursor formation are discussed and compared in the physical space and state space. Finally, conclusion is given in chapter 7.

2 Fundamentals

The mathematization of physical phenomena is a characteristic of modern science, that is, scientists construct mathematical models to describe physical phenomena, and give quantitative predictions that can be used for experimental validations, which can be used by engineers and technicians. Combustion is an extremely complex process involving fluid flow (convection), molecular diffusion, chemical reactions, and radiation. There is one challenge for the combustion scientists to construct mathematical models that can describe all these observed physical phenomena of combustion, and allow prediction of events for which there are no measurements and experiments [7]. For the purpose of exposing the principle of the combustion processes with mathematical descriptions, this chapter will briefly discuss these fundamental concepts, definitions and conservation equations for reacting flows.

2.1 Basic flame types

In combustion, based on the state of mixedness of the reactants (fuel and oxidizer), flames are categorized as being either premixed flames or non-premixed (diffusion) flames. In premixed flames, the fuel and oxidizer are mixed before the occurrence of any chemical reactions and burned later. In non-premixed flames, fuel and oxidizer are initially separated, and chemical reactions occur only in the mixing zone between the fuel and oxidizer, where mixing and combustion take place simultaneously. Flames also can be subdivided into laminar or turbulent flames depending on whether the fluid flow is laminar or turbulent. This thesis primarily focuses on research related to laminar combustion, emphasizing the investigation of laminar combustion phenomena. As for turbulent combustion, one can refer to the relevant literature [4, 7, 11, 47].

2.1.1 Laminar premixed flames

One-dimensional (1D) laminar premixed flame is the basis to study complex combustion configurations, e.g. turbulent premixed flame can be viewed as a set of laminar premixed flames embedded in turbulent field (flamelet theory). Figure 2.1 displays the configuration of such 1D laminar premixed flame. In the figure, the fresh gas mixture consists of fuel and oxidizer. Once ignited and reacted, the mixture forms a flame front, characterized by its thickness referred to as the flame thickness. Eventually the reactants become products in the post-oxidation zone, such as CO_2 and H_2O. Figure 2.2 shows the typical profiles of a premixed CH_4-air flame (fresh gas mixture temperature: 300 K, stoichiometric) with GRI 3.0 mechanism [48] and assumption of unity Lewis number. There are many reliable programs to solve the 1D premixed flame, such as INSFLA [49], PREMIX [50], CHEMKIN [51], Cantera [52] and OpenFOAM [53], etc.

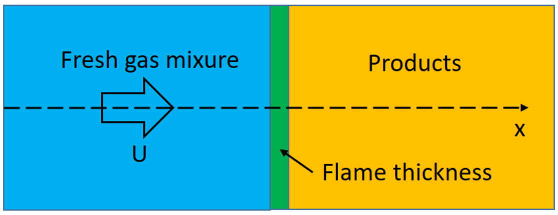

Figure 2.1: Configuration of 1D laminar premixed flame.

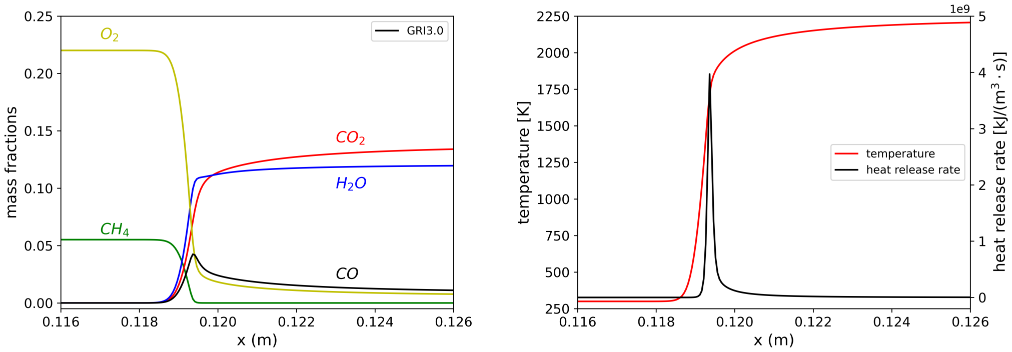

Figure 2.2: Computation of a stoichiometric CH_4-air premixed flame at 1 bar. Species profiles (left), temperature and heat release rate profiles (right).

2.1.2 Laminar diffusion flames

2.1.2.1 Laminar counterflow diffusion flames

Counterflow flames [54] are widely used to study combustion processes in experiments, e.g. flame structures, flammability of fuel, extinction characteristics, emission etc., as well as supply the experimental data to investigate the precision and accuracy of models in numerical combustion. A large number of literature (e.g. Refs. [55–57]) has been developed to study and analyze counterflow flames, and continues to expand rapidly.

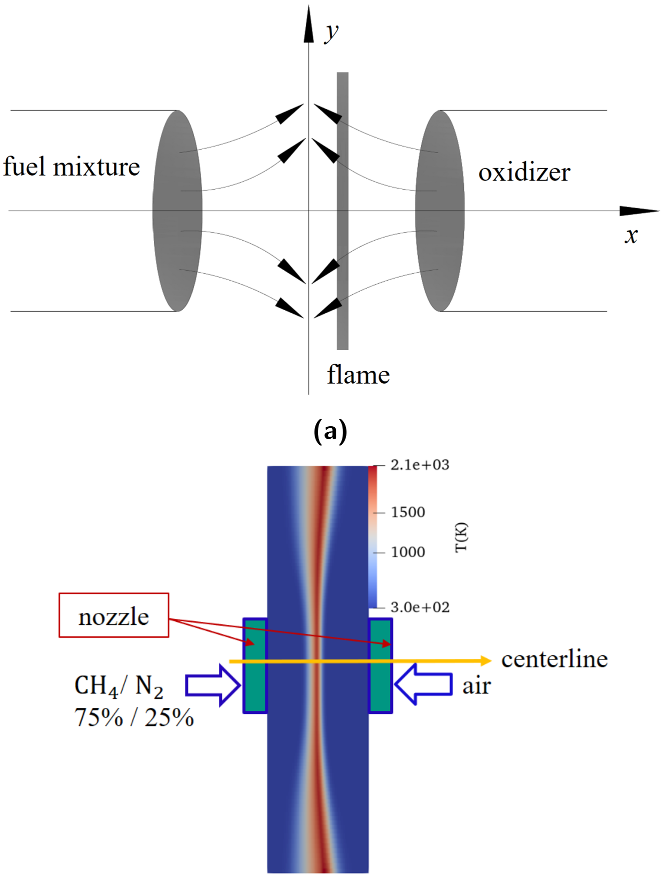

(a)

(b)

Figure 2.3: Schematic illustration of the counterflow flame configuration (a), one example of temperature (K) profile for the counterflow flame configuration (b).

A schematic view of the considered counterflow flame configuration is shown in Figure 2.3a. 2D axis-symmetric jets of fuel mixture and oxidizer impinge on each other from opposed nozzles. The stream of fuel mixture is injected through one pipe in the left boundary while the stream of air is injected from the right boundary, thus creating an axisymmetric flow field which can be described by the axial coordinate x and the radial coordinate y. Here the opposed jet flows of fuel and oxidizer, create a stagnation plane whose location depends on the relative magnitudes of the fuel mixture and oxidizer initial momentum fluxes [12]. The flame location is established between the two nozzles where the mixture fraction is nominally stoichiometric. For most hydrocarbon fuels burned in a counterflow flame configuration, the fuel mixture must diffuse across the stagnation plane to oxidizer, as shown in Figure 2.3a.

Figure 2.3b shows the result of temperature profile in which the fuel mixture side is methane mixed with nitrogen (75 % CH_4 + 25 % N_2 in volume percent) and the oxidizer side is air (21 % O_2 + 79 % N_2 in volume percent). The flame lies approximately at the midpoint where the stagnation plane closes to the stoichiometric plane, and the initial momentum fluxes are also approximately equal in this case.

2.1.2.2 Laminar jet diffusion flames

Examples of laminar jet flame occur frequently in actual combustion, such as candle flames, Bunsen burner, and oil lamps. In the jet flames, as the fuel mixture flows along the flame axis, it diffuses radially outward, while the oxidizer (e.g. air or pure oxygen) diffuses radially inward. The flame front is nominally defined to exist where the equivalence ratio of fuel or oxidizer is equal to 1, since the location is where the temperature is highest.

Figure 2.4a shows a typical configuration of the jet diffusion flame [58]. The homogeneous methane-N_2 mixture is injected into the surrounding atmosphere from a central pipe, and pure air flows from a surrounding concentric pipe. The mass fractions of CH_4 and N_2 are 0.6364 and 0.3636, respectively. For simplicity, we assume that the velocity profile is uniform at the tube exit, and the flow has reached a steady state. The GRI3.0 mechanism [48] and unity Levis number are implemented to calculate the case. The temperature profile of the jet diffusion flame, obtained by a numerical solution of the two-dimensional conservation equations in OpenFOAM, is shown in Figure 2.4b. The flame is axisymmetric, thus we here only calculate the half domain of the flame configuration to reduce the computational cost. The figure shows the flame being lifted off, the phenomenon explained in detail in chapter 6 through the concept of extinction. The extinction is observed near the nozzles due to the high strain rate in that area [7].

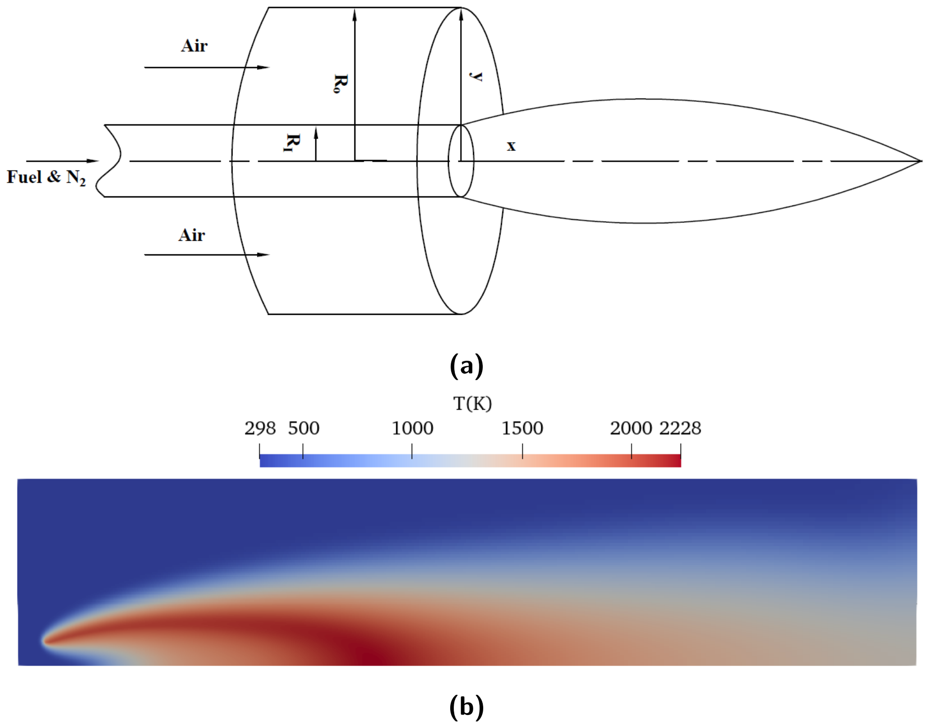

Figure 2.4: Schematic illustration of a jet flame configuration (a), Temperature (K) profile for the jet diffusion flame configuration (b).

2.2 Governing equations

A mathematical description of flame variation in time and space is the main research of numerical combustion. Some properties in combustion exhibit the characteristic of being conserved, such as mass, momentum, and energy. The summation of all processes altering these conserved properties gives rise to the conservation equations, which elucidate the change occurring within combustion. This section will briefly introduce these conservation equations used in reacting flows.

2.2.1 Continuity equation

This section describes the total mass conservation equation, which is also called the continuity equation. The total mass conservation, as the name implies, means that the mass flow entering or leaving the control volume (CV) through its surface per unit time remains the same. The rate of mass accumulation is considered in the following equation [59]:

$$\begin{bmatrix}\text{rate of mass}\\ \text{accumulation}\end{bmatrix} = \begin{bmatrix}\text{rate of mass flowing}\\ \text{in the volume}\end{bmatrix} - \begin{bmatrix}\text{rate of mass flowing}\\ \text{out the volume}\end{bmatrix}. \tag{2.1}$$

According to the above definition, the continuity equation can be derived and written in the form of Eqn. (2.2) [59]:

$$\frac{\partial \rho}{\partial t} + \nabla \cdot (\rho \boldsymbol{U}) = 0, \tag{2.2}$$

where ρ denotes the density, t is the time and $\boldsymbol{U}$ is the velocity vector.

2.2.2 Species mass fraction equation

As we can see, there is no source term in the total mass conservation equation (2.2), because chemical reactions do not generate mass, that is, the total mass is always conserved during the combustion process. To describe formation or consumption of species in chemical reactions, the species mass fraction equation with a source term is introduced, and the conservation equation for the mass fraction Y_k of species k is written as [11]:

$$\frac{\partial(\rho Y_k)}{\partial t} + \nabla \cdot (\rho Y_k (\boldsymbol{U} + \boldsymbol{U}_c)) + \nabla \cdot \boldsymbol{j}_k = \dot{\omega}_k, \tag{2.3}$$

where $\boldsymbol{U}_c$ represents the correction velocity, $\dot{\omega}_k$ is the reaction rate of species k (see section 3.1.3), and $\boldsymbol{j}_k$ denotes the diffusive mass flux density of species k. The correction velocity $\boldsymbol{U}_c$ is assessed to guarantee global mass conservation:

$$\boldsymbol{U}_c = -\frac{1}{\rho} \sum_{k=1}^{n_s} \boldsymbol{j}_k, \tag{2.4}$$

where n_s is the number of species. Further discussion on the diffusive mass flux density $\boldsymbol{j}_k$ can be found in section 4.1.2.

2.2.3 Momentum equation

The conserved momentum equation describes that the rate of momentum accumulation is caused by the rate of momentum entering or leaving the control volume and the sum of body and surface forces that act on the control volume [59]:

$$\begin{bmatrix}\text{rate of}\\ \text{momentum}\\ \text{accumulation}\end{bmatrix} = \begin{bmatrix}\text{rate of}\\ \text{momentum}\\ \text{entering the}\\ \text{volume}\end{bmatrix} - \begin{bmatrix}\text{rate of}\\ \text{momentum}\\ \text{leaving the}\\ \text{volume}\end{bmatrix} + \begin{bmatrix}\text{sum of}\\ \text{forces}\\ \text{acting}\\ \text{on the}\\ \text{volume}\end{bmatrix}. \tag{2.5}$$

According to the above consideration, the momentum equation can be derived and written in the form of Eqn. (2.6) [59]:

$$\frac{\partial(\rho\boldsymbol{U})}{\partial t} = -\nabla\cdot(\rho\boldsymbol{U}\otimes\boldsymbol{U}) - \nabla\cdot\boldsymbol{\tau} - \nabla p + \rho\mathbf{g}, \tag{2.6}$$

where the symbol $\boldsymbol{U}\otimes\boldsymbol{U}$ denotes the outer (dyadic) product of two velocity vectors, and $\boldsymbol{\tau}$ is the shear-rate tensor (viscous stress), ∇p the gradient of the pressure, $\mathbf{g}$ the gravitational acceleration vector. The shear-rate tensor $\boldsymbol{\tau}$ can be written in different formulae which depends on the properties of different liquids, e.g. Newtonian and Non-Newtonian fluids. The equation of the shear-rate tensor $\boldsymbol{\tau}$ can be derived by using the Stokes assumption for Newtonian fluid [60]:

$$\boldsymbol{\tau} = -\mu\left(\nabla\otimes\boldsymbol{U} + (\nabla\otimes\boldsymbol{U})^T - \frac{2}{3}(\nabla\cdot\boldsymbol{U})\boldsymbol{I}\right), \tag{2.7}$$

where μ is the dynamic viscosity and $\boldsymbol{I}$ denotes the identity matrix.

2.2.4 Energy equation

The energy conservation equation is derived from the first law of thermodynamics, which concerns the change in internal energies of two equilibrium states of one closed system due to the heat addition to the system and the work done on the system. In general, the law of conservation of energy can be describe as [60]:

$$\begin{aligned}&\begin{bmatrix}\text{rate of}\\ \text{kinetic and}\\ \text{internal energy}\\ \text{accumulation}\end{bmatrix} = \begin{bmatrix}\text{net rate of}\\ \text{kinetic and internal}\\ \text{energy addition}\\ \text{by convection}\end{bmatrix} + \begin{bmatrix}\text{net rate}\\ \text{of heat}\\ \text{addition by}\\ \text{conduction}\end{bmatrix} + \\ &\begin{bmatrix}\text{rate of work}\\ \text{done on system}\\ \text{by molecular}\\ \text{mechanisms}\end{bmatrix} + \begin{bmatrix}\text{rate of work}\\ \text{done on system}\\ \text{by external}\\ \text{forces}\end{bmatrix} + \begin{bmatrix}\text{net rate of}\\ \text{additional}\\ \text{heat sources}\end{bmatrix}.\end{aligned} \tag{2.8}$$

According to the above consideration, the energy equation can be derived and written in the form of Eqn. (2.9):

$$\begin{aligned}\frac{\partial(\frac{1}{2}\rho|\boldsymbol{U}|^2 + \rho e)}{\partial t} =& \underbrace{-\nabla\cdot\left(\frac{1}{2}\rho|\boldsymbol{U}|^2\boldsymbol{U} + \rho\boldsymbol{U}e\right)}_{\textit{convection}} \underbrace{-\nabla\cdot\boldsymbol{q}}_{\textit{conduction}} \underbrace{-\nabla\cdot(p\boldsymbol{U})}_{\textit{pressure}} \\ & \underbrace{-\nabla\cdot[\boldsymbol{\tau}\cdot\boldsymbol{U}]}_{\textit{viscous forces}} \underbrace{+\rho(\boldsymbol{U}\cdot\mathbf{g})}_{\textit{gravity}} + \underbrace{\nabla\cdot\boldsymbol{q}_{\text{rad}}}_{\textit{radiation}},\end{aligned} \tag{2.9}$$

where e denotes the internal energies, and $\boldsymbol{q}$ is the heat flux vector. The term in the left hand side of Eqn. (2.9) is the change of total energy by time for a finite volume element. And the first term in the right hand side (r.h.s) represents the rate of energy addition per unit volume by convection. The second term that changes the total energy is based on the heat conduction. The third, fourth and fifth terms of r.h.s in Eqn. (2.9) denote the work done by the fluid against its surroundings. The last term $\boldsymbol{q}_{\mathrm{rad}}$ is the radiative heat loss. The simulations conducted in this thesis utilize the energy equation expressed in terms of sensible enthalpy h_s, therefore the above equation can be rewritten as:

$$\begin{aligned}\frac{\partial(\rho h_s)}{\partial t} + \nabla \cdot (\rho \boldsymbol{U} h_s) = & -\frac{\partial(\rho K)}{\partial t} - \nabla \cdot (\rho \boldsymbol{U} K) - \nabla \cdot \boldsymbol{q} + \dot{\omega}_T \\ & - \nabla \cdot [\boldsymbol{\tau} \cdot \boldsymbol{U}] + \frac{\partial p}{\partial t} + \rho(\boldsymbol{U} \cdot \mathbf{g}) + \nabla \cdot \boldsymbol{q}_{\mathrm{rad}},\end{aligned} \tag{2.10}$$

where $K = \frac{|\boldsymbol{U}|^2}{2}$ denotes the specific kinetic energy and $\dot{\omega}_T$ is the heat release rate. The heat flux vector $\boldsymbol{q}$ is computed from:

$$\boldsymbol{q} = -\lambda \nabla T + \sum_{k=1}^{n_s} h_{sk} \hat{\boldsymbol{j}}_k, \tag{2.11}$$

in which includes a heat conduction term given by Fourier's law with the thermal conductivity λ and temperature T, which can be discretized implicitly. The sensible enthalpy h_{sk} of species k and the sensible enthalpy of the mixture h_s for ideal gases are calculated by:

$$h_{sk} = h_k - h^0_{f,k}, \quad h_s = \sum_{k=1}^{n_s} h_{sk} Y_k, \tag{2.12}$$

where $h^0_{f,k}$ is the enthalpy of formation of species k at standard reference state ($T_0 = 298.15$ K, $p = 1$ bar) and h_k is the enthalpy of species k. The corrected diffusive mass flux density $\hat{\boldsymbol{j}}_k$ is computed from:

$$\hat{\boldsymbol{j}}_k = \boldsymbol{j}_k - Y_k \sum_{k=1}^{n_s} \boldsymbol{j}_k. \tag{2.13}$$

The heat release rate $\dot{\omega}_T$ caused by combustion can be computed from:

$$\dot{\omega}_T = -\sum_{k=1}^{n_s} h^0_{f,k} \dot{\omega}_k. \tag{2.14}$$

2.2.5 Equation of state

The set of equations presented above does not include a method to calculate the density changes resulting from pressure and temperature variations in compressible reacting flow. Therefore, an additional equation is needed to describe the density variation. In most combustion systems, equation of state for ideal gases is valid, and even for high pressure combustion, it is a sufficiently accurate approximation as well. The equation of state for ideal gases is given by the following equation:

$$\rho = \frac{p\bar{M}}{RT}, \tag{2.15}$$

where R is the universal gas constant and is approximately equal to 8.314 $J/mol/K$, and $\bar{M}$ denotes the mean molecular mass.

2.3 Numerical solution of conservation equations

Computational fluid dynamics (CFD) is a subject that directly solves the basic governing equations by numerical methods and analyzes the laws of various flow phenomena. It integrates computational mathematics, computer science, fluid mechanics, scientific visualization and other disciplines. With the rapid development of computer technology, CFD is an increasingly important tool in many fields of scientific study and industries, including aerodynamics and aerospace analysis, weather forecast, industrial system design and analysis, fluid flows and heat transfer, engine and combustion analysis, etc. CFD and experimental methods to cooperate with each other speed up the scientific research and engineering design, as well as reducing computational cost.

As shown in section 2.2, the phenomena of fluid flow and combustion are described by a series of partial differential equations (PDE), such as mass, momentum and energy conservation equations, which are nonlinear and difficult to obtain analytical solutions. In order to get the numerical solution of the equation system, there are several numerical methods used in CFD. The main difference between these methods is the discretization of the governing equations. The discretization methods can be roughly divided into three branches according to the discrete principles:

- Finite Difference Method (FDM)
- Finite Element Method (FEM)
- Finite Volume Method (FVM)

Amongst the above numerical methods used in CFD, the finite volume method plays an increasingly important role [61].

2.3.1 Finite volume method

The FVM is a numerical method to solve PDE, and this method is used in many computational fluid dynamics software (e.g. OpenFOAM) [62]. The FVM is based on integral conservation equations rather than differential equations. The basic idea of FVM is to divide the computational domain into a series of grids, and make each grid surrounded by a non-repeating control volume; then integrate the governing equations over each control volume, and yield a set of discrete equations.

The general conservation equation of a scalar variable ϕ can be written as [61]:

$$\frac{\partial(\rho\phi)}{\partial t} + \nabla \cdot (\rho \boldsymbol{U} \phi) = \nabla \cdot (\Gamma_\phi \nabla \phi) + S_\phi, \tag{2.16}$$

where ϕ represents any conserved quantity. Γ_ϕ and S_ϕ denote the diffusion coefficient and source term of ϕ. By applying the integral form of the above governing equation over each CV, Eqn. (2.16) is transformed to:

$$\int_V \frac{\partial(\rho\phi)}{\partial t} dV + \int_V \nabla \cdot (\rho \boldsymbol{U} \phi) dV = \int_V \nabla \cdot (\Gamma_\phi \nabla \phi) dV + \int_V S_\phi dV, \tag{2.17}$$

where dV is the integration with respect to the volume. Replacing the volume integral by surface integral through the use of Gauss' divergence theorem, and assuming that all the control volumes are not deforming, the above equation becomes:

$$\frac{\partial}{\partial t} \int_V \rho\phi dV + \oint_S \nabla \cdot (\rho \boldsymbol{U} \phi) \boldsymbol{n} dS = \oint_S \nabla \cdot (\Gamma_\phi \nabla \phi) \boldsymbol{n} dS + \int_V S_\phi dV, \tag{2.18}$$

where $\boldsymbol{n}$ is the outward-pointing surface normal vector and dS is the infinitesimal surface element with associated the normal $\boldsymbol{n}$.

The FVM solves the integral formulation of conservation equation, which gives an advantage of being conservative without special cares. Another advantage of the FVM is that it can be widely used on structured and unstructured meshes, therefore the method is suitable for complex geometries in engineering problems. Moreover, in fluid-solid interaction analysis, it can be perfectly integrated with finite element method. However, the disadvantage of FVM is that it is difficult to approximate the solution of the governing equations with higher order.

2.3.2 Numerical techniques for solving Navier-Stokes equation

The previous section 2.2 introduces the Navier-Stokes equation which couples the pressure and momentum quantities, but how to solve this equation is an important issue of CFD. In this section, some of the most common techniques used to solve the equation will be discussed briefly. Further description about the numerical methods to solve the Navier-Stokes equation can be found in the corresponding literature [61, 63].

Firstly, we consider the momentum equation (2.6):

$$\frac{\partial(\rho \boldsymbol{U})}{\partial t} = -\nabla \cdot (\rho \boldsymbol{U} \otimes \boldsymbol{U}) - \nabla \cdot \boldsymbol{\tau} - \nabla p + \rho \mathbf{g}.$$

There are 4 unknown variables in the equation, pressure p and three components of velocity $\boldsymbol{U}$ (U_x, U_y and U_z in Cartesian coordinate system). As we can see, the pressure and velocity are coupled together, and there is no independent pressure equation to compute the pressure. Therefore we need some numerical techniques for solving the pressure-velocity coupling equation.

A strategy now is to construct the Poisson equation based on the continuity equation, and solve the solution of Poisson equation by some algorithms that fulfil the mass conservation and convergence conditions (details see Refs. [59, 63]). The popular approaches for dealing with the pressure-velocity coupling problem, that is, Poisson equation, are SIMPLE [64], PISO [65], and PIMPLE [59] algorithms:

- SIMPLE: Semi-Implicit Method for Pressure-Linked Equations.
  The SIMPLE algorithm is a pressure-based segregated method for computing steady-state flows.

- PISO: Pressure-Implicit with Splitting of Operators.
  The PISO algorithm is designed for transient flows. The computation is limited in the time step based on the Courant number [66].

- PIMPLE: Merged PISO-SIMPLE.
  The PIMPLE algorithm merges the PISO and the SIMPLE algorithm, which can be used for transient flows.

The simulations carried out in the work exclusively focus on laminar flows with a very low Reynolds number. Consequently, the selected PIMPLE algorithm is able to provide accurate results in the thesis.

For numerical stability, the Courant number is used in simulations to evaluate the time step, which is set to between 0.1 and 0.2 in all calculations presented in this thesis. And the Courant number is defined as:

$$Co = \frac{1}{2}\Delta t \frac{\sum_f |\boldsymbol{U}_f \cdot \boldsymbol{n}_f| A_f}{V_c} \leq 0.2, \tag{2.19}$$

where f represents the index of the cell faces, $\boldsymbol{U}_f$ is the velocity in the middle of the face f, A_f the surface area of face f, $\boldsymbol{n}_f$ its surface unit normal vector, and V_c is the volume of the cell.

2.3.3 OpenFOAM

Open field operation and manipulation (OpenFOAM) is a free C++ toolbox designed to solve problems of continuum mechanics, most prominently applying to CFD [53]. OpenFOAM can solve a wide range of problems, including complex flows with chemical reactions, turbulence, and heat transfer, as well as solid dynamics and electromagnetism, etc.

OpenFOAM is C++ class libraries (approximately 100) used to create executable files such as *application*. There are approximately 250 pre-built applications in OpenFOAM that fall into two categories: *solver* and *utilities* [53]. Solver is specifically designed to address problems in continuum mechanics, while utilities are tailored for tasks such as data manipulation. The largest advantage is that users can define their own solvers for certain applications based on OpenFOAM's basic class library to meet calculation requirements.

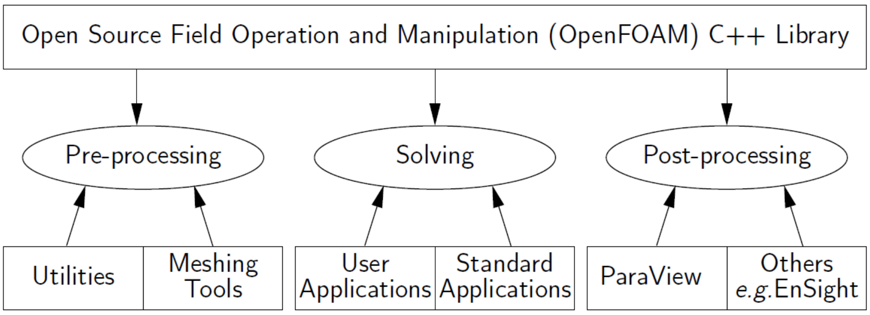

Figure 2.5: Overview of OpenFOAM structure [53].

There are three steps to perform one certain computational task by using OpenFOAM: pre-processing step, solving step and post-processing step. The overall structure of OpenFOAM is shown in Figure 2.5. The pre-processing step consists of definition of geometry for a given task, mesh generation, selection of fluid properties, specification of physical boundary conditions, domain decomposition if needed, etc. The solving step contains selection of appropriate solver or self-defined solver to solve the studied work. The solvers include the calculation process for solving corresponding mass, energy and momentum conservation equations. The post-processing step is that you can take a look at the results computed by the solver and visualize data by suitable cutting planes, contour plots of variables and line plots.

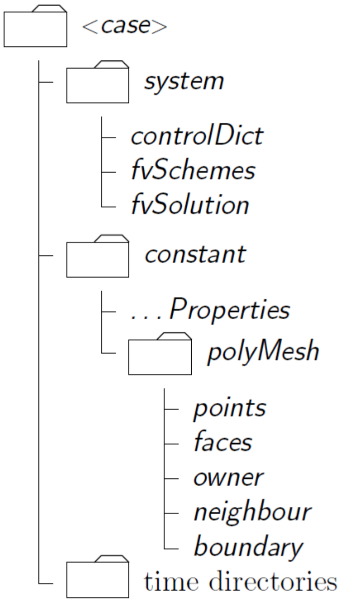

Figure 2.6: Case directory structure of OpenFOAM [53].

An OpenFOAM case contains mesh description of geometry, boundary conditions of physical properties, solver settings and temporal and spacial discretization schemes, etc. Figure 2.6 shows one sample of the basic case directory structure used in OpenFOAM. The detailed description of these directories is as follows:

A *constant* directory that consists of all the mesh information in a subdirectory *polyMesh* and files specifying physical and chemical properties used in the solver concerned in simulations:

- transportProperties: specify the fluid properties, e.g. viscosity.
- turbulenceProperties: specify the turbulent modelling used in solvers, e.g. *laminar* for laminar flow models; *RAS* for Reynolds-averaged simulation modelling; *LES* for large-eddy simulation modelling.

- g: includes the gravity acceleration.
- chemisrtyProperties: obtain reaction rate from kinetic data, and the numerical method of the solver to calculate the reaction rate is selected in the dictionary.
- reaction: supplies reaction mechanism for reacting flows, e.g. GRI3.0, C1-C3 hydrocarbons.
- combustionProperties: list interactions between the reactions and the fluid flow in combustion.
- thermophysicalProperties: are concerned with energy, heat and physical properties, e.g. selection of thermo-physical and mixture models, transport models, thermodynamic models and energy equation, equation of state, etc.
- thermo.compressibleGas: specify the constants for each species as input data to calculate the viscosity, specific heat capacity and density.

A *system* directory is mainly used to set the parameters of the solution procedure. It contains at least the 3 files: *controlDict*, *fvSchemes* and *fvSolution*.

- controlDict: specify simulation parameters consisting of start/end time, time step, Courant number and parameters for post-processing.
- fvSchemes: contain the selection of temporal and spacial discretization schemes for each term of the equations at run-time.
- fvSolution: specify the parameters and solver choice like the equation solvers, pre-conditioners, tolerances and the coupling method of pressure and velocity.

The *time* directories contain variables dictionary files of data (e.g. velocity, pressure, temperature, species, etc.) written by OpenFOAM for each time. The initial values and boundary conditions must be defined in 0 time directory before simulation.

3 Reaction mechanisms

A reaction mechanism consists of a series of elementary reactions, offering a detailed, step-by-step description of how initial reactants transform into final products through chemical processes. In most cases, the detailed steps of the reaction are not observed. Typically, a reaction mechanism is a theoretical hypothesis that attempts to provide a detailed description of each stage within a global chemical reaction. A reaction mechanism has the capacity to elucidate each reaction intermediate, active complex, and transition state, as well as the sequence in which bonds are broken or formed. Moreover, a comprehensive reaction mechanism should offer the reason for selecting reactants and catalysts while also explain all generated products and their respective quantities.

Over the past few decades, significant advancements in combustion research have been achieved as chemists elucidated chemical pathways from reactants to products, determined corresponding reaction rates through measurements or calculations, and developed comprehensive reaction mechanisms. This knowledge has paved the way for substantial progress in the field. With a deep understanding of combustion chemistry and development of computer science, scientists and engineers specializing in combustion can construct numerical models to simulate reaction systems, thereby enhancing analysis and prediction capabilities. In this chapter, we will briefly introduce the basic kinetics concepts, definitions and methods used in the reaction mechanism.

3.1 Global and elementary reactions and reaction ates

3.1.1 Global reaction

In combustion reactions one or several global reactions are typically used to describe the fuel combustion process, e.g. $2H_2 + O_2 \rightarrow 2H_2O$. The generalized form for global reaction of 1 mole of fuel (F) reacting with a moles of oxidizer (O_x) to form b moles of products (P_r) can be written as [12]:

$$\mathrm{F} + a\mathrm{O}_x \rightarrow b\mathrm{P}_r. \tag{3.1}$$

The consumed rate of fuel in the global reaction is computed by:

$$\frac{d[X_F]}{dt} = -k_G(T)[X_F]^n[X_{O_x}]^m, \tag{3.2}$$

where $[X_i]$ denotes the molar concentration of the i-th species in the mixture, and k_G is the global rate coefficient of the reaction, which is a function closely related to temperature. Here the exponents n and m represent reaction order, and the sum of all exponents ($n + m$) is the global reaction order.

The global reaction can be established by formulating a mathematical model of the reactants and products or by fitting the material coefficients with experimental data. It can also be built on the basis of the detailed reaction mechanism, using simplified methods such as quasi-steady state assumptions, partial-equilibrium assumptions and singular perturbation method. The global reaction is widely used in numerical calculation combined with CFD, which can greatly reduce the computational effort [67]. However,the use of global reactions to describe the chemical reactions occurring in combustion is usually a “black box” method [12]. This method may be useful for solving some particular problems, but it neglects the complex kinetics and intricate interactions between different species, which are critical for understanding combustion characteristics and pollutant formation. Therefore, introducing elementary reaction and reaction mechanism constructing from the elementary reaction become essential in order to address the deficiencies of the global reaction.

3.1.2 Elementary reaction

An elementary reaction refers to a reaction in which one or more species directly interact in a single reaction step to yield products, commonly known as a simple reaction [7]. Reaction mechanism usually consists of many elementary reactions and many species, for example, the reaction mechanism GRI3.0, widely used in calculations of methane combustion, involves 53 species and 325 elementary reactions [48]. Therefore, it is necessary to develop one compact notation method which can denote both mechanism and individual species formation rates.

3.1.3 Net production rate

The general form of a chemical reaction in one reaction mechanism can be described as:

$$a\mathrm{A} + b\mathrm{B} + c\mathrm{C} + \cdots \underset{k_r}{\overset{k_f}{\Longleftrightarrow}} d\mathrm{D} + e\mathrm{E} + f\mathrm{F} + \cdots , \tag{3.3}$$

where $\mathrm{A}, \mathrm{B}, \mathrm{C}, \cdots$ denote the reactants in the left side of the reaction, $\mathrm{D}, \mathrm{E}, \mathrm{F}, \cdots$ represent the products in the right side of the formula and k_f and k_r are the forward and reverse rate coefficients for the elementary reaction, respectively. The reaction rate of species A can be expressed as:

$$\frac{d[A]}{dt} = k_r \cdot [\mathrm{D}]^d[\mathrm{E}]^e[\mathrm{F}]^f \cdots - k_f \cdot [\mathrm{A}]^a[\mathrm{B}]^b[\mathrm{C}]^c \cdots , \tag{3.4}$$

where these lowercase $a, b, c, d, e, f, \ldots$ denote reactions orders with respect to the species $\mathrm{A}, \mathrm{B}, \mathrm{C}, \mathrm{D}, \mathrm{E}, \mathrm{F}, \ldots$, and the rate coefficient k in Eqn. (3.4) can be expressed by the empirical Arrhenius form [12, 68]:

$$k = AT^{\beta}\exp(-\frac{E_a}{RT}), \tag{3.5}$$

where A denotes the pre-exponential factor, β the temperature exponent, R the universal gas constant and E_a the activation energy. For a reaction mechanism with n_s species and n_r reactions, the formula to describe the mechanism can be written as:

$$\sum_{k=1}^{n_s} \nu_{ik}^{'} X_k \underset{k_{ri}}{\overset{k_{fi}}{\Longleftrightarrow}} \sum_{k=1}^{n_s} \nu_{ik}^{''} X_k, \quad i = 1, 2, \cdots, n_r \tag{3.6}$$

here $\nu_{ik}^{'}$ and $\nu_{ik}^{''}$ denote the stoichiometric coefficients of reactants and products, respectively, and k_{fi} and k_{ri} are the forward (f) and reverse (r) rate coefficients for the i-th elementary reaction, respectively. The net production rate of the k-th species $\dot{\omega}_k$ (used in Eqn. (2.3)) in all elementary reactions is given by:

$$\dot{\omega}_k = \frac{\partial[X_k]}{\partial t} = \sum_{i=1}^{n_r}\left[(\nu_{ik}^{''} - \nu_{ik}^{'})(k_{fi}\prod_{k}^{n_s}[X_k]^{\nu_{ik}^{'}} - k_{ri}\prod_{k}^{n_s}[X_k]^{\nu_{ik}^{''}})\right]. \tag{3.7}$$

3.2 Reduced reaction mechanisms

In combustion processes, the reaction mechanisms can be extremely complex and involve a large number of elementary reactions. For example, the calculation of methane combustion with GRI3.0, as presented in the previous section, considers 325 elementary reactions. In much more complex systems, such as engine ignition, detailed reaction mechanisms can involve hundreds of species and thousands of elementary reactions [18]. The complexity of the chemical mechanism not only results in an unbearable computational cost, but also has severe consequences for numerical simulations due to the wide variation in characteristic time scales. This leads to extreme stiffness in the partial equations system, which poses significant challenges for numerical calculations [7]. In order to solve these issues, researchers and scientists often use reduced mechanisms in the relevant combustion calculation.

To simplify the reaction mechanism, conventional methods such as sensitivity analysis [20], Jacobian analysis [21], and principal component analysis [22] are often used to eliminate unimportant species and elementary reactions and obtain a skeletal mechanism. The skeletal mechanism can be further simplified by making the quasi-steady state assumption for specific species and assuming partial equilibrium for a number of elementary reactions [12]. We will provide a brief overview of these reduced methods in the following sections. For a more detailed discussion of reduced mechanisms, one can refer to original papers, reviews, and textbooks that focus on the dynamics of chemical reactions.

3.2.1 Traditional simplification methods

In most reaction mechanisms involved in the combustion process, many reactive intermediates, namely, radicals, are generated. Normally, following a rapid change in the concentration of these radicals, at some stage of the reaction (called quasi-steady state), the consumption rate of the radicals is approximately equal to the formation rate of the radicals [69]. The quasi-steady state approximation (QSSA) is based on the intermediates in quasi-steady state to simplify the detailed reaction mechanism.

The partial-equilibrium approximation (PEA) provides another approach to simplify the reaction mechanism by eliminating fast variables [70]. Specifically, if a particular reaction is significantly faster than the others, the extent of that reaction can be assumed to reach a state of equilibrium much faster. As a result, the fast reaction can be eliminated from the overall reaction mechanism [71].

3.2.2 Intrinsic low-dimensional manifolds (ILDM)

Traditional simplification methods, such as QSSA and PEA discussed above, have some drawbacks. Researchers who use these approaches must have much experience in the simplification of reaction mechanisms, and considerable time and labour are required by these methods. Moreover, the traditionally simplified mechanism can only be applied to a particular combustion scenario. For example, one reduced mechanism can be used to predict accurately ignition times, however accurate prediction of the propagation velocity of premixed flames for same mixture of fuel and oxidizer needs another reduced mechanism. Intrinsic low-dimensional manifolds (ILDM) [23] is a general procedure for simplifying reaction mechanisms which can overcome these drawbacks. The ILDM does not need to know which reactions are in partial equilibrium, nor which species are in steady state. The procedure only needs the detailed mechanism and the number of degrees of freedom required in the reduced mechanism as inputting information.

Typically, the time scales of chemical and physical processes usually span several orders of magnitude (see Figure 3.1). Chemical reactions in combustion processes usually cover a range from 10^{-10} s to 10^{0} s. The time scales of physical processes (e.g. flow, transport, turbulence) usually cover the range from 10^{-5} s to 10^{-2} s [7]. The fast time scales of chemical reactions are typically responsible for the equilibration processes, e.g. species in quasi-steady state and reactions in partial equilibrium [23]. Therefore, it is possible to decouple the chemical time scales by removing the fastest time scales, which are assumed to be in local equilibrium.

In order to decouple all time scales of chemical reactions and minimize the computational effort, several methods, for instance, intrinsic low-dimensional manifolds (ILDM) [23], flame prolongation of ILDM (FPI) [26], method of invariant manifold (MIM) [25] and reaction-diffusion manifolds (REDIM) [27] are used to simplify the chemical kinetics. These methods can decrease both computational cost and the stiffness of partial differential equations, which can significantly increase the performance of numerical calculations.

The mathematical model based on ILDM (details see Ref. [72]) can be described by the detailed evolution equation of a typical reacting flows with the ($n = n_s$+2)-dimensional state vector $\boldsymbol{\Psi} = (h, p, \phi_1, \cdots, \phi_{n_s})^T$, which is written as:

$$\frac{\partial \boldsymbol{\Psi}}{\partial t} = \boldsymbol{F}(\boldsymbol{\Psi}) - \boldsymbol{U} \cdot \nabla \boldsymbol{\Psi} - \frac{1}{\rho} \nabla \cdot (\boldsymbol{D} \cdot \nabla \boldsymbol{\Psi}), \tag{3.8}$$

here h is the specific enthalpy, p is the pressure, the ratio $\phi_k = \frac{Y_k}{M_k}$ denotes the specific mole number consisting of mass fraction Y_k and corresponding species molar mass M_k, $\boldsymbol{D}$ represents the $(n \times n)$-dimensional diffusion matrix given via [7, 72], and $\boldsymbol{F}(\boldsymbol{\Psi})$ is the n-dimensional vector $(0, 0, \dot{r}_1, \cdots, \dot{r}_{n_s})$ that accounts for the chemical source terms, $\dot{r}_{n_k} = \frac{\dot{\omega}_k}{M_k}$ and t denotes the time.

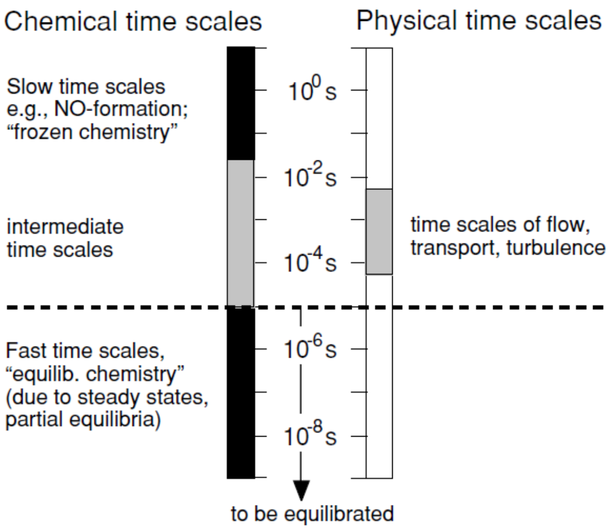

Figure 3.1: Time scales of chemical and physical processes in combustion [7].

Initially, the ILDM method is introduced through a limiting example, namely, a homogeneous reaction system. Thus, the convective and diffusive terms in Eqn. (3.8) vanish, then the equation can be simplified to:

$$\frac{\partial \boldsymbol{\Psi}}{\partial t} = \boldsymbol{F}(\boldsymbol{\Psi}). \tag{3.9}$$

The $(n \times n)$-dimensional Jacobi matrix $\boldsymbol{F}_{\boldsymbol{\Psi}}$ $((F_\Psi)_{ij} = \frac{\partial F_i}{\partial \Psi_j})$ of the chemical source terms can be decomposed into the invariant subspaces to identify fast or slow reactions in chemical processes

$$\boldsymbol{F}_{\boldsymbol{\Psi}} = (\boldsymbol{Z}_s \boldsymbol{Z}_f) \cdot \begin{pmatrix} \boldsymbol{N}_s & 0 \\ 0 & \boldsymbol{N}_f \end{pmatrix} \cdot \begin{pmatrix} \tilde{\boldsymbol{Z}}_s \\ \tilde{\boldsymbol{Z}}_f \end{pmatrix}, \tag{3.10}$$

here $\boldsymbol{Z}_s$ is the $(n \times m_s)$-dimensional matrix which forms an invariant subspace associated with the m_s eigenvalues having the smallest real parts $(\boldsymbol{N}_s)$, and $\boldsymbol{Z}_f$ denotes the $(n \times m_f)$-dimensional invariant subspace belonging to the m_f eigenvalues having the largest real parts $(\boldsymbol{N}_f)$, where m_s and m_f are the number of eigenvalues according to slow and fast processes [73, 74]. $\boldsymbol{N}_s$ is an $(m_s \times m_s)$-dimensional matrix and $\boldsymbol{N}_f$ is an $(m_f \times m_f)$-dimensional matrix and

$$(\boldsymbol{Z}_s \boldsymbol{Z}_f)^{-1} = \begin{pmatrix} \tilde{\boldsymbol{Z}}_s \\ \tilde{\boldsymbol{Z}}_f \end{pmatrix}. \tag{3.11}$$

$\tilde{\boldsymbol{Z}}_s$ is the $(m_s \times n)$-dimensional matrix and $\tilde{\boldsymbol{Z}}_f$ is the $(m_f \times n)$-dimensional matrix of invariant subspaces corresponding to the slow and fast processes respectively. The general assumption that the fast processes have already relaxed defines an m_s-dimensional manifold in the state space via:

$$\tilde{\boldsymbol{Z}}_f(\boldsymbol{\Psi}) \cdot \boldsymbol{F}(\boldsymbol{\Psi}) = 0. \tag{3.12}$$

The manifold is formed with points where the reaction rates in the direction of the fast processes vanish. In this way the ILDM in the state space is defined and computed numerically [27, 75, 76]. Eggles *et al.* conducted an in-depth comparative study between the ILDM method and the traditional simplification methods based on the QSSA, and found that the performance of the two methods was very close [77]. However the ILDM method shows much better performance in comparison with the QSSA in other standard problems, e.g. Davis-Skodje model [78, 79].

The ILDM method assumes that chemistry is much faster than convective and diffusive processes. However, the assumptions give poor approximations in the low-temperature domain of a flame, where chemistry and transport time scales have the same order. The problem can be partly overcome by addition of extra dimensions to the ILDM in order to meet the requirement of accuracy [80]. However, this may result in a higher dimensional look-up table in the application of the ILDM method, which can increase the computational efforts as well. To improve the performance of ILDM in the low-temperature domain, several different methods are proposed, e.g. FPI [26] and extended ILDM [81]. The calculation results with these methods demonstrate a significant improvement in the performance of ILDM in the low-temperature region, with a notable reduction in computational cost.

3.2.3 Flamelet generated manifolds (FGM)

In order to solve the the problem of poor approximations of the ILDM method in the colder part of the reaction zone, Oijen *et al.* proposed another approach, named flamelet generated manifolds (FGM) technique [24]. This method shares the idea with so-called flamelet concept, that is, a three-dimensional flame can be viewed as an ensemble of many one-dimensional (1D) premixed flames [47]. Therefore, a FGM is constructed by using a set of 1D laminar flamelets, while the application of the generated manifold is similar as in the case of the ILDM method [82].

The main evolution process of all species are assumed to take place in the s-direction, where the coordinate is locally perpendicular to the isosurfaces of a certain species mass fraction Y_k in terms of the FGM method. The set of flamelet equations used to generate a manifold is written as [24, 82]:

$$\frac{\partial(\dot{m}Y_k)}{\partial s}+\frac{\partial}{\partial s}\left(\frac{1}{Le_k}\frac{\lambda}{C_p}\frac{\partial Y_k}{\partial s}\right)=\dot{\omega}_k+P_k, \quad k\in[1,n_s], \tag{3.13}$$

$$\frac{\partial(\dot{m}h)}{\partial s}-\frac{\partial}{\partial s}\left(\frac{\lambda}{C_p}\frac{\partial h}{\partial s}\right)=\frac{\partial}{\partial s}\sum_{k=1}^{n_s}h_k\frac{\lambda}{C_p}\left(\frac{1}{Le_k}-1\right)\frac{\partial Y_k}{\partial s}+Q_h, \tag{3.14}$$

with the constant mass-flow rate $\dot{m}$, the thermal conductivity λ, the Lewis number Le_k, the heat capacity at constant pressure C_p, the chemical source term $\dot{\omega}_k$, and the enthalpy h , and the specific enthalpy of species k h_k. The number of species is represented by n_s. Furthermore, the perturbation terms P_k and Q_h describe non-stationary state within the moving flame and transport term along the isosurfaces.

A solution of the set of flamelet equations, including the results of $Y_k(s)$ and $h(s)$, is called a flamelet and constitutes a curved line in composition space which can be viewed as a one-dimensional manifold parametrized by s. In order to use the manifold in further application, controlling variable (or progress variable) Y_{CV} must be selected. The choice of controlling variable should guarantee a unique mapping $Y_k(Y_{\mathrm{CV}})$ for all species i. This means that $Y_{\mathrm{CV}}(s)$ should be a monotonic function of s.

There is no flamelet data in the colder part of the reaction zone, when the enthalpy of mixture drops below the “coldest” flamelet, which is shown in Figure 3.2. The FGM method uses a special regime to prolongate the low-enthalpy region [24]. The region is firstly mapped onto the unit square (η,ζ) defined by:

$$\eta=\frac{Y_{\mathrm{CV}}-Y_{\mathrm{CV},b}}{Y_{\mathrm{CV},u}-Y_{\mathrm{CV},b}} \quad \text{and} \quad \zeta=\frac{h-h_{min}}{h^L-Y_{min}}, \tag{3.15}$$

where the subscripts b and u represent the values of controlling variables at unburnt and burned conditions, h^L is the enthalpy at the coldest flamelet and h_{min} denotes the enthalpy of the chemical equilibrium at $T=T_{min}$ (point A in Figure 3.2). The dependent variables φ is the function of (Y_{CV},h), which can be denoted by $\varphi(Y_{\mathrm{CV}},h)=f(\eta,\zeta)$. The profiles of dependent variables along the coldest flamelet and the chemical equilibria can be given by $f(\eta,1)$ and $f(1,\zeta)$. The values in the so called low-enthalpy zone are evaluated by linear interpolation using the equation

$$f(\eta,\zeta)=\frac{f(0,\zeta)-f(0,0)}{f(0,1)-f(0,0)}[f(\eta,1)-f(0,0)]+f(0,0). \tag{3.16}$$

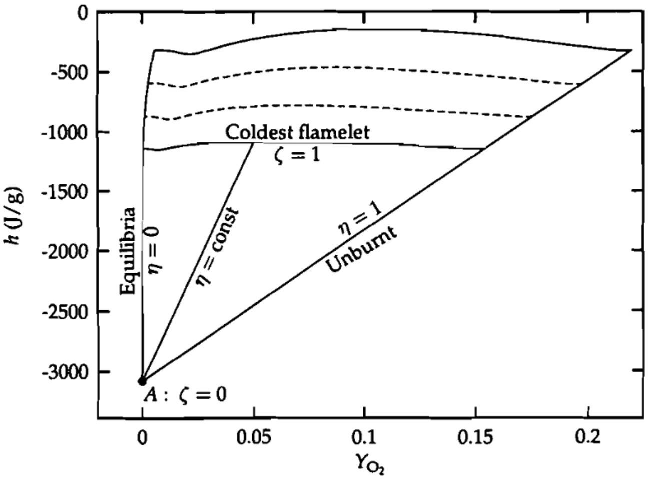

Figure 3.2: Interpolation in low enthalpy region [24].

The FGM method's limitation lies in its assumption that combustion occurs either in a completely premixed or completely non-premixed mode. As a result, using premixed flamelets to estimate diffusion combustion or diffusion flamelets to estimate premixed combustion leads to significant differences in the results. To solve this limitation and improve the performance of FGM, multi-dimensional flamelet model is proposed [83–85]. The multi-regime approach describes the flame structure more comprehensively compared to classical method based on a single flame regime [86]. However, this method significantly amplifies the number of flamelets, sometimes exceeding 3000, consequently leading to a large increase in computational effort of generating FGM [85].

3.3 Reaction-diffusion manifolds (REDIM)

As discussed in the above ILDM section, the reduction method ILDM does not work well in the whole state space. The simulation accuracy of this method is higher in the high-temperature combustion region; however, in the low-temperature combustion region, due to the slow chemical reaction, the combustion process is more affected by convection and diffusion, leading to a reduction in accuracy. To overcome the limitations of the ILDM method, a general approach called reaction-diffusion manifold (REDIM) has been developed, which builds upon the extended ILDM method and the invariant manifold concept [27]. The REDIM method considers not only the effect of the reaction system but also the coupling of molecular transport with thermochemical processes in the generating process of automatically simplified chemistry [87]. This approach offers a solution to the challenges faced by the ILDM method.

As with the formulation of the typical system of partial differential equations introduced in the ILDM method to describe reacting systems, we also can begin with considering Eqn. (3.8):

$$\frac{\partial \boldsymbol{\Psi}}{\partial t} = \boldsymbol{F}(\boldsymbol{\Psi}) - \boldsymbol{U} \cdot \nabla \boldsymbol{\Psi} - \frac{1}{\rho} \nabla \cdot (\boldsymbol{D} \cdot \nabla \boldsymbol{\Psi}) \equiv \boldsymbol{\Phi}(\boldsymbol{\Psi}), \tag{3.17}$$

where $\boldsymbol{\Phi}(\boldsymbol{\Psi})$ is the vector field, that automatically belongs to the tangent space if and only if the manifold is an invariant manifold. We suppose that the solution of Eqn. (3.17) belongs to an m_s-dimensional slow manifold and the low-dimensional invariant manifold can be defined as:

$$M = \{\boldsymbol{\Psi} : \boldsymbol{\Psi} = \boldsymbol{\Psi}(\boldsymbol{\theta}), \boldsymbol{\Psi} : R^{m_s} \to R^n\}, \tag{3.18}$$

where $\boldsymbol{\Psi}(\boldsymbol{\theta})$ is an explicit function parameterized by the variable $\boldsymbol{\theta}$ (an m_s-dimensional vector of local coordinates) and M is the invariant m_s-dimensional system manifold, which can be used to describe the system solution of state space by m_s parameters instead of using n parameters ($m_s \ll n$).

3.3.1 REDIM evolution equation

According to the core concept of manifold dimension reduction, the problem of model reduction is transformed into identifying and describing manifolds with particular conditions [29]. For the PDE formed by Eqn. (3.17), its invariant manifold must satisfy a condition, that is, any state point $\boldsymbol{\Psi}$ belongs to tangent space $T_\Psi M$ of the low-dimensional manifold M. This means that the right vector field in Eqn. (3.17) follows the condition [27]:

$$\left(\boldsymbol{\Psi}_{\boldsymbol{\theta}}^{\perp}(\boldsymbol{\theta})\right)^T \cdot \boldsymbol{\Phi}(\boldsymbol{\Psi}) \equiv 0, \tag{3.19}$$

where $\boldsymbol{\Psi}_{\boldsymbol{\theta}}^{\perp}$ defines the normal space to the invariant manifold as $(\boldsymbol{\Psi}_{\boldsymbol{\theta}}^{\perp})^T \cdot \boldsymbol{\Psi}_{\boldsymbol{\theta}} \equiv 0$ and $\boldsymbol{\Psi}_{\boldsymbol{\theta}}$ denotes the tangent space to the manifold, which is the $(n \times m_s)$-dimensional matrix of partial derivatives of $\boldsymbol{\Psi}$ with respect to $\boldsymbol{\theta}$ ($\{\Psi_\theta\}_{ij} = \frac{\partial \Psi_i}{\partial \theta_j}$). By using a projection operator to project the vector field $\boldsymbol{\Phi}(\boldsymbol{\Psi})$ onto its normal space, this condition can be expressed as follows:

$$(\boldsymbol{I} - \boldsymbol{\Psi}_{\boldsymbol{\theta}} \boldsymbol{\Psi}_{\boldsymbol{\theta}}^{+}) \cdot \boldsymbol{\Phi}(\boldsymbol{\Psi}) = 0, \tag{3.20}$$

where $\boldsymbol{I}$ is the $(n \times n)$-dimensional identity matrix and $\boldsymbol{\Psi}_{\boldsymbol{\theta}}^{+}$ is an $(m_s \times n)$-dimensional pseudo-inverse matrix of $\boldsymbol{\Psi}_{\boldsymbol{\theta}}$ (see [73]), which fulfils the condition:

$$\boldsymbol{\Psi}_{\boldsymbol{\theta}}^{+}\boldsymbol{\Psi}_{\boldsymbol{\theta}} = \boldsymbol{I}_{m_s \times m_s}. \tag{3.21}$$

Note, however, the pseudo-inverse matrix $\boldsymbol{\Psi}_{\boldsymbol{\theta}}^{+}$ is not unique, mathematically, any matrix can be used, as long as they meet the above condition.

Eqn. (3.20) can be reformulated into a PDE system for $\boldsymbol{\Psi} = \boldsymbol{\Psi}(\boldsymbol{\theta}, t)$ in Ref [27]:

$$\frac{\partial \boldsymbol{\Psi}(\boldsymbol{\theta})}{\partial t} = \left(\boldsymbol{I} - \boldsymbol{\Psi}_{\boldsymbol{\theta}}(\boldsymbol{\theta})\boldsymbol{\Psi}_{\boldsymbol{\theta}}^{+}(\boldsymbol{\theta})\right) \cdot \boldsymbol{\Phi}(\boldsymbol{\Psi}(\boldsymbol{\theta})). \tag{3.22}$$

The equation system (3.22) can be solved starting from an initial guess of the invariant manifold and continues to integrate with time t approaching to ∞, until the desired manifold is yielded. The projection operator makes the normal space of manifold vanish, which means the state space $\boldsymbol{\Psi}$, at any location of the flow field and at any time, always belongs to the invariant manifold [27]. That implies that the dynamic change of the system in the state space is completely confined to the manifold.

By differentiation of Eqn. (3.17), a set of equations are obtained with respect to the parameters. Then the evolution equation of state space can be re-written as (details see Ref. [27]):

$$\boldsymbol{\Phi}(\boldsymbol{\Psi}(\boldsymbol{\theta})) = \boldsymbol{F}(\boldsymbol{\Psi}(\boldsymbol{\theta})) - \boldsymbol{U} \cdot \boldsymbol{\Psi}_{\boldsymbol{\theta}}\nabla\boldsymbol{\theta} - \frac{1}{\rho}\nabla \cdot (\boldsymbol{D}\boldsymbol{\Psi}_{\boldsymbol{\theta}} \cdot \nabla\boldsymbol{\theta}). \tag{3.23}$$

The diffusion term in Eqn. (3.23) can be decomposed into two terms (detailed discussion see Ref. [88]), then one obtains:

$$\begin{aligned} \boldsymbol{\Phi}(\boldsymbol{\Psi}(\boldsymbol{\theta})) &= \boldsymbol{F}(\boldsymbol{\Psi}(\boldsymbol{\theta})) - \boldsymbol{U} \cdot \boldsymbol{\Psi}_{\boldsymbol{\theta}}\nabla\boldsymbol{\theta} \\ &\quad - \frac{1}{\rho}\left[\boldsymbol{D}\boldsymbol{\Psi}_{\boldsymbol{\theta}} \cdot (\nabla \cdot (\nabla\boldsymbol{\theta})) + (\boldsymbol{D}\boldsymbol{\Psi}_{\boldsymbol{\theta}})_{\boldsymbol{\theta}} \circ \boldsymbol{\chi}(\boldsymbol{\theta}) \circ \boldsymbol{\chi}(\boldsymbol{\theta})\right], \end{aligned} \tag{3.24}$$

where $\boldsymbol{\chi}(\boldsymbol{\theta}) = \nabla\boldsymbol{\theta} = \mathrm{grad}(\boldsymbol{\theta})$ is the gradient estimate of the manifold, and $\circ$ is one operator (details see Ref. [27]). Note that for simplicity we assume that the diffusion matrix is equal diffusivity, that is, $\boldsymbol{D} = d \cdot \boldsymbol{I}$. However, the REDIM method has already been validated to correctly deal with effects of detailed molecular transport in syngas/air combustion systems where non-equal diffusivity plays an important role [89]. The convection term (second term in Eqn. (3.24)) and third term of Eqn. (3.24) vanish after projecting onto its normal component with the projection operator $\boldsymbol{I} - \boldsymbol{\Psi}_{\boldsymbol{\theta}}\boldsymbol{\Psi}_{\boldsymbol{\theta}}^{+}$ due to $\boldsymbol{\Psi}_{\boldsymbol{\theta}}^{+}\boldsymbol{\Psi}_{\boldsymbol{\theta}} = \boldsymbol{I}$:

$$(\boldsymbol{I} - \boldsymbol{\Psi}_{\boldsymbol{\theta}}\boldsymbol{\Psi}_{\boldsymbol{\theta}}^{+}) \cdot (\boldsymbol{U} \cdot \boldsymbol{\Psi}_{\boldsymbol{\theta}}\nabla\boldsymbol{\theta}) = \boldsymbol{U} \cdot \left(\boldsymbol{\Psi}_{\boldsymbol{\theta}}\nabla\boldsymbol{\theta} - \boldsymbol{\Psi}_{\boldsymbol{\theta}}(\boldsymbol{\Psi}_{\boldsymbol{\theta}}^{+}\boldsymbol{\Psi}_{\boldsymbol{\theta}})\nabla\boldsymbol{\theta}\right) \equiv 0, \tag{3.25}$$

$$(\boldsymbol{I} - \boldsymbol{\Psi}_{\boldsymbol{\theta}}\boldsymbol{\Psi}_{\boldsymbol{\theta}}^{+}) \cdot (\boldsymbol{\Psi}_{\boldsymbol{\theta}} \nabla \cdot (d \nabla \boldsymbol{\theta})) \equiv 0. \tag{3.26}$$

Thus, the evolution equation for the invariant manifold can be further rewritten in a simplified form:

$$\frac{\partial \boldsymbol{\Psi}(\boldsymbol{\theta})}{\partial t} = \Big(\boldsymbol{I} - \boldsymbol{\Psi}_{\boldsymbol{\theta}}(\boldsymbol{\theta})\boldsymbol{\Psi}_{\boldsymbol{\theta}}^{+}(\boldsymbol{\theta})\Big) \cdot \left(\boldsymbol{F}(\boldsymbol{\Psi}(\boldsymbol{\theta})) - \frac{1}{\rho}(d\boldsymbol{\Psi}_{\boldsymbol{\theta}})_{\boldsymbol{\theta}} \circ \boldsymbol{\chi}(\boldsymbol{\theta}) \circ \boldsymbol{\chi}(\boldsymbol{\theta})\right). \tag{3.27}$$

If the diffusion matrix is non-equal diffusivity, the evolution equation can be given by (details in Ref. [89]):

$$\begin{aligned}\frac{\partial \boldsymbol{\Psi}(\boldsymbol{\theta})}{\partial t} &= \Big(\boldsymbol{I} - \boldsymbol{\Psi}_{\boldsymbol{\theta}}(\boldsymbol{\theta})\boldsymbol{\Psi}_{\boldsymbol{\theta}}^{+}(\boldsymbol{\theta})\Big) \\ &\cdot \left(\boldsymbol{F}(\boldsymbol{\Psi}(\boldsymbol{\theta})) - \frac{1}{\rho}\Big[\boldsymbol{D}\boldsymbol{\Psi}_{\boldsymbol{\theta}} \cdot \nabla^2 \boldsymbol{\theta} + (\boldsymbol{D}\boldsymbol{\Psi}_{\boldsymbol{\theta}})_{\boldsymbol{\theta}} \circ \boldsymbol{\chi}(\boldsymbol{\theta}) \circ \boldsymbol{\chi}(\boldsymbol{\theta})\Big]\right).\end{aligned} \tag{3.28}$$

3.3.2 Projection operator

The main focus of this proposed method is to find a suitable projection operator. To calculate the projection operator $\boldsymbol{I} - \boldsymbol{\Psi}_{\boldsymbol{\theta}}\boldsymbol{\Psi}_{\boldsymbol{\theta}}^{+}$, we should firstly define the pseudo-inverse $\boldsymbol{\Psi}_{\boldsymbol{\theta}}^{+}$. As pointed out above, mathematically, any $\boldsymbol{\Psi}_{\boldsymbol{\theta}}^{+}$ can be used for the projection as long as it fulfils the condition in Eqn. (3.21). Golda *et al.* [30] stated two methods to define the matrix $\boldsymbol{\Psi}_{\boldsymbol{\theta}}^{+}$, in which one is to use the standard Moore-Penrose pseudo-inverse, and the other is to define an $(m_s \times n)$-dimensional parametrization matrix.

The first approach is to change the manifold in normal direction to the tangential direction using the standard Moore-Penrose pseudo-inverse [73]. However, this way has a disadvantage, since enthalpy h and pressure p have different magnitudes and units comparing with specific mole numbers of species in state vector $\boldsymbol{\Psi}$, this makes orthogonality lose its direct physical meaning in the composition. Therefore, it is essential to define a positive scaling matrix so that these values of $\boldsymbol{\Psi}_{\boldsymbol{\theta}}^{+}$ are in the same order of magnitude. The pseudo-inverse with the scaling matrix can be defined as:

$$\boldsymbol{\Psi}_{\boldsymbol{\theta}}^{+} = \left(\boldsymbol{\Psi}_{\boldsymbol{\theta}}^{T}\boldsymbol{S}\boldsymbol{\Psi}_{\boldsymbol{\theta}}\right)^{-1}\boldsymbol{\Psi}_{\boldsymbol{\theta}}^{+}\boldsymbol{S}, \tag{3.29}$$

where $\boldsymbol{S}$ denotes the $(n \times n)$-dimensional scaling matrix which is diagonal and given by [89]:

$$\boldsymbol{S} = \begin{bmatrix} 10^{-12} & 0 & 0 & \cdots & 0 \\ 0 & 10^{-12} & 0 & \cdots & 0 \\ 0 & 0 & 1 & \cdots & 0 \\ \cdot & \cdot & \cdot & \cdot & \cdot \\ \cdot & \cdot & \cdot & \cdot & \cdot \\ \cdot & \cdot & \cdot & \cdot & \cdot \\ 0 & 0 & 0 & \cdots & 1 \end{bmatrix}. \tag{3.30}$$

Another approach is to define an $(m_s \times n)$-dimensional parametrization matrix $\boldsymbol{C}$. The pseudo-inverse $\boldsymbol{\Psi}_{\boldsymbol{\theta}}^{+}$ with a parametrization matrix is written by:

$$\boldsymbol{\Psi}_{\boldsymbol{\theta}}^{+} = \left(\boldsymbol{C}\boldsymbol{\Psi}_{\boldsymbol{\theta}}\right)^{-1} \boldsymbol{C}. \tag{3.31}$$

In this way, the pseudo-inverse defined by above equation, in addition to the condition in Eqn. (3.21), has to satisfy an additional condition $\boldsymbol{C}(\boldsymbol{I} - \boldsymbol{\Psi}_{\boldsymbol{\theta}}\boldsymbol{\Psi}_{\boldsymbol{\theta}}^{+}) = \boldsymbol{0}$. This means that any vector $\boldsymbol{p}$ projected onto the tangential subspace of the manifold, its coordinate in the parametrization matrix $\boldsymbol{C}$ do not change ($\boldsymbol{C}\boldsymbol{\Psi}_{\boldsymbol{\theta}}\boldsymbol{\Psi}_{\boldsymbol{\theta}}^{+} \cdot \boldsymbol{p} = \boldsymbol{C} \cdot \boldsymbol{p}$). Here, for example, one parametrization matrix is given by:

$$\boldsymbol{C} = \begin{bmatrix} 1 & 0 & 0 & \cdots & 0 \\ 0 & 0 & 1 & \cdots & 0 \end{bmatrix}, \tag{3.32}$$

in which the first and third state variables would not change after projection due to the parametrization matrix [30]. This approach intuitively shows that the direction of REDIM relaxation and evolution must coincide with the relatively rapid evolution direction of the system.

3.3.3 Initial condition and choice of progress variables

The REDIM method also needs the initial conditions which is often pre-calculated by solving a set of one-dimensional (1D) laminar flames. Actually the initial condition no matter what calculated from which flamelet scenarios is less important for the REDIM, since one only interests in the converged solution of the evolution equation (Eqn. (3.27)). The integration of Eqn. (3.27) can start from an arbitrary initial manifold, finally, the reaction system will evolve towards the invariant manifold. Note, however, that a reasonable initial guess can accelerate the convergence of Eqn. (3.27).

The other input to solve the REDIM evolution equation is the choice of reduced coordinate $\boldsymbol{\theta}$. As shown in [90], the evolution equation is invariant with respect to the reduced coordinate $\boldsymbol{\theta}$. In other words, the generation of the REDIM reduced chemistry is independent on the choice of $\boldsymbol{\theta}$. In order to verify this, results computed by the REDIM method with two different progress variables are compared in section 5.4. In the previous work, specific mole number $\phi_{\mathrm{N_2}}$ is usually selected as the first progress variable due to its monotonicity, which can be used to describe the mixing process. The choice of second progress variable is arbitrary, if it can guarantee a one-to-one mapping (no folding part) of REDIM. Figure 3.3 illustrates two sets of progress variables within 1D counterflow flamelets, $(\phi_{\mathrm{N_2}}, \phi_{\mathrm{CO_2}})^T$ and $(\phi_{\mathrm{N_2}}, \phi_{\mathrm{CO_2}} + 0.5 \cdot \phi_{\mathrm{CO}})^T$, used as the initial manifold, one of which has a folding part (see Figure 3.3a), while the other does not (Figure 3.3b).

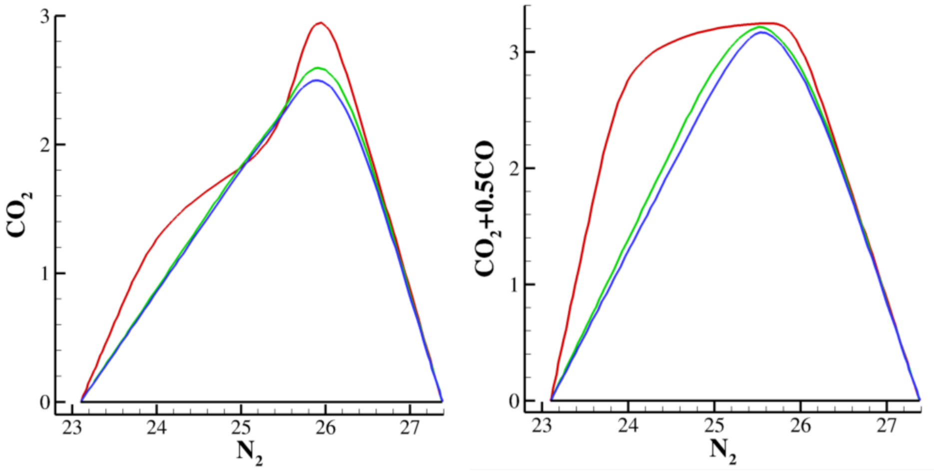

(a) (b)

Figure 3.3: 1D counterflow flamelets with the GRI3.0 mechanism projected on the specific mole number of $(\phi_{\mathrm{N_2}}, \phi_{\mathrm{CO_2}})$ (a) and $(\phi_{\mathrm{N_2}}, \phi_{\mathrm{CO_2}} + 0.5\phi_{\mathrm{CO}})$ (b) at strain rate $a = 5\ s^{-1}$ (red line), 60 s^{-1} (green line), 120 s^{-1} (blue line) and mixing line (black line).

3.3.4 Gradient estimate

The gradient estimate $\boldsymbol{\chi}(\boldsymbol{\theta}) = \nabla\boldsymbol{\theta} = \mathrm{grad}(\boldsymbol{\theta})$ must be supplied before solve the REDIM evolution equation, which is calculated via:

$$\mathrm{grad}(\boldsymbol{\theta}) = \boldsymbol{\Psi}_{\boldsymbol{\theta}}^{+}\mathrm{grad}(\boldsymbol{\Psi}). \tag{3.33}$$

The pseudo-inverse $\boldsymbol{\Psi}_{\boldsymbol{\theta}}^{+}$ is discussed in the above section, and there are three possibilities to evaluate the gradient $\mathrm{grad}(\boldsymbol{\Psi})$ [91]:

- The easiest way is to use constant values, that is, grad($\boldsymbol{\Psi}$) = constant. This method is simple and fast, but the disadvantage is that it may not be accurate enough in low-dimensional manifolds.

- The most accurate way is to compute the gradients by using DNS data, which can describe all the properties of the thermo-chemical state. However, the high computational cost of DNS is the main disadvantage of this method.

- Another way to calculate the gradients is to use the results from a set of 1D laminar flames, which can balance the accuracy and the computational cost. Therefore, this way is chosen to compute the gradient estimate in the thesis.

Bykov and Maas [27, 92] have proved, in the framework of the REDIM concept, that the gradient estimate is only important for low dimensional REDIM, and it becomes less important for higher dimensions (usually higher than three-dimensional REDIM). In this thesis, we restrict ourselves to the two-dimensional REDIM as it is sufficiently accurate for the most combustion systems [31, 89, 93, 94].

3.3.5 Boundary condition

Since the REDIM has to cover all the state space of the considered reaction system, one must define boundary conditions which correspond to boundaries of physical problem. The boundary conditions for Eqn. (3.27) in principle can be set to Dirichlet and Neumann boundary conditions [30]:

- Dirichlet boundary condition:
  $\boldsymbol{\Psi}(\boldsymbol{\theta} = \boldsymbol{\theta}_B) = \boldsymbol{\Psi}_B$, where $\boldsymbol{\theta}_B$ is the local coordinate of $\boldsymbol{\Psi}_B$ at a physical boundary point on the REDIM. The states at the Dirichlet boundary condition of the initial manifold would not change during the evolution process towards the invariant manifold. Therefore, these states located at the boundary of initial manifold require more attention. Otherwise, there would have large errors for these states at the boundary of the flame [95].

- Neumann boundary condition:
  $\boldsymbol{\Psi}_{\boldsymbol{\theta}}\text{grad}(\boldsymbol{\theta})|_{\boldsymbol{\theta}=\boldsymbol{\theta}_B} = \text{grad}(\boldsymbol{\Psi}_B)$, where if set $\text{grad}(\boldsymbol{\Psi}_B) = 0$, it follows that $\text{grad}(\boldsymbol{\theta})|_{\boldsymbol{\theta}=\boldsymbol{\theta}_B} = 0$. Therefore, Eqn. (3.27) can be transformed into the

following format via the Neumann boundary condition at the boundary of manifold [96]:

$$\frac{\partial \boldsymbol{\Psi}(\boldsymbol{\theta})}{\partial t} = \left(\boldsymbol{I} - \boldsymbol{\Psi}_{\boldsymbol{\theta}}(\boldsymbol{\theta})\boldsymbol{\Psi}_{\boldsymbol{\theta}}^{+}(\boldsymbol{\theta})\right) \cdot \boldsymbol{F}(\boldsymbol{\Psi}(\boldsymbol{\theta})). \tag{3.34}$$

The above equation shows that the source term $\boldsymbol{F}(\boldsymbol{\Psi})$ is completely dominated for the REDIM evolution equation at the boundary of manifold if implement the Neumann boundary condition.

Except the above two boundary conditions, Neagos *et al.* [96] developed the so-called “free” manifold boundaries to integrate Eqn. (3.27), which is an expansion of the invariant manifold domain. This approach is used to solve the problem that the determined manifold boundary is not large enough to describe the boundary of the actual reaction system. Details see the Refs. [30, 96].

3.3.6 Implementation procedure of the REDIM method

Once the invariant manifold is generated by solving Eqn. (3.27), the n-dimensional state vector $\boldsymbol{\Psi}$ can be accessed as a function of m_s-dimensional parametrization vector $\boldsymbol{\theta}$, i.e. a back-transformation, which can be used to recover the species and temperature profiles [72]. In order to realize the transformation, Eqn. (3.17) can be written in the following formulation by using chain rule:

$$\boldsymbol{\Psi}_{\boldsymbol{\theta}}\frac{\partial \boldsymbol{\theta}}{\partial t} = \boldsymbol{F}(\boldsymbol{\Psi}(\boldsymbol{\theta})) - \boldsymbol{U} \cdot \boldsymbol{\Psi}_{\boldsymbol{\theta}} \cdot \nabla\boldsymbol{\theta} - \frac{1}{\rho}\nabla \cdot (\boldsymbol{D} \cdot \boldsymbol{\Psi}_{\boldsymbol{\theta}} \cdot \nabla\boldsymbol{\theta}), \tag{3.35}$$

and by multiplying both sides with the pseudo-inverse $\boldsymbol{\Psi}_{\boldsymbol{\theta}}^{+}$, one obtains the reduced model equation:

$$\frac{\partial \boldsymbol{\theta}}{\partial t} = \boldsymbol{\Psi}_{\boldsymbol{\theta}}^{+} \cdot \boldsymbol{F}(\boldsymbol{\Psi}(\boldsymbol{\theta})) - \boldsymbol{U} \cdot \nabla\boldsymbol{\theta} - \frac{1}{\rho}\boldsymbol{\Psi}_{\boldsymbol{\theta}}^{+} \cdot \nabla \cdot (\boldsymbol{D}\boldsymbol{\Psi}_{\boldsymbol{\theta}} \cdot \nabla\boldsymbol{\theta}). \tag{3.36}$$

Finally, we can summarize the application procedure of the REDIM method in the following several steps [27]:

- specify the initial condition, choose the suitable parametrization vector $\boldsymbol{\theta}$, and define the boundary condition for Eqn. (3.27);
- supply the gradient estimate grad($\boldsymbol{\theta}$) as a function of the parameter $\boldsymbol{\theta}$ for the evolution equation;

- integrate Eqn. (3.27) in time $t \to \infty$ until a stationary solution $\boldsymbol{\Psi}(\boldsymbol{\theta})$ is obtained;
- store the data of $\boldsymbol{\theta}, \boldsymbol{\Psi}(\boldsymbol{\theta})$, $\boldsymbol{\Psi}_{\boldsymbol{\theta}}$, $\boldsymbol{\Psi}_{\boldsymbol{\theta}}^{+}$, $\boldsymbol{D}\boldsymbol{\Psi}_{\boldsymbol{\theta}}$ and $\boldsymbol{\Psi}_{\boldsymbol{\theta}}^{+}\boldsymbol{F}$, so that it can be used in Eqn. (3.36).

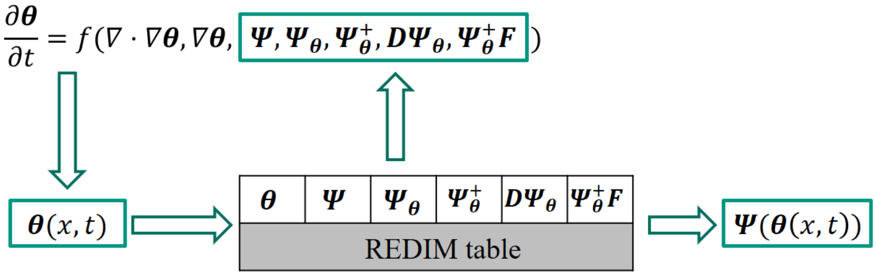

Figure 3.4: Flow chart for the implementation procedure of REDIM [29, 30].

Figure 3.4 shows the complete flow chart for implementation procedure of the REDIM method. The REDIM is constructed according to Eqn. (3.27). The detailed construction of REDIM will be introduced in the following section. The terms $\boldsymbol{\Psi}(\boldsymbol{\theta})$, $\boldsymbol{\Psi}_{\boldsymbol{\theta}}$, $\boldsymbol{\Psi}_{\boldsymbol{\theta}}^{+}$, $\boldsymbol{D}\boldsymbol{\Psi}_{\boldsymbol{\theta}}$ and $\boldsymbol{\Psi}_{\boldsymbol{\theta}}^{+}\boldsymbol{F}$ are computed as functions of the local coordinates $\boldsymbol{\theta}$ in a modified and extended version of HOMREA [49]. We solve the Eqn. (3.36) and obtain the values of $\boldsymbol{\theta}(x,t)$ in the simulation. Finally, $\boldsymbol{\Psi}(\boldsymbol{\theta}(x,t))$ is assigned by the $\boldsymbol{\theta}(x,t)$ using the REDIM lookup table. Note that Eqn. (3.36) yields the solution $\boldsymbol{\theta}(x,t)$ in the physical space.

3.3.7 Construction of REDIM for a counterflow methane/air flame

This section will provide a detailed guide on how to create REDIM tables, which will help to gain a more intuitive understanding of the REDIM method. To illustrate the process, we will use a typical example of a 1D laminar counterflow methane/air flame. A stream of methane mixed with air is injected from the left boundary while a stream of air is injected from the right boundary. The detailed boundary conditions used to calculate the counterflow flame are listed in table 3.1.

In order to generate the REDIM tables, firstly we need to compute detailed solutions of different flame scenarios following the suggestions in Ref. [28]. These flame scenarios are a set of 1D counterflow flames with different strain

Table 3.1: Boundary conditions for 1D counterflow flame.

	T	p	composition in volume percent
Left boundary	293 K	1 bar	25 % CH4 + 75 % air
Right boundary	293 K	1 bar	21 % O2 + 79 % N2

rates in this example, which include reactive solutions and simple diffusion solutions. The generation procedure of REDIM has been implemented in the INSFLA and HOMREA codes [49]. Schießl *et al.* [94] compared the REDIMs generated by the one- or multi-dimensional gradient estimates from the DNS data and proved that gradient estimates have minor influence for the REDIMs in counterflow flames. Therefore, the REDIM obtained from the gradient estimate computed by 1D counterflow flames can also accurately describe simulations with multi-dimensional transport. As mentioned above, the REDIM table is obtained by solving Eqn. (3.27). To solve the equation, one must specify the initial condition, boundary conditions and, in addition, the gradient estimate grad($\boldsymbol{\theta}$).

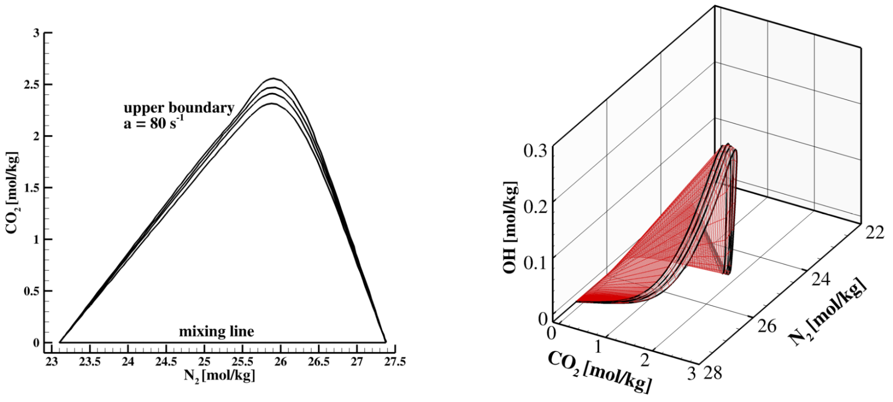

(a) **(b)**

Figure 3.5: Initial condition computed by the GRI3.0 mechanism for the construction of REDIM, flamelets at strain rate a = 80 s^{-1}, 140 s^{-1}, 200 s^{-1}, 300 s^{-1} and mixing line (a), linear interpolation between flamelets (b).

The initial condition has been taken from stationary solutions of 1D counterflow flames. These stationary solutions are calculated with different strain rates by the in-house program INSFLA. The strain rate a is an important quantity used to characterize 1D counterflow flames, which is defined and computed in Ref. [97]:

$$a = \sqrt{-\frac{J}{\rho_{ub}}}, \tag{3.37}$$

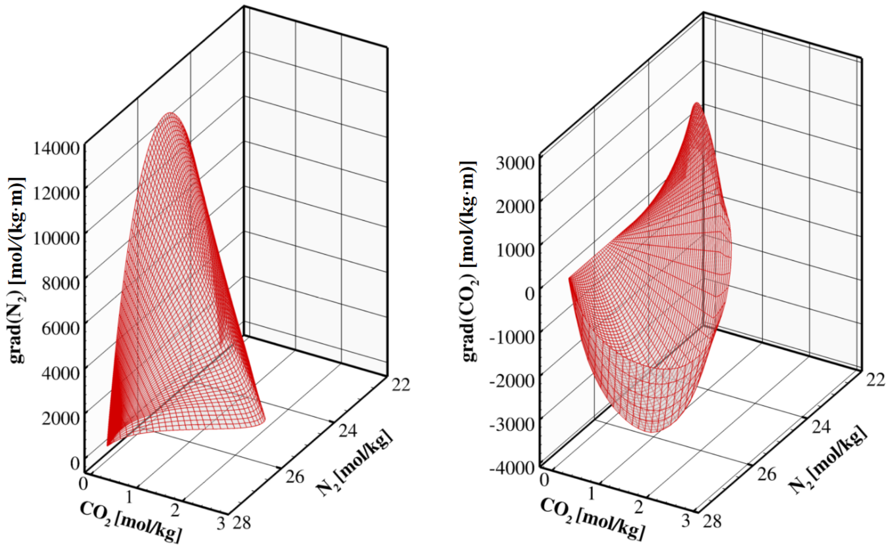

(a) (b)

Figure 3.6: Gradient estimate computed from 1D counterflow flamelets with the GRI3.0 mechanism for the construction of REDIM, grad(N_2) by (ϕ_{N_2}, ϕ_{CO_2}) (a), grad(CO_2) by (ϕ_{N_2}, ϕ_{CO_2}) (b).

where J denotes the tangential pressure gradient, and ρ_{ub} is the density of the unburnt fuel mixture.

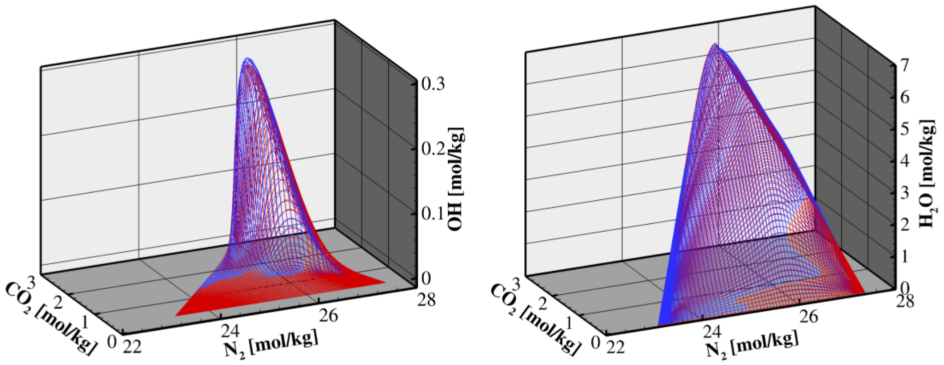

(a) (b)

Figure 3.7: Composition space of the 2D REDIM reduced chemistry in (ϕ_{N_2}, ϕ_{CO_2}) projection, OH (a) and H_2O (b).

Figure 3.5a shows the boundary conditions and initial conditions taken from a collection of counterflow flames with different strain rates computed with the GRI3.0 mechanism. The upper boundary is one stationary solution with low strain rate of 80 s^{-1}. The pure mixing line is defined by the unburnt mixtures, that is, inert counterflow diffusion solution, which defines the lower boundary of the application range of REDIM. The upper and lower boundaries include all possible flame scenarios in this work, consisting of both stable and unstable (extinction) flame regimes [31]. The boundaries of the manifold are specified as Dirichlet boundary conditions from the detailed flame calculation. Except the flame scenarios for boundaries of REDIM, the other stationary solutions with different strain rates ($a = 100, 120, 140, 160, 180, 200, 300$ s^{-1}) are selected in this work. Any other states between two flamelets (represented by 3 black lines in Figure 3.5 as an example) can be computed by a simple linear interpolation (red mesh), which is shown in Figure 3.5b. Figure 3.5a is the projection of Figure 3.5b on the specific mole number N_2 and CO_2 plane (the red mesh is not shown). The selection of initial solutions is arbitrary in theory, however, a reasonable initial guess can accelerate the convergence of Eqn. (3.27). In order to prove this point, we used different initial guess to generate REDIMs, that is, one REDIM (red mesh in Figure 3.7) is generated by the more flamelets ($a = 80, 100, 120, 140, 160, 180, 200, 300$ s^{-1} and mixing line), and the other REDIM (blue mesh in Figure 3.7) is generated by only two flamelets ($a = 80$ s^{-1} and mixing line). Comparing the two REDIM manifolds, one can see that there are only slight differences between the meshes, however the convergence time in the REDIM with two flamelets is approximately 3 times than the REDIM with the reasonable initial guess in this work. Moreover, we do not need to provide the extinction regime in the generation of REDIM, while the REDIM method can still describe the extinction process very well (details see section 5.6.2).

Figure 3.6 shows that the gradient estimates for grad(N_2) and grad(CO_2) by (ϕ_{N_2}, ϕ_{CO_2}) used for the 2D REDIM are calculated by the 1D counterflow flamelets obtained with the GRI3.0 mechanism. Figure 3.7 shows the examples of composition space of the 2D REDIM reduced chemistry in (ϕ_{N_2}, ϕ_{CO_2}) projection (GRI3.0 mechanism is used in the simplification).

4 Implementation of detailed and reduced chemistry in OpenFOAM

4.1 EBIdnsFoam

As introduced in section 2.3.3, OpenFOAM is a versatile, flexible, and easy to extend toolkit for the calculation of CFD, which has several solvers dedicated to solving the combustion problems [53]. Note, however, that these solvers for the simulation of combustion based on OpenFOAM have some disadvantages. For example, there is no detailed transport models to simulate process of molecular diffusion. Moreover, the computational expense associated with computing chemical reaction rates in finite rate models used by the solvers in OpenFOAM for ordinary differential equations (ODE) is much higher than that of other ODE solvers.

In order to overcome the above disadvantages of OpenFOAM solvers for combustion system, Zirwes *et al.* developed the EBI-DNS solver (also known as EBIdnsFoam) which can solve combustion problems both accurately and efficiently [98–100]. The first version was developed in 2012 [101] and has since been refined and improved. The EBIdnsFoam solver couples Cantera that is an open-source suite of tools for problems involving chemical kinetics, thermodynamics, and transport processes to OpenFOAM. The coupling process between OpenFOAM and Cantera is shown in Figure 4.1. OpenFOAM is used to solve the governing equations (e.g. total mass, momentum, energy and species conservation equations and equation of state) and supplies the results of pressure, temperature and species mass fractions to the Cantera. The Cantera part in the solver is used to compute transport properties (e.g. molecular viscosity, thermal conductivity, and heat capacity) derived from rigorous kinetic gas theory and reaction rates using an operator splitting technique [98]. This means the reaction mechanism based on Cantera's xml format can be provided to the EBIdnsFoam solver. The only external dependency SUNDIALS (SUite of Nonlinear and DIfferential/ALgebraic equation Solvers) CVODE solver [102] is used to integrate the chemical reaction source term (see section 4.1.4).

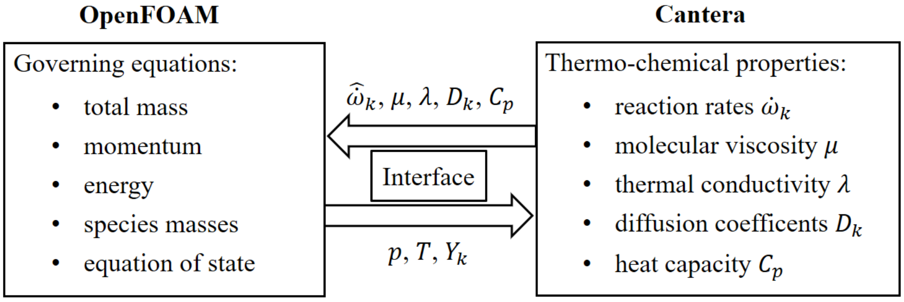

Figure 4.1: Coupling process between OpenFOAM and Cantera [99].

4.1.1 Governing equations used in EBIdnsFoam

The system of governing equations (refers to section 2.2 for detailed information) used in EBIdnsFoam solver is written as:

- Continuity equation:

$$\frac{\partial \rho}{\partial t} + \nabla \cdot (\rho \boldsymbol{U}) = 0. \tag{4.1}$$

- Species mass fraction equation:

$$\frac{\partial (\rho Y_k)}{\partial t} + \nabla \cdot (\rho Y_k (\boldsymbol{U} + \boldsymbol{U}_c)) + \nabla \cdot \boldsymbol{j}_k = \hat{\dot{\omega}}_k, \quad k = 1, ..., n_s \tag{4.2}$$

  where n_s is the number of species in the reacting system and $\hat{\dot{\omega}}_k$ is the time step averaged reaction rate (details see section 4.1.4).

- Momentum conservation equation:

$$\begin{aligned}\frac{\partial (\rho \boldsymbol{U})}{\partial t} =& - \nabla \cdot (\rho \boldsymbol{U} \otimes \boldsymbol{U}) + \nabla \cdot \left[\mu \left(\nabla \otimes \boldsymbol{U} + (\nabla \otimes \boldsymbol{U})^T - \frac{2}{3} (\nabla \cdot \boldsymbol{U}) \boldsymbol{I} \right) \right] \\ & - \nabla p + \rho \mathbf{g}.\end{aligned} \tag{4.3}$$

- Energy conservation equation:

$$\begin{aligned}\frac{\partial(\rho h_s)}{\partial t} + \nabla\cdot(\rho \boldsymbol{U} h_s) = &- \frac{\partial(\rho K)}{\partial t} - \nabla\cdot(\rho \boldsymbol{U} K) + \nabla\cdot(\lambda\nabla T) \\ &- \nabla\cdot(\sum_{k=1}^{n_s} h_{sk}\hat{\boldsymbol{j}}_k) - \nabla\cdot[\boldsymbol{\tau}\cdot\boldsymbol{U}] + \frac{\partial p}{\partial t} \\ &+ \rho(\boldsymbol{U}\cdot\mathbf{g}) + \dot{\omega}_T + \nabla\cdot\boldsymbol{q}_{\mathrm{rad}}.\end{aligned} \tag{4.4}$$

  The temperature is calculated from the sensible enthalpy via the heat capacity using Newton's method.

- Equation of state for ideal gases:

$$\rho = \frac{p\bar{M}}{RT}. \tag{4.5}$$

4.1.2 Diffusion models

The mixture-averaged diffusion model (Hirschfelder and Curtiss approximation) is applied to the calculations in the thesis. By employing this approximation, the Maxwell–Stefan equations can be simplified, resulting in a closed expression for the species diffusion flux density $\boldsymbol{j}_k$ [103]:

$$\boldsymbol{j}_k = -\rho D_k \nabla Y_k - \frac{D_k^T}{T}\nabla T, \tag{4.6}$$

where D_k is the diffusion coefficient of species k into the rest of the mixture and D_k^T represents the thermal diffusion coefficient of species k. The second term in Eqn. (4.6) is the thermal diffusion (Soret effect), which is often neglected in most situations, because it is non-negligible only for light species (H, H_2, He, etc.) and at low temperature [11]. Thus, the species diffusion flux density can be further written as:

$$\boldsymbol{j}_k = -\rho D_k \nabla Y_k. \tag{4.7}$$

The formulation of the mixture-average diffusion coefficient of species D_k in the gas mixture is defined as:

$$D_k = \left(\sum_{j\neq k}\frac{X_j}{\mathcal{D}_{kj}} + \frac{X_k}{1-Y_k}\sum_{j\neq k}\frac{Y_j}{\mathcal{D}_{kj}}\right). \tag{4.8}$$

where $X_k = Y_k\frac{\bar{M}}{M_k}$ denotes mole fraction of species k and $\mathcal{D}_{kj}$ is the binary diffusion coefficient [103]. However, because the diffusion coefficients involves binary diffusion coefficients and still need highly computational effort, most combustion codes use simplified diffusion laws. Thus, the diffusion coefficient D_k is often defined in terms of Lewis number by [11]:

$$Le_k = \frac{\lambda}{\rho C_p D_k}, \tag{4.9}$$

where C_p is the heat capacity at constant pressure. If the assumption of unity Lewis number ($Le_k = 1$) is used, one can obtain:

$$D_k = \frac{\lambda}{\rho C_p}, \tag{4.10}$$

which means that the diffusion coefficient of each species k is equal in simulation, that is, $D = D_k$ [8, 11].

4.1.3 Thermodynamic properties

Thermodynamic properties of species k (e.g. specific molar heat capacity at constant pressure $\bar{C}_{pk}$, specific molar enthalpy $\bar{h}_k$, specific molar entropy $\bar{s}_k$) are usually tabulated as function of the temperature. JANAF polynomials are the thermodynamic functions used to calculate the thermodynamic properties [104]:

$$\frac{\bar{C}_{pk}}{R} = a_{k,0} + a_{k,1}T + a_{k,2}T^2 + a_{k,3}T^3 + a_{k,4}T^4, \tag{4.11}$$

$$\frac{\bar{h}_k}{R} = a_{k,0}T + \frac{a_{k,1}}{2}T^2 + \frac{a_{k,2}}{3}T^3 + \frac{a_{k,3}}{4}T^4 + \frac{a_{k,4}}{5}T^5 + a_{k,5}, \tag{4.12}$$

$$\frac{\bar{s}_k}{R} = a_{k,0}\ln T + a_{k,1}T + \frac{a_{k,2}}{2}T^2 + \frac{a_{k,3}}{3}T^3 + \frac{a_{k,4}}{4}T^4 + a_{k,6}. \tag{4.13}$$

Two different polynomials with two sets of seven coefficients ($a_{k,0} - a_{k,6}$) are used for high and low temperature ranges which are separated by a intermediate temperature, usually $T = 1000$ K [7]. The specific mass values of the thermodynamic properties are calculated from:

$$C_{pk} = \frac{\bar{C}_{pk}}{M_k}, \quad h_k = \frac{\bar{h}_k}{M_k}, \quad s_k = \frac{\bar{s}_k}{M_k}. \tag{4.14}$$

The thermodynamic properties for mixture are computed by:

$$C_p = \sum_k Y_k C_{pk} = \frac{1}{\bar{M}} \sum_k X_k \bar{C}_{pk}, \tag{4.15}$$

$$h = \sum_k Y_k h_k = \frac{1}{\bar{M}} \sum_k X_k \bar{h}_k, \tag{4.16}$$

$$s = \sum_k Y_k s_k = \frac{1}{\bar{M}} \sum_k X_k \bar{s}_k. \tag{4.17}$$

4.1.4 Operator splitting technique

As discussed in section 3.2 (shown in Figure 3.1), the fast time scale of chemical reaction is approximately 10^{-10} s which is usually much smaller than the time scale of physical processes without reaction. This means that OpenFOAM needs to use much smaller time step in the governing equations for a reactive flow, in order to sufficiently resolve the chemical reaction source terms. However, this process requires extremely highly computational cost. To solve the problem, an operator splitting technique is implemented in the EBIdnsFoam solver, in which each control volume (or cell) in the computational domain is regarded as a closed isovolumetric zero-dimensional batch reactor. There are two different time steps used in the solver, one of which is the CFD time step used by OpenFOAM (Δt_{OF}), and the other is much smaller time step that is adaptively selected by the SUNDIALS ($\Delta t_{\mathrm{SUNDIALS}}$). Before solving the conservation equations, the SUNDIALS CVODE uses the time step $\Delta t_{\mathrm{SUNDIALS}}$ to integrate the reaction rates over the CFD time step in each control volume assuming that there is no diffusion or convection [99, 105].

The system of ordinary differential equations (ODE) consisting of n_s species equations and one energy equation, is integrated by SUNDIALS [99]:

$$\int_{Y_k(t_0)}^{Y_k(t_0+\Delta t_{\mathrm{OF}})} dY_k = \int_{t_0}^{t_0+\Delta t_{\mathrm{OF}}} \frac{\dot{\omega}_k}{\rho} dt, \quad k = 1...n_s \tag{4.18}$$

$$\int_{T(t_0)}^{T(t_0+\Delta t_{\mathrm{OF}})} dT = \int_{t_0}^{t_0+\Delta t_{\mathrm{OF}}} -\frac{\sum_k \dot{\omega}_k e_k}{\rho C_v} dt, \tag{4.19}$$

where $C_v = C_p - \frac{R}{\bar{M}}$ and e_k is the partial specific internal energy of species k, that can be computed by the following equation for ideal gas:

$$e_k = \frac{\bar{e}_k}{M_k} = \frac{1}{M_k}(\bar{h}_k - RT). \tag{4.20}$$

Finally, a time step averaged reaction rate used in the species governing equations (4.2) can be computed by the species mass fractions $Y_k(t_0)$ and $Y_k(t_0 + \Delta t_{\mathrm{OF}})$ [99]:

$$\hat{\dot{\omega}}_k = \rho \frac{\partial Y_k}{\partial t} \approx \rho \frac{Y_k(t_0 + \Delta t_{\mathrm{OF}}) - Y_k(t_0)}{\Delta t_{\mathrm{OF}}}, \tag{4.21}$$

where the species mass fraction $Y_k(t_0 + \Delta t_{\mathrm{OF}})$ is computed by the above integration with SUNDIALS.

4.2 Validation of EBIdnsFoam solver

4.2.1 Problem definition

The aim of this section is to validate the EBIdnsFoam solver by simulating an axisymmetric laminar coflow diffusion flame, which involves the combustion of nitrogen-diluted methane mixture [106, 107]. A schematic of the burner is shown in Figure 4.2. The study will include the influence of gravity, detailed transport model and optically thin radiation model. The fuel mixture (65 % CH_4 and 35 % N_2 in volume percent) is injected into a coflow air stream (21 % O_2 and 79 % N_2 in volume percent). The computational temperature, mole fractions of major and minor species and NO with the solver are compared to the corresponding results in Ref. [107].

4.2.2 Numerical set-up

The computational domain is two-dimensional and takes advantage of axisymmetry, which has dimension $\mathrm{R_{MAX}} = 5.0$ cm at radial extent (y-direction) and $\mathrm{L_{MAX}} = 20.0$ cm at axial extent (x-direction). The velocity profile of the inner tube is assumed to be parabolic, which can be defined by the following form [107]:

$$U = 0.76 \cdot [1 - (\frac{y}{\mathrm{R_I}})^2] \text{ m/s}. \tag{4.22}$$

In the oxidizer stream, the velocity profile is assumed to be flat, and setting to 0.3563 m/s. Both the streams are at 298 K and the ambient air pressure is set to 1 bar. The dead zone which surrounds the outer tube contains pure air (298 K) and the velocity is 0 there. The GRI3.0 reaction mechanism is used to calculate the 2D jet flame in the section.

The mixture-averaged diffusion model is selected to calculate the diffusion coefficient D_k in the EBIdnsFoam solver. The study excludes the Soret and

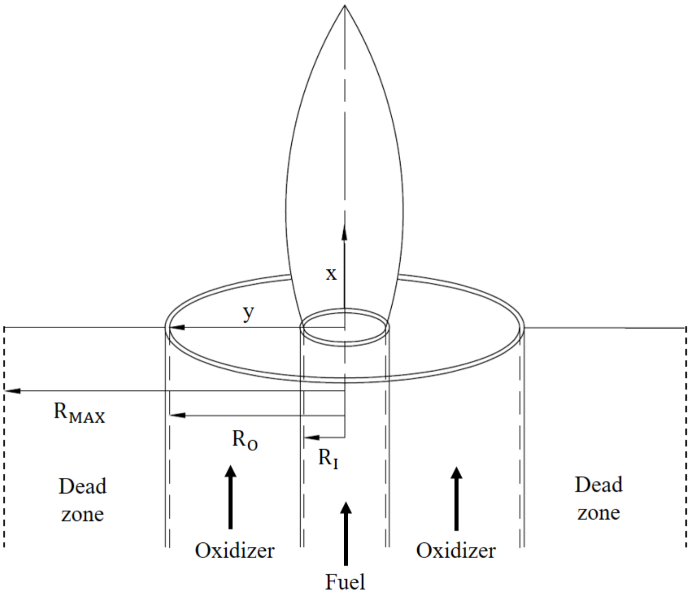

Figure 4.2: Schematic of 2D jetflow flame configuration with dead zone. The inner tube radius is $R_I = 0.2$ cm and the wall thickness of the tube is 0.04 cm. The outer tube radius is $R_O = 2.5$ cm.

Dufour effects. An optically thin radiation model with three radiating species (H_2O, CO and CO_2) is taken into account in the calculation [108, 109]. Based on the optically thin assumption, the radiative heat loss term can be written as [110]:

$$\nabla \cdot \boldsymbol{q}_{\text{rad}} = 4\sigma(T^4 - T_b^4)\sum_i (p_i a_{pi}), \tag{4.23}$$

where σ is the Stefan-Boltzmann constant, T is the local flame temperature, T_b denotes the environment temperature, p_i represents the partial pressure of species i in atmospheres and a_{pi} is the Planck mean absorption coefficient of species i.

4.2.3 Simulation results

Figure 4.3 shows computed isotherms and isopleths of selected species for the EBIdnsFoam solver and the computational results with the GRI3.0 mechanism reported in [107]. The peak temperatures are 1941 K and 1956 K for the solver and computations in Ref. [107], respectively. It can be seen that the results for temperature, mole fractions of selected major species (CH_4 and O_2) and minor species (OH and NO) calculated by the EBIdnsFoam solver

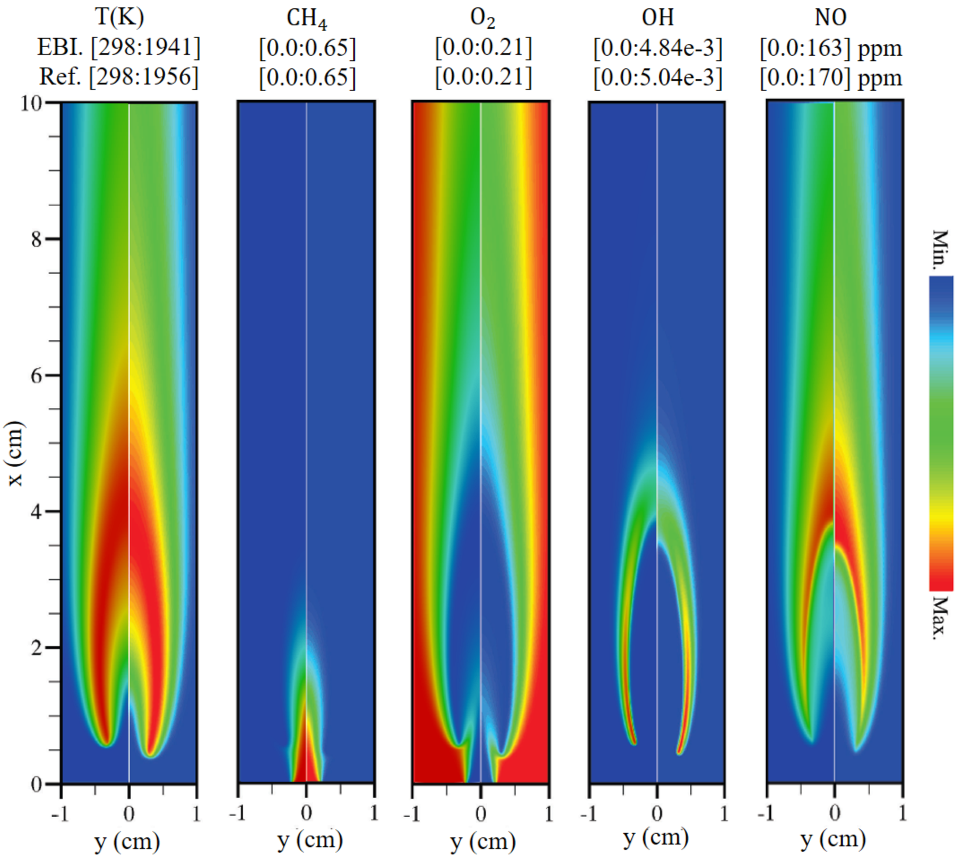

Figure 4.3: Computed isotherms and isopleths of selected species in mole fractions, left half of each plot: EBIdnsFoam, right half of each plot: computational data in Ref. [107].

have a very good agreement with the corresponding computed data in the literature. The EBIdnsFoam can describe the flame structure and the flame lifting phenomenon very well. An important feature of lifted flames is the presence of small amount of oxygen that leaks into the fuel-rich side, which is observed in both results. Liftoff heights and flame lengths (definitions see section 6.3.2) are listed in table 4.1. In comparison with the computational results in the literature, the liftoff height obtained by the EBIdnsFoam is closer to the experimental value. However, the computed flame height is overestimated with respect to the computational data and nearly one third of the 0.33 cm difference is due to this 0.13 cm difference in calculated liftoff height.

Figure 4.4 displays radial profiles of selected species and temperature at two different values of ζ (details see Ref. [107] or section 6.3.4). It is shown

Table 4.1: Comparison of calculated and measured liftoff heights and flame lengths (cm).

	Com. data in [107]	EBIdnsFoam	Exp. data in [107]
Liftoff heights	0.40	0.53	0.66
Flame lengths	3.75	4.08	3.24

that the profiles of $\zeta = 0.225$ in Figure 4.4a, which locates approximately one-fifth of the way up the flame. The peak temperatures along the radial profiles from the EBIdnsFoam solver and the computational results in the literature are approximately 1937 K and 1950 K, respectively. The figure also indicates the presence of oxygen on the fuel-rich side, attributed to the oxygen leakage, and while its value is small, but not negligible. Other major species (CH_4, H_2O, CO_2 and N_2) are correctly calculated by the EBIdnsFoam solver, comparing with the computational and experimental data reported in the literature. In Figure 4.4b, where $\zeta = 1.125$, the fuel is consumed completely. The temperature and products level off on the centerline and decrease as y increases, while O_2 increases to 0.21 in the coflow stream. The radial profiles of temperature and major species computed by the solver agree quite well with the computational and experimental results in Ref. [107] in the figures.

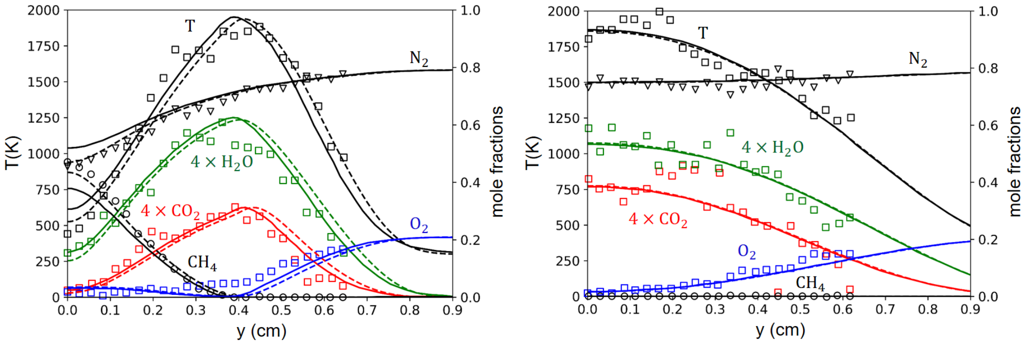

(a) **(b)**

Figure 4.4: Radial profiles of selected species and temperature. Solid line: computational results in Ref. [107], dashed line: EBIdnsFoam, symbols: experimental results in Ref. [107]. (a) $\zeta = 0.225$, computational $y = 1.153$ cm, EBIdnsFoam $y = 1.329$ cm, experimental $y = 1.24$ cm and (b) $\zeta = 1.125$, computational $y = 4.269$ cm, EBIdnsFoam $y = 4.630$ cm, experimental $y = 3.64$ cm.

Consequently, the reliability and accuracy of the EBIdnsFoam solver for calculating laminar coflow flames is demonstrated by the excellent agreement between the results obtained from the solver and those reported in the literature.

4.3 REDIMFoam

4.3.1 REDIMFoam based on generalized coordinates

The system of governing equations used in REDIMFoam solver can be written as:

- Continuity equation (4.1):

$$\frac{\partial \rho}{\partial t} + \nabla \cdot (\rho \boldsymbol{U}) = 0.$$

- Reduced model equations for m_s-dimensional parametrization vector $\boldsymbol{\theta}$ is derived by combining Eqn. (3.36) with the continuity equation:

$$\frac{\partial (\rho \boldsymbol{\theta})}{\partial t} + \nabla \cdot (\rho \boldsymbol{U} \cdot \boldsymbol{\theta}) + \boldsymbol{\Psi}_{\boldsymbol{\theta}}^{+} \cdot \nabla \cdot (\boldsymbol{D} \boldsymbol{\Psi}_{\boldsymbol{\theta}} \cdot \nabla \boldsymbol{\theta}) = \rho \boldsymbol{\Psi}_{\boldsymbol{\theta}}^{+} \cdot \boldsymbol{F}(\boldsymbol{\Psi}(\boldsymbol{\theta})). \quad (4.24)$$

- Momentum conservation equation (4.3):

$$\begin{aligned} \frac{\partial (\rho \boldsymbol{U})}{\partial t} = & - \nabla \cdot (\rho \boldsymbol{U} \otimes \boldsymbol{U}) + \nabla \cdot \left[\mu \left(\nabla \otimes \boldsymbol{U} + (\nabla \otimes \boldsymbol{U})^T - \frac{2}{3} (\nabla \cdot \boldsymbol{U}) \boldsymbol{I} \right) \right] \\ & - \nabla p + \rho \mathbf{g}. \end{aligned}$$

- Equation of state for ideal gases (4.5):

$$\rho = \frac{p \bar{M}}{RT}.$$

According to the above system of governing equations, there are only $(3 + m_s)$ equations ($m_s \ll n_s$) solved in the REDIM approach, namely Eqn. (4.1), Eqn. (4.3), Eqn. (4.5), and m_s θ-equations (4.24). If here $m_s = 2$, that is, $\boldsymbol{\theta} = (\theta_1, \theta_2)^T$, then there are 2 θ-equations computed in the REDIMFoam solver:

$$\frac{\partial (\rho \theta_1)}{\partial t} + \nabla \cdot (\rho \boldsymbol{U} \theta_1) + \boldsymbol{\Psi}_{\theta_1}^{+} \cdot \nabla \cdot (\boldsymbol{D} \boldsymbol{\Psi}_{\theta_1} \cdot \nabla \theta_1) = \rho \boldsymbol{\Psi}_{\theta_1}^{+} \cdot \boldsymbol{F}(\boldsymbol{\Psi}(\theta_1)), \quad (4.25)$$

$$\frac{\partial (\rho \theta_2)}{\partial t} + \nabla \cdot (\rho \boldsymbol{U} \theta_2) + \boldsymbol{\Psi}_{\theta_2}^{+} \cdot \nabla \cdot (\boldsymbol{D} \boldsymbol{\Psi}_{\theta_2} \cdot \nabla \theta_2) = \rho \boldsymbol{\Psi}_{\theta_2}^{+} \cdot \boldsymbol{F}(\boldsymbol{\Psi}(\theta_2)). \quad (4.26)$$

The numerical solution of REDIM generates an m_s-dimensional mesh in the different coordinate directions and the evolution equation (3.27) is solved on the nodes of the mesh cell by cell [111]. Then, the m_s-dimensional manifold is described by the grid indices (see Figure 4.5), which are called generalized coordinates θ [72]. The advantage of using generalized coordinates is perfectly accommodated to the reaction progress on the simplified manifold and uniqueness is guaranteed [72]. Furthermore, the generalized coordinates can also improve the efficiency of interpolation calculation during the implementation of REDIM, since the structure of the grid is locally orthogonal and equidistant everywhere, which can avoid the point-by-point search.

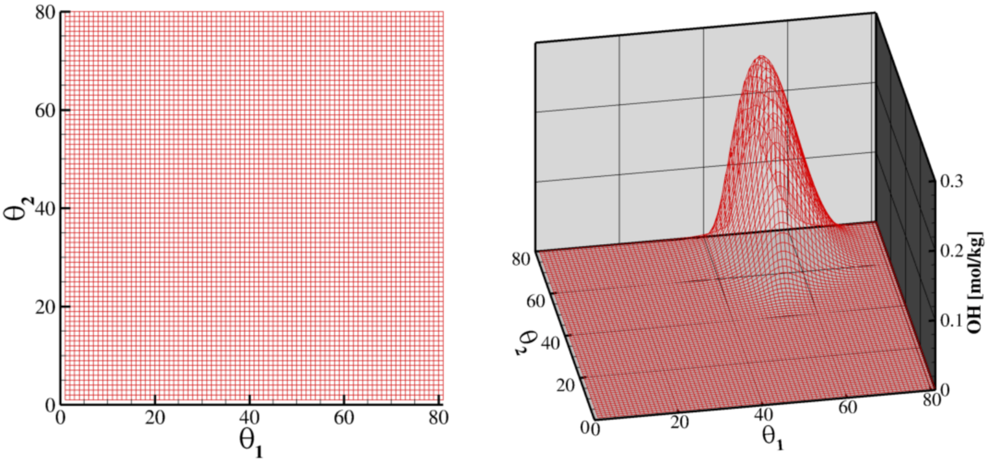

(a) **(b)**

Figure 4.5: Grid indices of a 2D REDIM table based on the generalized coordinates, 2D projection of manifold in the generalized coordinates θ (a), 3D projection of OH profile (b).

As discussed in section 3.3, the REDIM table has been generated in a preprocessing stage, and the terms $\boldsymbol{\Psi}(\boldsymbol{\theta})$, $\boldsymbol{\Psi}_{\boldsymbol{\theta}}$, $\boldsymbol{\Psi}_{\boldsymbol{\theta}}^{+}$, $\boldsymbol{D}\boldsymbol{\Psi}_{\boldsymbol{\theta}}$ and $\boldsymbol{\Psi}_{\boldsymbol{\theta}}^{+}\boldsymbol{F}$ are computed at each mesh point and stored in the table beforehand. The next stage is implementation of the system of the governing equations in OpenFOAM. The REDIMFoam solver is created by solving the system of governing equations based on the version v2006 of OpenFOAM [112]. We can summarize the full implementation scheme of the REDIM method with OpenFOAM into the following steps:

- obtain the terms $\boldsymbol{\Psi}_{\boldsymbol{\theta}}^{+}$, $\boldsymbol{D}\boldsymbol{\Psi}_{\boldsymbol{\theta}}$ and $\boldsymbol{\Psi}_{\boldsymbol{\theta}}^{+}\boldsymbol{F}$ by a simple linear interpolation method in the REDIM table depending on the generalized coordinates;

- calculate the m_s-dimensional vector $\nabla\boldsymbol{\theta}$;
- compute the n-dimensional transport term $\nabla \cdot (\boldsymbol{D}\boldsymbol{\Psi}_{\boldsymbol{\theta}} \cdot \nabla\boldsymbol{\theta})$ and the term for the reduced coordinate of the m_s-dimensional reduced manifold $\boldsymbol{\Psi}_{\boldsymbol{\theta}}^{+} \cdot \nabla \cdot (\boldsymbol{D}\boldsymbol{\Psi}_{\boldsymbol{\theta}} \cdot \nabla\boldsymbol{\theta})$;
- supply the results of $\boldsymbol{\Psi}_{\boldsymbol{\theta}}^{+} \cdot \nabla \cdot (\boldsymbol{D}\boldsymbol{\Psi}_{\boldsymbol{\theta}} \cdot \nabla\boldsymbol{\theta})$ and $\boldsymbol{\Psi}_{\boldsymbol{\theta}}^{+}\boldsymbol{F}$ to Eqn. (4.24) and solve the equation.

Finally, after solving Eqn. (4.24) in each time step, a back-transformation of the solution $\boldsymbol{\theta}(x_i, t)$ to detailed variable $\boldsymbol{\Psi}(\boldsymbol{\theta}(x_i, t))$ is assigned by performing another linear interpolation in the REDIM lookup table [27, 72]. Note that the primary solution $\boldsymbol{\theta}(x_i, t)$ is spatial profiles of the generalized coordinates, and other thermo-chemical quantities (e.g. temperature, species mass fractions) can be retrieved by the back-transformation from the REDIM table.

4.3.2 REDIMFoam based on physical coordinates

In the above section, we introduced the implementation of REDIM in generalized coordinates. It should be pointed out that the main disadvantage of using generalized coordinates to simulate combustion with REDIM is the lack of simple and transparent physical meaning. This means that it is difficult to interpret the obtained results. Therefore, some researchers [34, 113, 114] prefer to perform calculations in physical coordinates $\boldsymbol{\xi}$ which can be realized by a constant parametrization matrix $\boldsymbol{C}$. The parametrization matrix defines the constant linear combination of variables in state space, $\boldsymbol{\xi} = \boldsymbol{C} \cdot \boldsymbol{\Psi}$ [115]. For example, if the state vector consists of the following variables $\boldsymbol{\Psi} = (h, p, \phi_{\mathrm{N_2}}, \phi_{\mathrm{CO_2}}, \phi_{\mathrm{CO}}, \cdots, \phi_{\mathrm{H}})^T$, and the parametrization matrix is given by:

$$\boldsymbol{C} = \begin{bmatrix} 0 & 0 & 1 & 0 & 0 & \cdots & 0 \\ 0 & 0 & 0 & 1 & 0.5 & \cdots & 0 \end{bmatrix}, \quad \boldsymbol{\xi} = \begin{pmatrix} \phi_{\mathrm{N_2}} \\ \phi_{\mathrm{CO_2}} + 0.5\phi_{\mathrm{CO}} \end{pmatrix}, \tag{4.27}$$

then the parameters $\xi_1 = \phi_{\mathrm{N_2}}$ and $\xi_2 = \phi_{\mathrm{CO_2}} + 0.5\phi_{\mathrm{CO}}$. This can be very simple for post-processing of results and convenient to monitor the integration process. However, it can be challenging to find an appropriate monotonic parametrization that ensures a one-to-one mapping. This task is time-consuming, as it often involves searching for a suitable linear combination of the specific mole number of particular species [116].

A reduced model equation based on physical coordinates is established by analogy with the reduced equation in generalized coordinates (Eqn. (3.35)) by using the chain rule [115]:

$$\boldsymbol{\Psi}_{\xi}\frac{\partial\boldsymbol{\xi}}{\partial t}=\boldsymbol{F}(\boldsymbol{\Psi}(\boldsymbol{\xi}))-\boldsymbol{U}\cdot\boldsymbol{\Psi}_{\xi}\cdot\nabla\boldsymbol{\xi}-\frac{1}{\rho}\nabla\cdot(\boldsymbol{D}\cdot\boldsymbol{\Psi}_{\xi}\cdot\nabla\boldsymbol{\xi}), \tag{4.28}$$

and multiply both sides with one matrix $\boldsymbol{\Psi}_{\boldsymbol{\xi}}^{+}$, then one obtains the reduced model equations in physical coordinates:

$$\frac{\partial\boldsymbol{\xi}}{\partial t}=\boldsymbol{\Psi}_{\boldsymbol{\xi}}^{+}\cdot\boldsymbol{F}(\boldsymbol{\Psi}(\boldsymbol{\xi}))-\boldsymbol{U}\cdot\nabla\boldsymbol{\xi}-\frac{1}{\rho}\boldsymbol{\Psi}_{\boldsymbol{\xi}}^{+}\cdot\nabla\cdot(\boldsymbol{D}\boldsymbol{\Psi}_{\xi}\cdot\nabla\boldsymbol{\xi}). \tag{4.29}$$

The reduced model equation for m_s-dimensional parametrization vector $\boldsymbol{\xi}$ is derived by combining Eqn. (4.29) with the continuity equation:

$$\frac{\partial(\rho\boldsymbol{\xi})}{\partial t}+\nabla\cdot(\rho\boldsymbol{U}\cdot\boldsymbol{\xi})+\boldsymbol{\Psi}_{\boldsymbol{\xi}}^{+}\cdot\nabla\cdot(\boldsymbol{D}\boldsymbol{\Psi}_{\xi}\cdot\nabla\boldsymbol{\xi})=\rho\boldsymbol{\Psi}_{\boldsymbol{\xi}}^{+}\cdot\boldsymbol{F}(\boldsymbol{\Psi}(\boldsymbol{\xi})). \tag{4.30}$$

The matrix $\boldsymbol{\Psi}_{\boldsymbol{\xi}}^{+}$ can be expressed in terms of generalized coordinates, which can be computed by [115]:

$$\begin{aligned}\boldsymbol{\Psi}_{\boldsymbol{\xi}}^{+}&=(\boldsymbol{\Psi}_{\boldsymbol{\xi}}^{T}\boldsymbol{\Psi}_{\xi})^{-1}\boldsymbol{\Psi}_{\boldsymbol{\xi}}^{T}\\&=\boldsymbol{\xi}_{\boldsymbol{\theta}}(\boldsymbol{\xi}_{\boldsymbol{\theta}})^{-1}(\boldsymbol{\Psi}_{\boldsymbol{\xi}}^{T}\boldsymbol{\Psi}_{\xi})^{-1}(\boldsymbol{\xi}_{\boldsymbol{\theta}}^{T})^{-1}\boldsymbol{\xi}_{\boldsymbol{\theta}}^{T}\boldsymbol{\Psi}_{\boldsymbol{\xi}}^{T}\\&=\boldsymbol{\xi}_{\boldsymbol{\theta}}(\boldsymbol{\xi}_{\boldsymbol{\theta}}^{T}\boldsymbol{\Psi}_{\boldsymbol{\xi}}^{T}\boldsymbol{\Psi}_{\xi}\boldsymbol{\xi}_{\boldsymbol{\theta}})^{-1}(\boldsymbol{\Psi}_{\xi}\boldsymbol{\xi}_{\boldsymbol{\theta}})^{T}\\&=\boldsymbol{\xi}_{\boldsymbol{\theta}}[(\boldsymbol{\Psi}_{\xi}\boldsymbol{\xi}_{\boldsymbol{\theta}})^{T}\boldsymbol{\Psi}_{\xi}\boldsymbol{\xi}_{\boldsymbol{\theta}}]^{-1}(\boldsymbol{\Psi}_{\xi}\boldsymbol{\xi}_{\boldsymbol{\theta}})^{T}\\&=\boldsymbol{\xi}_{\boldsymbol{\theta}}(\boldsymbol{\Psi}_{\boldsymbol{\theta}}^{T}\boldsymbol{\Psi}_{\boldsymbol{\theta}})^{-1}\boldsymbol{\Psi}_{\boldsymbol{\theta}}^{T}\\&=\boldsymbol{\xi}_{\boldsymbol{\theta}}\boldsymbol{\Psi}_{\boldsymbol{\theta}}^{+}\\&=\boldsymbol{C}\boldsymbol{\Psi}_{\boldsymbol{\theta}}\boldsymbol{\Psi}_{\boldsymbol{\theta}}^{+}.\end{aligned} \tag{4.31}$$

The term $\boldsymbol{\Psi}_{\boldsymbol{\theta}}\boldsymbol{\Psi}_{\boldsymbol{\theta}}^{+}$ is a projector onto the tangent space of the manifold in generalized coordinates. This means that the matrix $\boldsymbol{\Psi}_{\boldsymbol{\xi}}^{+}$ can project the vector field onto the tangential subspace. The matrix $\boldsymbol{\Psi}_{\boldsymbol{\xi}}$ can be defined as:

$$\begin{aligned}\boldsymbol{\Psi}_{\boldsymbol{\xi}}&=\boldsymbol{\Psi}_{\boldsymbol{\theta}}\boldsymbol{\theta}_{\boldsymbol{\xi}}\\&=\boldsymbol{\Psi}_{\boldsymbol{\theta}}(\boldsymbol{C}\boldsymbol{\Psi}_{\boldsymbol{\theta}})^{-1}.\end{aligned} \tag{4.32}$$

Therefore, the REDIM table based on generalized coordinates can be further post-processed, for example, the terms $\boldsymbol{D}\boldsymbol{\Psi}_{\boldsymbol{\xi}}=\boldsymbol{D}\boldsymbol{\Psi}_{\boldsymbol{\theta}}(\boldsymbol{C}\boldsymbol{\Psi}_{\boldsymbol{\theta}})^{-1}$, $\boldsymbol{\Psi}_{\boldsymbol{\xi}}^{+}\boldsymbol{F}=\boldsymbol{C}\boldsymbol{\Psi}_{\boldsymbol{\theta}}\boldsymbol{\Psi}_{\boldsymbol{\theta}}^{+}\boldsymbol{F}$, to get the REDIM table based on physical coordinates. Figure 4.6 shows the grid indices of a 2D REDIM table projected on (ξ_1,ξ_2) space, in which $\xi_1 = \phi_{N_2}$ and $\xi_2 = \phi_{CO_2} + 0.5\phi_{CO}$. The implementation scheme for the REDIM in physical coordinates is same as the procedure in generalized coordinates. It simply entails replacing Eqn. (4.24) with Eqn. (4.30) in the reduced model equation that needs to be solved, as explained in the above section.

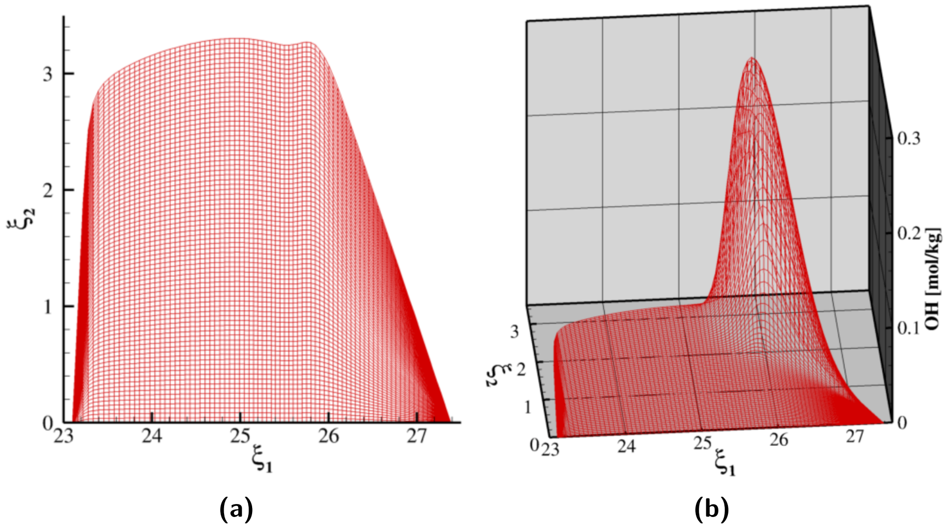

(a) **(b)**

Figure 4.6: Grid indices of a 2D REDIM table based on the physical coordinates, 2D projection of manifold in the physical coordinates ξ (a), 3D projection of OH profile (b).

4.3.3 Relative CPU time

The primary reason for utilizing reduced chemistry in numerical combustion is to decrease computational effort. Consequently, it is necessary to compare the computational costs of the detailed mechanism and the REDIM method. To facilitate this comparison, a relative CPU time method between detailed simulation and REDIM has been defined [31]:

$$\text{Relative CPU time of REDIM} = \frac{\text{CPU time with REDIM}}{\text{CPU time with detailed mechanism}}, \tag{4.33}$$

where the CPU time denotes the computing time based on the same time step and mesh size with the detailed chemical kinetics and the REDIM reduced chemistry in single core. As introduced before, the REDIM reduced chemistry only solves the $(3+m_s)$ equations $(m_s \ll n_s)$ in the calculation, which not only can significantly reduce the computational cost, but can efficiently decrease the stiffness of governing equations. Moreover, other thermo-chemical quantities (e.g. temperature, species mass fractions) can be retrieved by the linear interpolation from a REDIM look-up table, which can avoid to solve highly non-linear chemical source terms.

4.3.4 Comparison of results based on generalized and physical coordinates

To verify the performance of REDIMFoam solver and to compare the results computed by the REDIM method in generalized and physical coordinates, an adiabatic 1D methane/air free flame is calculated in this section. The equivalence ratio (Φ) of fuel mixture is 1. A unity Lewis number is assumed. The boundary conditions used in the free flame are listed in table 4.2, in which zero gradient denotes the Neumann boundary condition [117], and the others are Dirichlet boundary conditions [117]. A 1-dimensional REDIM (i.e. $m_s = 1$, ϕ_{CO_2} is selected here) is generated and provided to the REDIMFoam solver.

Table 4.2: Boundary conditions of 1D free flame.

	T	p	$\boldsymbol{U}$	species mass fractions
Left boundary	300 K	zero gradient	0.5 m/s	$\Phi = 1$
Right boundary	zero gradient	1 bar	zero gradient	zero gradient

The computational results obtained with the detailed mechanism (SanDiego-2014 mechanism [118] used in EBIdnsFoam and INSFLA) and the corresponding REDIM reduced chemistry (used in REDIMFoam) are compared. In figure 4.7, some major and minor species are plotted over the spatial coordinate. A good agreement can be observed between the results obtained from EBIdnsFoam and INSFLA code with the same mechanism, which further validates the performance of EBIdnsFoam in the 1D free flame. It also can be seen that a better description of these species profiles can be obtained with the REDIM method comparing with the detailed solutions (results in EBIdnsFoam and INSFLA code), even for minor species. The computed results with 1D REDIM in generalized coordinate are much lightly different from these results in physical coordinate. Moreover, Strassacker *et al.* calculated a head-on quenching flame with the 2D REDIM in generalized and physical coordinates, and there is also nearly no discrepancy between the results with generalized and physical coordinates [115].

The CPU time of detailed mechanism in the EBIdnsFoam solver is 4.49 s, however, the CPU time of REDIMFoam in generalized and physical coordinates are 0.51 s and 0.55 s, respectively. The relative CPU time of REDIM in generalized and physical coordinates is approximately 11 % and 12 % of the detailed mechanism. Therefore the economy of computational effort is considerable.

The calculated results based on generalized coordinate have excellent agreement with their corresponding results computed by physical coordinate, and the CPU time is almost same. The generalized coordinate is anywhere perfectly accommodated to the reaction progress on the simplified manifold and ensures uniqueness. Furthermore, the generalized coordinate can also improve the efficiency and the robustness of interpolation calculation during the implementation of REDIM, since the structure of the grid is locally orthogonal and equidistant everywhere [72]. Therefore, we will use the REDIMFoam solver based on generalized coordinate for the following calculations in the thesis.

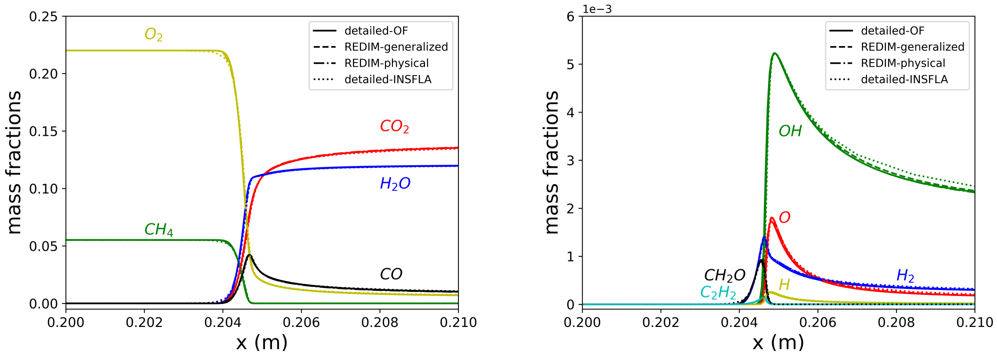

(a) **(b)**

Figure 4.7: Comparison of results for major (a) and minor (b) species computed with the SanDiego-2014 mechanism and the corresponding REDIM reduced chemistry in generalized and physical coordinates, solid line: EBIdnsFoam with SanDiego-2014, dashed line: REDIM in generalized coordinate, dashed dotted line: REDIM in physical coordinate, dotted line: INSFLA with SanDiego-2014.

5 Validation of 2D counterflow flames

5.1 Problem definition

In order to verify the REDIM method, some results computed by detailed and reduced mechanisms according to the generalized coordinate are compared in this chapter. The flame studied is a two-dimensional axisymmetric laminar counterflow diffusion flame. A stream of methane mixed with air (25 % CH_4 + 75 % air in volume percent, equivalence ratio $\Phi = 3.17$) is injected from the left boundary while a stream of air (21 % O_2 + 79 % N_2 in volume percent) is injected from the right boundary. The mixture composition is the same as the composition used in the Sandia flame [119], and the simulation of 1D counterflow diffusion flames based on the fuel mixture has been investigated in the steady and unsteady regimes [31]. In this chapter, we mainly study the properties of 2D counterflow diffusion flames with detailed and reduced mechanisms. The gravity is neglected in the calculations. A brief schematic of the burner configuration is presented in Figure 5.1, which is similar to the burner geometry in Refs. [120, 121]. The geometry has been simplified to make it easier to simulate in this work, namely not considering the nozzle rim thickness and the nozzle protrusion length.

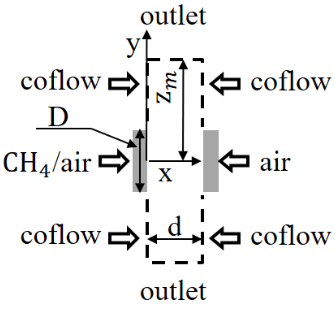

Figure 5.1: Schematic of the burner configuration and the axisymmetric computational domain.

5.2 Numerical set-up

5.2.1 computational domain and mesh size

The computational domain is axisymmetric (2-dimensional), and diameters of the nozzles (D) for the fuel flow and the oxidizer flow are both 2 cm. The distance d between the two nozzles is 2 cm as well, in addition, the computational height is $z_m = 4$ cm (measured from the centerline of the nozzle). In the present work, three mesh sizes (mesh 1, mesh 2 and mesh 3 listed below) are used to compute the 2D axisymmetric laminar diffusion flames with the detailed mechanism and the corresponding REDIM method, respectively, in order to investigate the mesh dependence. In the computational domain between the two nozzles (2 cm × 2 cm), the mesh is equidistantly spaced along both x and y directions (see Figure 5.1), but out of this domain, the mesh size increases proportionally in the y direction.

- Mesh 1 (coarse):
  $\Delta x = 0.1$ mm for $0 \leq x \leq 2$ cm, $\Delta y = 0.25$ mm for $0 \leq y \leq 1$ cm, and increasing spacing starting from $\Delta y = 0.26$ mm for $1 < y \leq 4$ cm.
- Mesh 2 (fine):
  $\Delta x = 0.05$ mm for $0 \leq x \leq 2$ cm, $\Delta y = 0.125$ mm for $0 \leq y \leq 1$ cm, and increasing spacing starting from $\Delta y = 0.13$ mm for $1 < y \leq 4$ cm.
- Mesh 3 (very fine):
  $\Delta x = 0.025$ mm for $0 \leq x \leq 2$ cm, $\Delta y = 0.125$ mm for $0 \leq y \leq 1$ cm, and increasing spacing starting from $\Delta y = 0.13$ mm for $1 < y \leq 4$ cm.

5.2.2 Boundary conditions and mechanisms

The detailed boundary conditions considered for the 2D counterflow flames are listed in table 5.1. The inlet velocities are equal in magnitude and opposite in direction for both nozzle streams, which are set to different values (details will be discussed in the following sections). Air flows from the concentric pipe (coflow) with an axial velocity of 0.01 m/s [120]. The outlet is treated as an outflow boundary condition.

The detailed mechanisms GRI 3.0 [48] and SanDiego-2014 [118] are used in the simulations with EBIdnsFoam solver, which consist of 53 components with 325 elementary reactions and 48 components with 247 elementary reactions, respectively. The assumption of unity Lewis number is used in this work, which has been shown to be a reasonable simplification in these kind of flame

Table 5.1: Boundary conditions of 2D counterflow flame.

	T	p	$\boldsymbol{U}$	species mass fractions
Nozzles	293 K	zero gradient	fixed	25 % CH_4 + 75 % air
Coflow	293 K	zero gradient	0.01 m/s	air
Outlet	zero gradient	1 bar	zero gradient	zero gradient

configurations [15, 122, 123]. Furthermore, the focus of this chapter is not an analysis of the transport model, but a comparison between detailed and reduced mechanisms.

The 2D REDIM reduced chemistry ($m_s = 2$) is applied to calculate the 2D counterflow flames. The generation process of REDIM table is introduced in section 3.3.7. The boundary conditions and initial conditions used for the generation of REDIM are taken from a collection of 1D counterflow flames with different strain rates ($a = 80, 100, 120, 140, 160, 180, 200, 300\ s^{-1}$ and mixing line) computed with the GRI3.0 and SanDiego-2014 mechanisms, in which the flamelet with low strain rate of 80 s^{-1} is the upper boundary and the mixing line represents the lower boundary of the application range of REDIM. The assumption of unity Lewis number is also used in the REDIM method.

5.3 Mesh dependence

The computational results with the detailed mechanism (GRI3.0) and the corresponding REDIM method are presented in the section in order to investigate the influence of different mesh resolutions on flame structure. The detailed solutions are computed by the EBIdnsFoam solver and the reduced results are calculated by the REDIMFoam solver based on the generalized coordinate. The inlet velocity of the counterflow nozzles is set to 1.0 m/s. $\boldsymbol{\phi} = (\phi_{N_2}, \phi_{CO_2})^T$ is selected as the progress variables in this section. Figure 5.2 shows the structures of two dimensional axisymmetric laminar diffusion flames computed with the GRI3.0 mechanism, in which green rectangles just denote the location of nozzles, not belonging to the computational domain. Figures 5.3a and 5.3b display contours of temperature and profiles of selected species mass fractions along the centerline of the computational domain on three mesh sizes, respectively. As can be observed, the peak temperatures (black line: 2006 K on mesh 1; red line: 2016 K on mesh 2; blue line: 2019 K on mesh 3) computed by the three mesh sizes have almost the same values, and the error is very small. The minor species profiles (OH and O mass fractions) computed by mesh 1 have difference to finer mesh (mesh 2 and mesh

3), while the results computed by mesh 2 and mesh 3 have good agreement in Figure 5.3b, which means that the effect of mesh size in the calculations is negligible on mesh 2 and mesh 3.

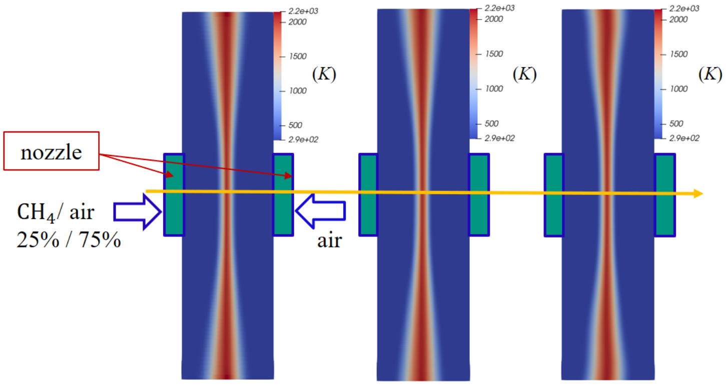

Figure 5.2: Temperature profiles computed with the detailed chemistry GRI3.0 on three mesh sizes, left figure: mesh 1; middle figure: mesh 2; right figure: mesh 3; the yellow line marks the centerline along the computational domain.

In Figure 5.4a, it is shown that the flame thickness computed by mesh 1 is a bit larger than the results on mesh 2 and mesh 3, while the error is less than 2 %. Although the peak temperatures on mesh 1 (black line: 1992 K) is slightly lower than the values (red line: 2015 K; blue line: 2017 K) on mesh 2 and mesh 3, the error is very small as well. As can be observed, the minor species profiles (OH, O and H_2 mass fractions) computed with the REDIM reduced chemistry on mesh 1 have difference to finer mesh (mesh 2 and mesh 3), while the results on mesh 2 and mesh 3 have good agreement in Figure 5.4b, which means that the effect of mesh size in the calculations is negligible on mesh 2 and mesh 3. Analyzing the above results, we think the accuracy of mesh 2 is sufficient to capture the flame structure for the detailed and reduced mechanisms, therefore, we will use this mesh size for the following analysis.

The CPU time of detailed mechanism (GRI3.0) in the EBIdnsFoam solver is 156.99 s, however, the CPU time of REDIMFoam with the corresponding REDIM reduced chemistry in generalized coordinate is 15.28 s, based on the same time step and mesh size (mesh 2). The relative CPU time of REDIM is only approximately 10 % of the detailed mechanism, which means that the REDIM method can significantly reduce the computational effort.

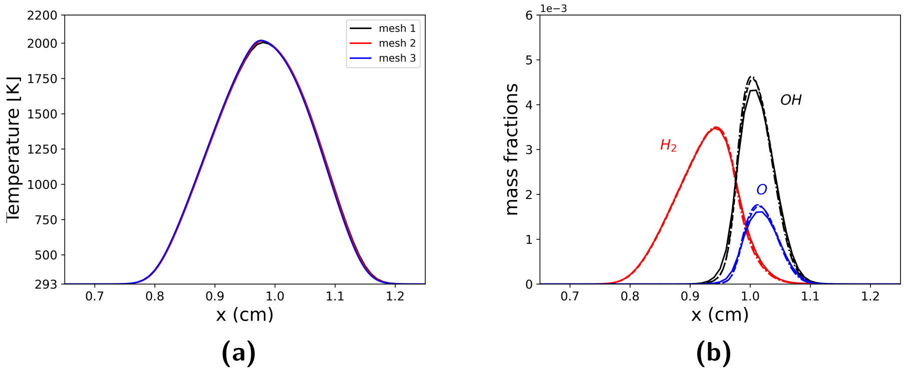

(a) **(b)**

Figure 5.3: Comparison of results for temperature (a) and minor species (b) computed with the detailed chemistry GRI3.0 along the centerline of the 2D counterflow flame on three mesh sizes, solid line: mesh 1, dashed line: mesh 2, dashed dotted line: mesh 3.

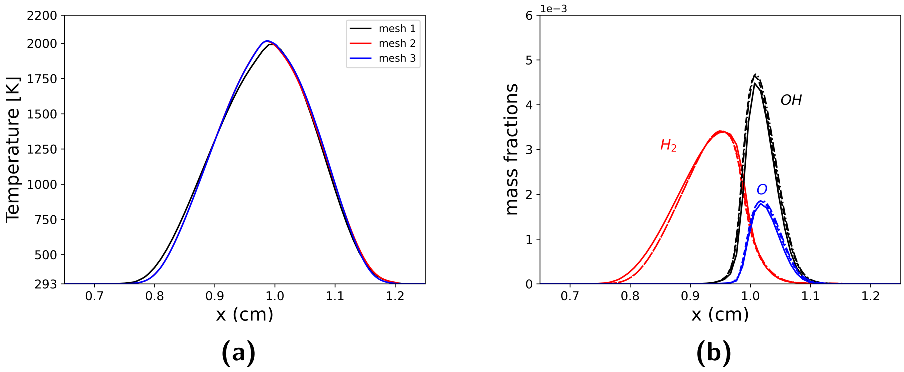

(a) **(b)**

Figure 5.4: Comparison of results for temperature (a) and minor species (b) computed with the REDIM method along the centerline of the 2D counterflow flame on three mesh sizes, solid line: mesh 1, dashed line: mesh 2, dashed dotted line: mesh 3.

5.4 Influence of the choice of progress variable

In this section, two different linear combinations of parametrization ($\boldsymbol{\phi} = (\phi_{\mathrm{N_2}}, \phi_{\mathrm{CO_2}})^T$ and $(\phi_{\mathrm{N_2}}, \phi_{\mathrm{CO_2}} + 0.5\phi_{\mathrm{CO}})^T$) have been chosen to verify the independence of the REDIM reduced chemistry with respect to the progress variable. The inlet velocity of the nozzles is 1.0 m/s. The GRI3.0 mechanism is implemented in the section. Figure 5.5 shows the temperature profiles of the 2D counterflow flames, in which the left part of each figure in Figure 5.5 shows the results obtained by the EBIdnsFoam using detailed chemistry (GRI

3.0), while the right part shows the results computed by the REDIMFoam with $(\phi_{\mathrm{N_2}}, \phi_{\mathrm{CO_2}})$ progress variable.

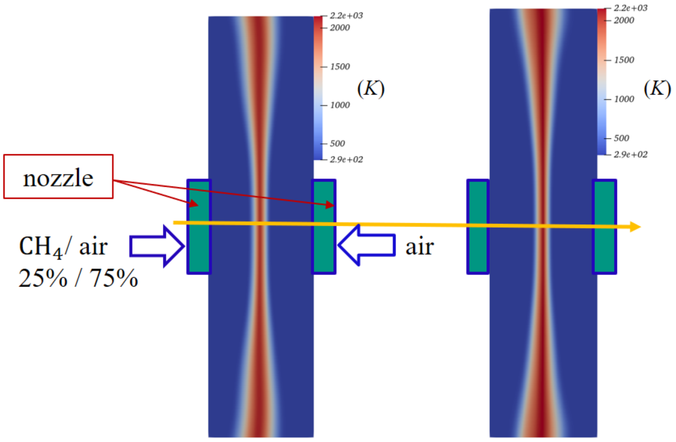

Figure 5.5: Temperature profiles on mesh 2, left figure: detailed mechanism (GRI3.0); right figure: REDIM reduced mechanism; the yellow line marks the centerline along the computational domain.

As can be seen in Figure 5.6, the results of the REDIM reduced model obtained with different progress variables $(\phi_{\mathrm{N_2}}, \phi_{\mathrm{CO_2}})$ and $(\phi_{\mathrm{N_2}}, \phi_{\mathrm{CO_2}}+0.5\phi_{\mathrm{CO}})$, both are almost same as the results of the detailed mechanism, regardless of temperature or H_2O mass fraction, and even for the minor species such as OH mass fraction. Although the mass fraction of O computed by the REDIM method is slightly different to the detailed solution, the profiles computed by the REDIMFoam with the two different progress variables are almost same. The peak temperature computed by the GRI3.0 mechanism is 2016 K, while the values obtained with the progress variables $(\phi_{\mathrm{N_2}}, \phi_{\mathrm{CO_2}})$ and $(\phi_{\mathrm{N_2}}, \phi_{\mathrm{CO_2}} + 0.5\phi_{\mathrm{CO}})$ are 2015 K and 2016 K respectively in Figure 5.6a. It is proved that the generation of the REDIM reduced chemistry is independent on the choice of the progress variable, in which the only principle of the choice is to guarantee a one-to-one mapping of REDIM, as discussed in section 3.3.3.

5.5 Influence of the choice of reaction mechanism

The computational results obtained with the detailed mechanisms (GRI 3.0 and SanDiego-2014) and the REDIM reduced chemistry are compared in the section on mesh 2. Two REDIM tables are generated by two detailed

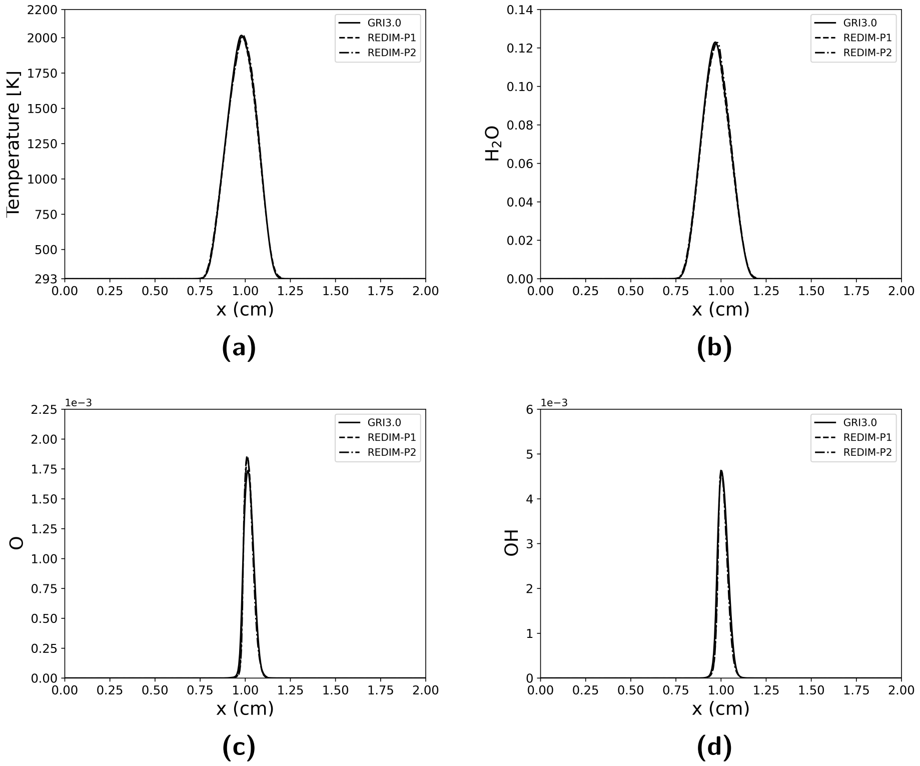

Figure 5.6: Comparison of results for temperature (a) and mass fractions of H_2O (b), O (c) and OH (d) along the centerline of the 2D counterflow flame, solid line: GRI3.0, dashed line (REDIM-P1): $(\phi_{N_2}, \phi_{CO_2})$, dashed dotted line (REDIM-P2): $(\phi_{N_2}, \phi_{CO_2} + 0.5\phi_{CO})$.

mechanisms, the GRI 3.0 mechanism and the SanDiego-2014 mechanism. The inlet velocity of two streams is 1.0 m/s. $\boldsymbol{\phi} = (\phi_{N_2}, \phi_{CO_2})$ is selected as the progress variable in this section.

The profiles of temperature and selected species mass fractions over N_2 mass fraction for two detailed mechanisms (GRI3.0 and SanDiego-2014) as well as their corresponding REDIMs (dashed line) are shown in Figure 5.7. The temperature and mass fraction of CO_2 over N_2 mass fraction is quantitatively very similar for the two mechanisms. The peak temperature (2015 K in Figure 5.7a) obtained from the REDIM reduced mechanism is almost same as the peak temperature (2016 K) computed by the detailed chemistry (GRI3.0 mechanism), moreover, the peak temperature (2031 K) calculated by the SanDiego-2014 mechanism is also almost same as 2032 K in the REDIM reduced chemistry. The errors introduced by REDIM are less than 0.1 %.

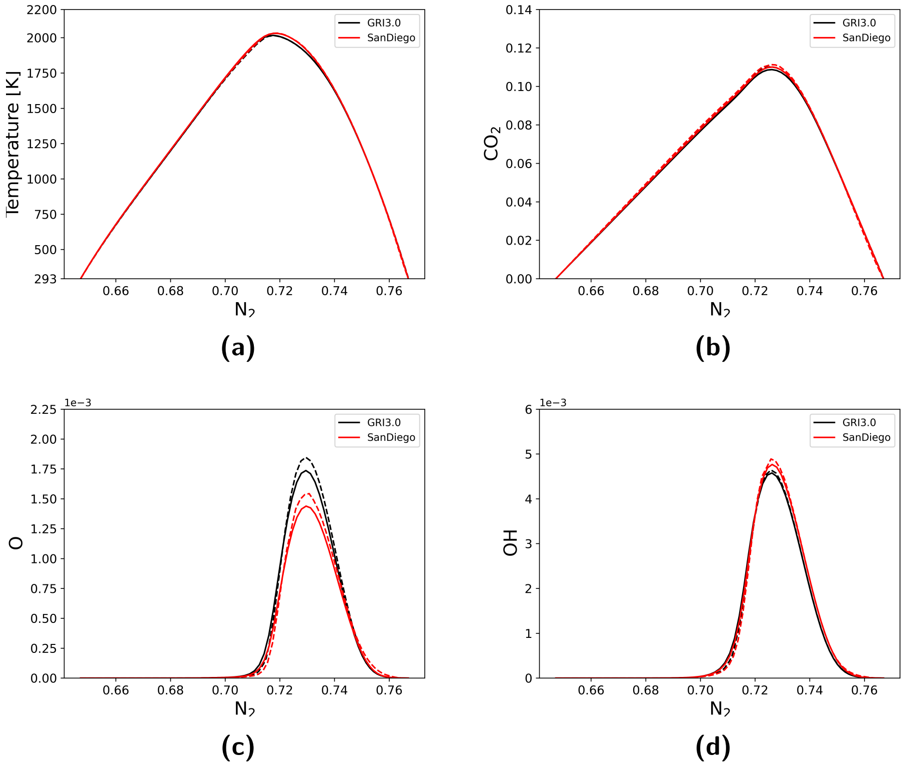

Figure 5.7: Comparison of results for temperature (a) and mass fractions of CO_2 (b), O (c) and OH (d) over mass fraction N_2 with detailed (solid line) and reduced (dashed line) mechanisms along the centerline of the 2D counterflow flame.

Maximum of CO_2 mass fractions shows negligible differences between the detailed mechanisms and the REDIM reduced model as well. This means that the REDIM method can reproduce the structure of the 2D counterflow flame very well. In contrast, the profiles of minor species O and OH over N_2 mass fraction are different for the two mechanisms. It is shown that the differences between REDIM and detailed mechanisms for the same mechanism are much smaller than the ones between the different mechanisms.

Consequently, from analyzing the above results, we can make the conclusion that the computation with REDIM reduced chemistry has excellent agreement with their corresponding results computed by the different detailed mechanism.

5.6 Influence of the inlet velocity

5.6.1 Model performance under steady conditions

This section investigates the behavior of REDIM for various inlet velocities of the nozzle which are commonly used to determine global strain rates a_g in 2D counterflow flames. The definition of the global strain rate is as follows [120, 121, 124]:

$$a_g = \frac{2U_r U_F}{d}\left(1 + \frac{\sqrt{\rho_F}}{U_r\sqrt{\rho_O}}\right), \tag{5.1}$$

where the velocity ratio $U_r = U_O/U_F$, U_O and U_F denote the inlet velocities of the air and fuel streams, d is the distance between two nozzles in Figure 5.1, and ρ_F and ρ_O are the density of fuel mixture and air, respectively. The values of the inlet velocity for fuel and air streams at both nozzles are same in this work, therefore $U_r = 1$, $U_F = U$.

The REDIM reduced chemistry is based on the GRI3.0 mechanism. $\boldsymbol{\phi} = (\phi_{N_2}, \phi_{CO_2})$ is selected as the progress variable in this section. Figure 5.8a shows the temperature profiles calculated by the GRI3.0 mechanism and the REDIM reduced chemistry under three different inlet velocities ($U =$ 0.5, 1.0 and 1.5 m/s). Comparing the temperature profiles of the detailed mechanism and the REDIM method, it is found that REDIM can reproduce the flame structure very well with the change of the inlet velocity. The peak temperatures of the detailed mechanism decrease with the increase of the inlet velocity in table 5.2, and the peak temperatures computed by the REDIM method have the same tendency with the change of the inlet velocity. Additionally, the increased strain rate decreases the residence time of the flame, therefore the flame has less time to reach chemical equilibrium.

Figure 5.8b shows the profiles of mass fractions for major species (H_2O). Analyzing the computational results, we found that results obtained by the REDIM method have a better agreement with that obtained by detailed mechanism with the change of inlet velocity. The maxima of H_2O computed by the REDIM method are approximately equal to the values computed by the detailed mechanism. As for the minor species, OH and H_2, the results computed by the REDIM method still have a good agreement with the results from the detailed mechanism in Figures 5.8c and 5.8d.

The maximum of temperature and mass fractions of major and minor species along the centerline of the 2D counterflow flame computed by the detailed and reduced mechanisms over strain rates (that is, different inlet velocities) from 97 s^{-1} to 972 s^{-1} are compared in Figure 5.9. We can see that the results computed by the REDIM method agree very well with detailed

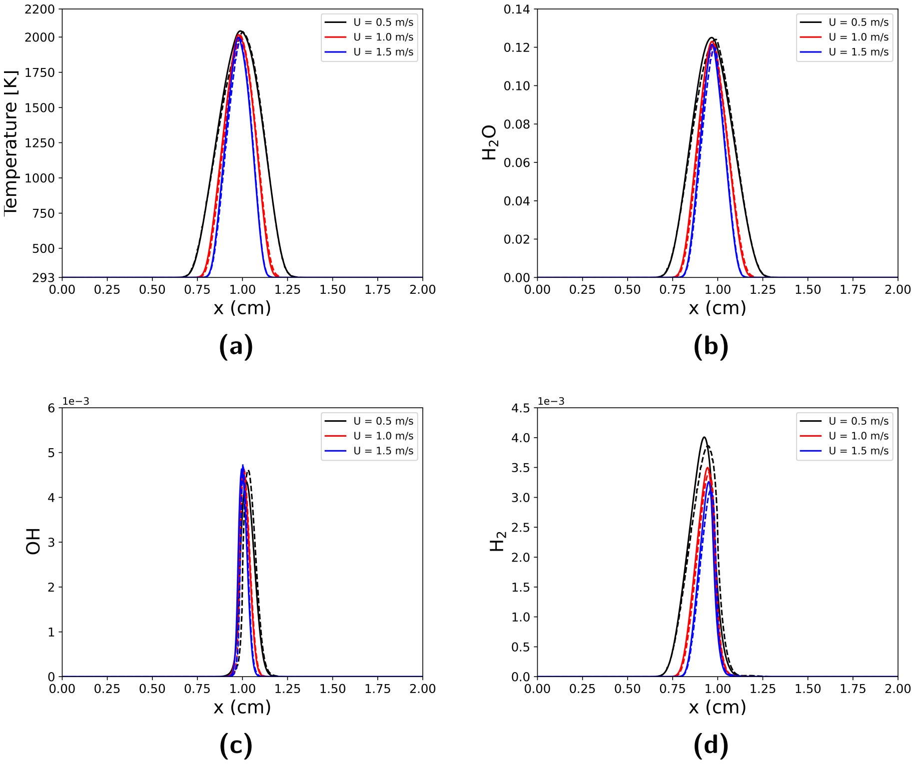

Figure 5.8: Comparison of results for temperature (a) and mass fractions of H_2O (b), OH (c) and H_2 (d) along the centerline of the 2D counterflow flame under three different inlet velocities (U = 0.5, 1.0 and 1.5 m/s), solid line: GRI3.0, dashed line: REDIM reduced mechanism.

Table 5.2: Peak temperatures.

inlet velocity	global strain rate	GRI3.0	REDIM
U = 0.5 m/s	$a_g = 97\ s^{-1}$	2043 K	2038 K
U = 1.0 m/s	$a_g = 194\ s^{-1}$	2016 K	2015 K
U = 1.5 m/s	$a_g = 291\ s^{-1}$	1997 K	1987 K

mechanism in the range of small global strain rates (97 - 600 s^{-1}). Small differences can be observed in the maximum of minor species, e.g. OH and H_2 in the larger global strain rates ($> 600\ s^{-1}$), while the values of temperature, H_2O mass fractions in the REDIM method have good agreement with results of the GRI3.0 in the whole strain rates.

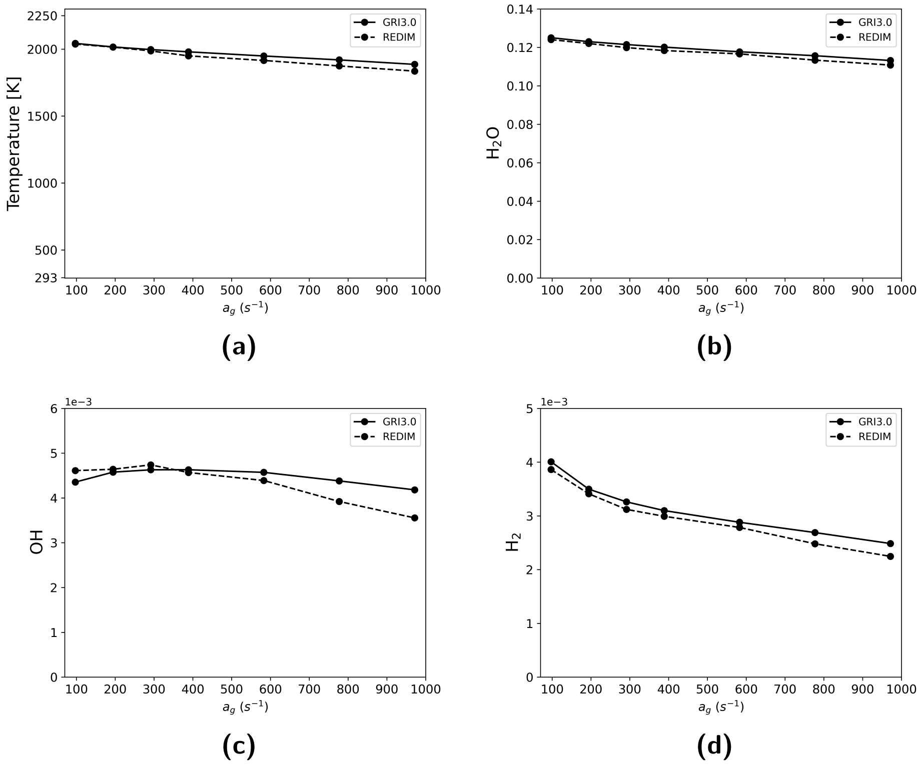

(a) (b)

(c) (d)

Figure 5.9: Comparison of results for maxima of temperature (a) and mass fractions of H_2O (b), OH (c) and H_2 (d) along the centerline of the 2D counterflow flame over global strain rates, solid line: GRI3.0, dashed line: REDIM reduced mechanism.

5.6.2 Model performance under extinction conditions

In the preceding sections, our focus was solely on validating REDIM's performance under steady state. By increasing the global strain rate beyond the quenching limit (1457 s^{-1}), whether the REDIM method can provide an accurate description of the flame response. This scenario offers an intriguing test case to assess REDIM's performance in dealing with extinction conditions.

Hence, we employ the time-varying step function in OpenFOAM to elevate the global strain rate from 97 s^{-1} to exceeding the quenching limit of 1550 s^{-1}.

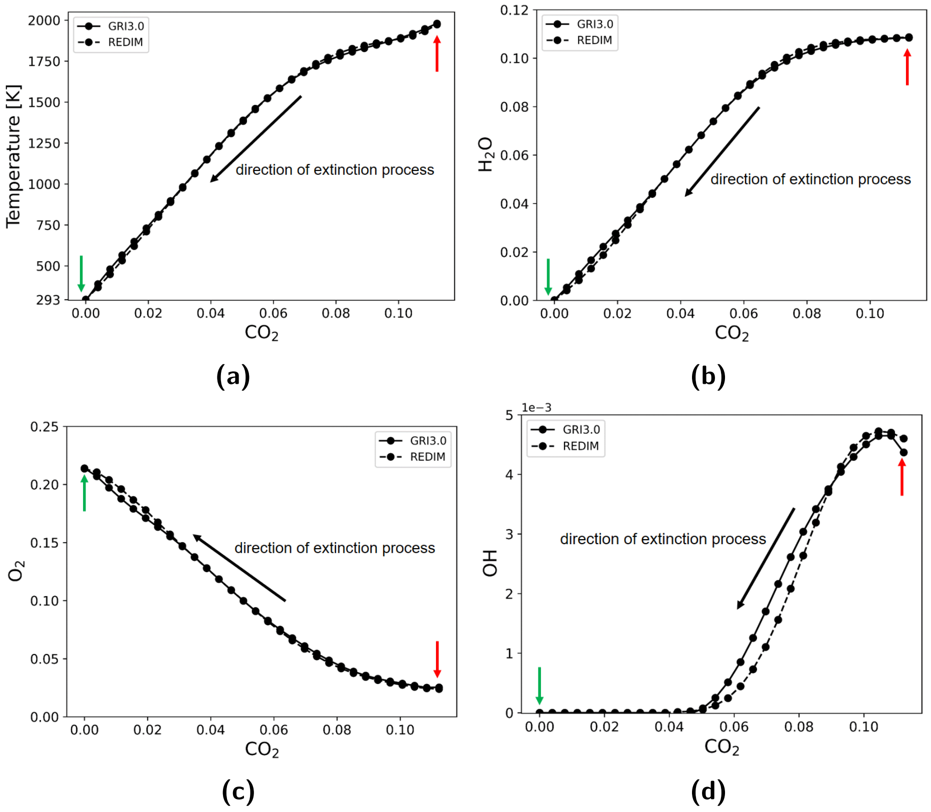

(a) (b) (c) (d)

Figure 5.10: Comparison of the extinction process in the 2D counterflow flame, solid line: GRI3.0, dashed line: REDIM reduced mechanism.

Figure 5.10 illustrates the state spaces of temperature and mass fractions of H_2O, O_2 and OH over mass fraction of CO_2, as calculated by the GRI3.0 mechanism (solid line) and the REDIM method (dashed line) at the point of maximum CO_2 mass fraction during the extinction process. The points indicated by red arrows denote the initial state and the points indicated by green arrows are extinguished state. The black arrows show the direction of extinction process in the figures. Regarding the reduced solutions, it is evident that, by definition, their movement is constrained within the REDIM slow manifolds. It can be observed that the REDIM reduced chemistry can describe the behaviour of extinction in the flames very well, even though we do not provide the extinction flamelets in the generation of REDIM. The results of temperature and mass fractions of H_2O and O_2 with REDIM reduced chemistry almost overlap with the detailed solution. This implies that these thermokinetic properties exhibit changes in close proximity to REDIM during the extinction process. Although there is a minor discrepancy for the OH mass fraction between detailed and reduced solutions during the extinction process in Figure 5.10d, the REDIM method still clearly show the evolution of the extinction process with acceptable accuracy in the 2D counterflow flames.

Overall, the REDIM method can reproduce the flame structures of steady and quenching regimes in the 2D counterflow flames very well. Due to the small errors between the detailed mechanism and the REDIM reduced chemistry, we think the results are acceptable and demonstrate that REDIM can be used in the applications at extreme conditions with very good accuracy, even with two-dimensional manifolds (2D REDIM).

6 Validation of 2D jet flames

6.1 Problem definition

In this chapter, we will examine a two-dimensional axisymmetric laminar jet diffusion flame, with a focus on comparing the detailed mechanism with the REDIM reduced chemistry. The study will exclude the influence of gravity. The flame configuration is used in most practical combustion devices, e.g. gas turbines and commercial burners. The jet diffusion flame is very important for investigating the interaction of complex transport process with detailed mechanism, because the results of the investigation can be used to model turbulent combustion, probe flow-thermochemistry interaction and understand how pollutants are generated. In the configuration studied in this section, a cylindrical stream of fuel mixture is injected into a coflowing oxidizer stream [58, 125, 126]. The tubes through which the fuel mixture and the oxidizer flow are concentric with radii R_I and R_O, respectively. The wall thickness of the two tubes is assumed to be zero [58]. The two gases come into contact at the outlets of the inner and outer tubes, and produce an unconfined coflowing flame (see Figure 6.1).

6.2 Numerical set-up of 2D jet flames

6.2.1 Computational domain and reaction zone

Given that the flame is of the Bunsen type, its flame structure exhibits symmetry around the axis of the inner tube. Therefore, for axisymmetric problems, a 2-dimensional computational domain is sufficient (see Figure 6.1b), which can reduce the computational effort.

The fuel mixture flows from an inner tube (i.e. main jet, $R_I = 0.2$ cm) and the oxidizer is injected from the annular outer tube ($R_O = 2.5$ cm). A computational height $L = 12$ cm has been considered. The green dashed line in Figure 6.1b shows the computational domain. In the literature [43, 107, 113, 127, 128], such flames usually exist the liftoff phenomenon. In order to better resolve the flame structure, it is necessary to use local mesh refinement technology [106, 107, 113, 129]. Therefore, we defined a reaction zone with a locally refined, uniform mesh in the computational domain.

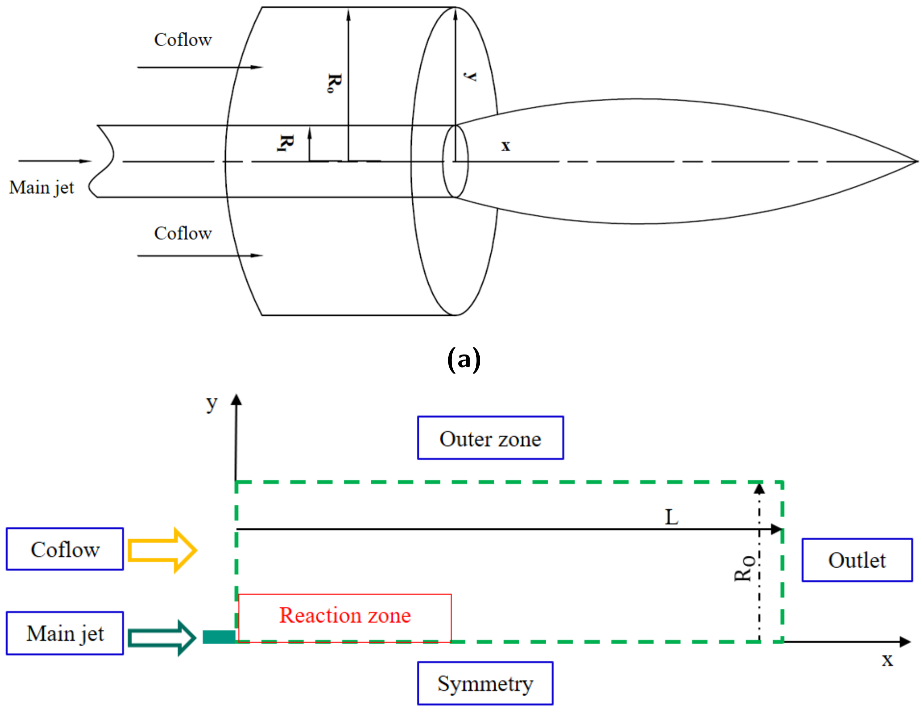

(a)

(b)

Figure 6.1: Schematic illustration of 2D jetflow flame configuration (a) and the computational domain (b).

First, the coarse initial mesh (consisting of 16000 grids) is used to calculate the initial solution. The mesh size increases proportionally in the x and y directions. The smallest mesh appears at the patch of the main jet and has dimensions $\Delta x = 0.33$ mm and $\Delta y = 0.2$ mm. The largest mesh appears at the patch of outlet and has dimensions $\Delta x = 0.99$ mm and $\Delta y = 0.46$ mm. Then the initial mesh is used to find a first approximation for the steady solution of the 2D jet flame with detailed and reduced mechanisms. Finally, the position of the reaction zone is determined in terms of the profile of OH in the steady solution (see Figure 6.2). The maximum value of OH on the right and top sides of the reaction zone should not exceed one tenth of the maximum value of OH within the reaction zone.

The mesh size is equidistantly spaced in the reaction zone, which has dimension $\Delta x = 0.1$ mm and $\Delta y = 0.05$ mm, according to the results of section 5.3 and the detailed numerical simulation in Ref. [107, 130]. Out of this reaction domain, the mesh size still increases proportionally in the x and y directions. Due to the different length and width of the reaction region, the total number of grids in each computational example is different.

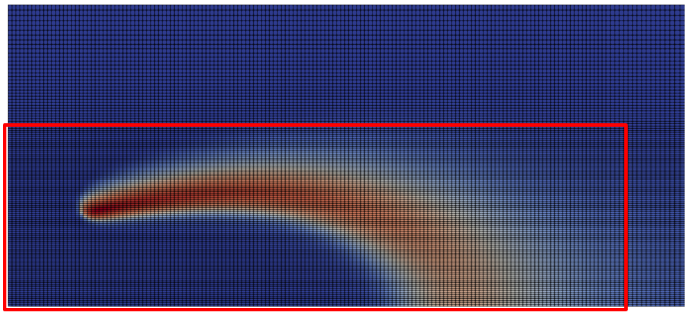

Figure 6.2: Reaction zone (red wireframe) determined by profile of OH in steady state.

6.2.2 Boundary conditions and mechanism used in 2D jet flames

The detailed boundary conditions considered for the 2D jet flames are listed in table 6.1. The inlet velocities of main jet and coflow are set to same or different values (details will be discussed in the following sections). The fuel mixture in the main jet consists of 25 % methane and 75 % air in volume percent. Air flows from the concentric pipe (Coflow) with an fixed axial velocity. The outlet is treated as an outflow boundary condition. A special symmetry boundary condition ("symmetry" in Fig. 6.1) is applied to treat the simulation setup as an axisymmetric case (2D in cylindrical coordinates) [63].

Table 6.1: Boundary conditions of 2D jet flames.

	T	p	$\boldsymbol{U}$	species mass fractions
Main jet	293 K	zero gradient	fixed	25 % CH_4 + 75 % air
Coflow	293 K	zero gradient	fixed	air
Outlet	zero gradient	1 bar	zero gradient	zero gradient
Outer zone	zero gradient	1 bar	zero gradient	zero gradient

The detailed solution is computed by EBIdnsFoam solver with the GRI 3.0 mechanism. The assumption of unity Lewis number is used in this chapter. The 2D REDIM reduced chemistry ($m_s = 2$) is applied to calculate the 2D jet flames to receive the reduced solution. $\boldsymbol{\phi} = (\phi_{\mathrm{N_2}}, \phi_{\mathrm{CO_2}} + 0.5\phi_{\mathrm{CO}})$ is selected as the progress variable in this section. The generation method of REDIM tables is same as that used in chapter 5. The boundary conditions and initial conditions used for the generation of REDIM are taken from a collection of 1D counterflow flames with different strain rates ($a = 5, 60, 120, 200, 400, 600\ s^{-1}$ and mixing line) computed with the GRI3.0 mechanism, in which the flamelet with low strain rate of 5 s^{-1} is the upper boundary and the mixing line represents the lower boundary of the application range of REDIM. It can be seen that the upper boundary and initial conditions used here to generate REDIM are different from the REDIM used in the 2D counterflow flames. This is because the choice of the boundary of initial manifold is determined by the specific physical problem being studied and the REDIM has to cover all the state space of the considered reaction system, while except the boundary, the choice of other initial flamelets is arbitrary (details see section 3.3). The assumption of unity Lewis number is also used in the REDIM method.

6.3 Flame structures of steady state

We will introduce the results of steady state computed by detailed and reduced mechanisms under different inlet velocities (U = 0.35, 0.5 and 0.65 m/s) in this section. The inlet velocity has the same value at the main jet and coflow, and the distribution is assumed to be uniform.

6.3.1 Flame overview

Figures 6.3, 6.4 and 6.5 display contours of temperatures and mass fractions of selected species for inlet velocities of the main jet and coflow U = 0.35, 0.5 and 0.65 m/s, respectively. The left half of each plot shows results computed by the GRI3.0 mechanism, while the right half of each plot shows results obtained with the corresponding REDIM reduced chemistry. A single color scale, ranging from blue (minimum values) to red (maximum values), has been used in both halves of each plot. The ranges of maximum and minimum for the GRI3.0 and the REDIM method in the datasets are presented in the first and second line at the top of each plot, respectively.

The temperature of flames displays a typically wishbone-shaped region and the liftoff phenomenon, as observed in Refs. [106, 113, 131, 132]. It can be seen that the REDIM method can successfully describe the liftoff phenomenon for three different inlet velocities and has a very good agreement for temperature and mass fractions of selected species, when compared with the results computed by detailed mechanism. The flame structures of reduced and detailed mechanisms are almost same. Small discrepancy is mainly caused by the vertical translation or scaling due to small differences in liftoff height and flame length [107]. As can be seen in figures 6.3, 6.4 and 6.5, with the increase of the inlet velocity, the flame liftoff phenomenon is more obvious, and the liftoff height and flame length become larger. Both the detailed mechanism and the REDIM method can well describe this process.

The concentration of fuel CH_4 has the highest value at the location near of the nozzle surface, then reacts quickly with OH, O and H radicals. OH exists in relatively thin area, mainly within the high-temperature zone, and the highest concentrations of OH are found away from the centerline (where $y = 0$). O_2 in the oxidizer undergoes decomposition into O radicals at high temperatures. These O radicals subsequently react with H radicals diffusing radially outward from the fuel mixture side to generate OH. A small amount of CH_4 leaks into the oxidizer stream and forms a “tail” which, although eventually consumed in the outer mantle of the flame, still can result in incomplete combustion. The higher the inlet velocity or the liftoff height, the more fuel leaks (see the plots of CH_4 for three different velocities). An important design criterion for gas burners is the avoidance of flame liftoff. The calculations in this chapter indeed prove that the flame liftoff will cause the problem of fuel leakage and the REDIM reduced mechanism also can accurately describe these processes and phenomena.

The maximum concentrations of O_2 and N_2 occur in the oxidizer stream (Coflow in Figure 6.1). N_2 is present in the whole computational domain, and no part of the jet flame is nitrogen-free. The maximum concentrations of the major species H_2O and CO_2 occur in the high temperature region. The results of H_2O and CO_2 obtained with the REDIM method agree very well with that computed by the detailed mechanism. The minor species mass fractions of OH and H_2, calculated by both the detailed mechanism and the REDIM reduced chemistry, show good agreement at the three inlet velocities. As for the small difference in minor species profiles, future work will increase the dimension of REDIM (e.g. using a 3D REDIM) to capture the flame structure, which can yield better results to predict minor species [27].

The CPU time of GRI3.0 in the EBIdnsFoam solver is 54.3, 54.56, 70.74 s for $U = 0.35$, 0.5 and 0.65 m/s, respectively, however, the CPU time of REDIMFoam with the corresponding REDIM reduced chemistry is 4.02, 4.10, 5.54 s, based on the same time step and mesh size. The relative CPU time of REDIM is only approximately 8 % of the detailed mechanism, which means that the REDIM method can significantly reduce the computational cost in the cases.

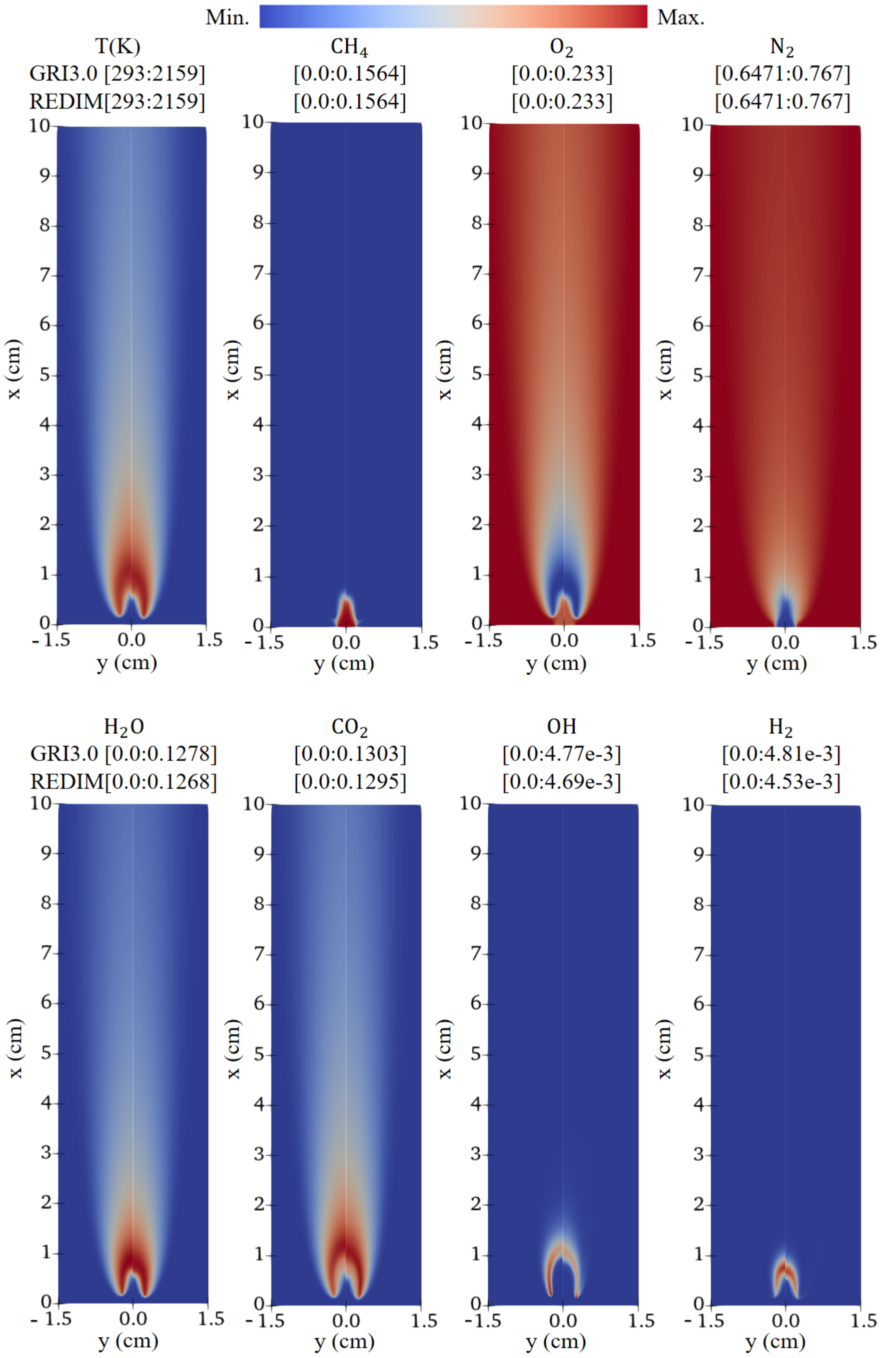

Figure 6.3: Computed isotherms and isopleths of selected species in mass fractions for $U = 0.35$ m/s; left half of each plot: GRI3.0, right half of each plot: REDIM.

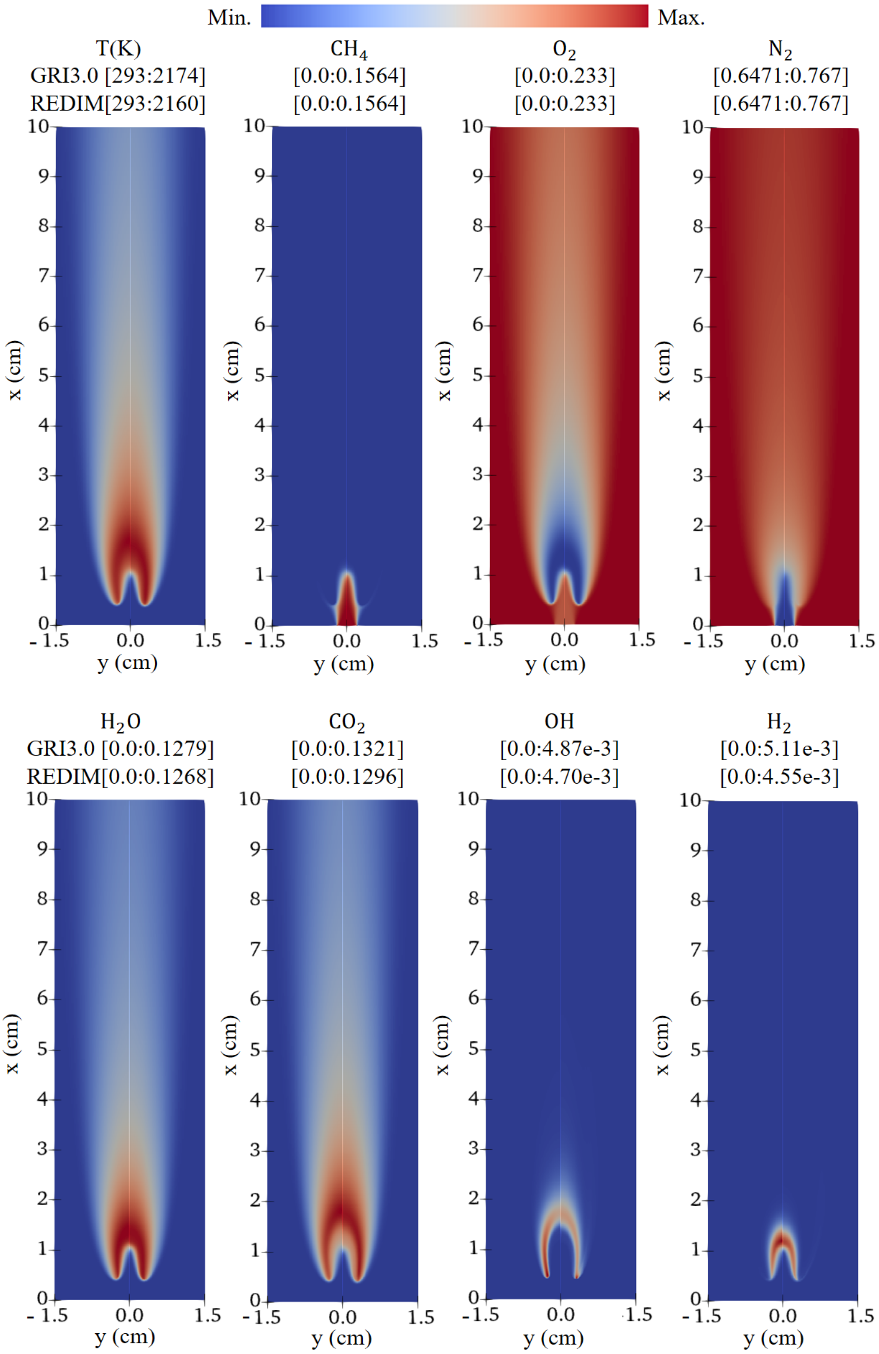

Figure 6.4: Computed isotherms and isopleths of selected species in mass fractions for $U = 0.5$ m/s; left half of each plot: GRI3.0, right half of each plot: REDIM.

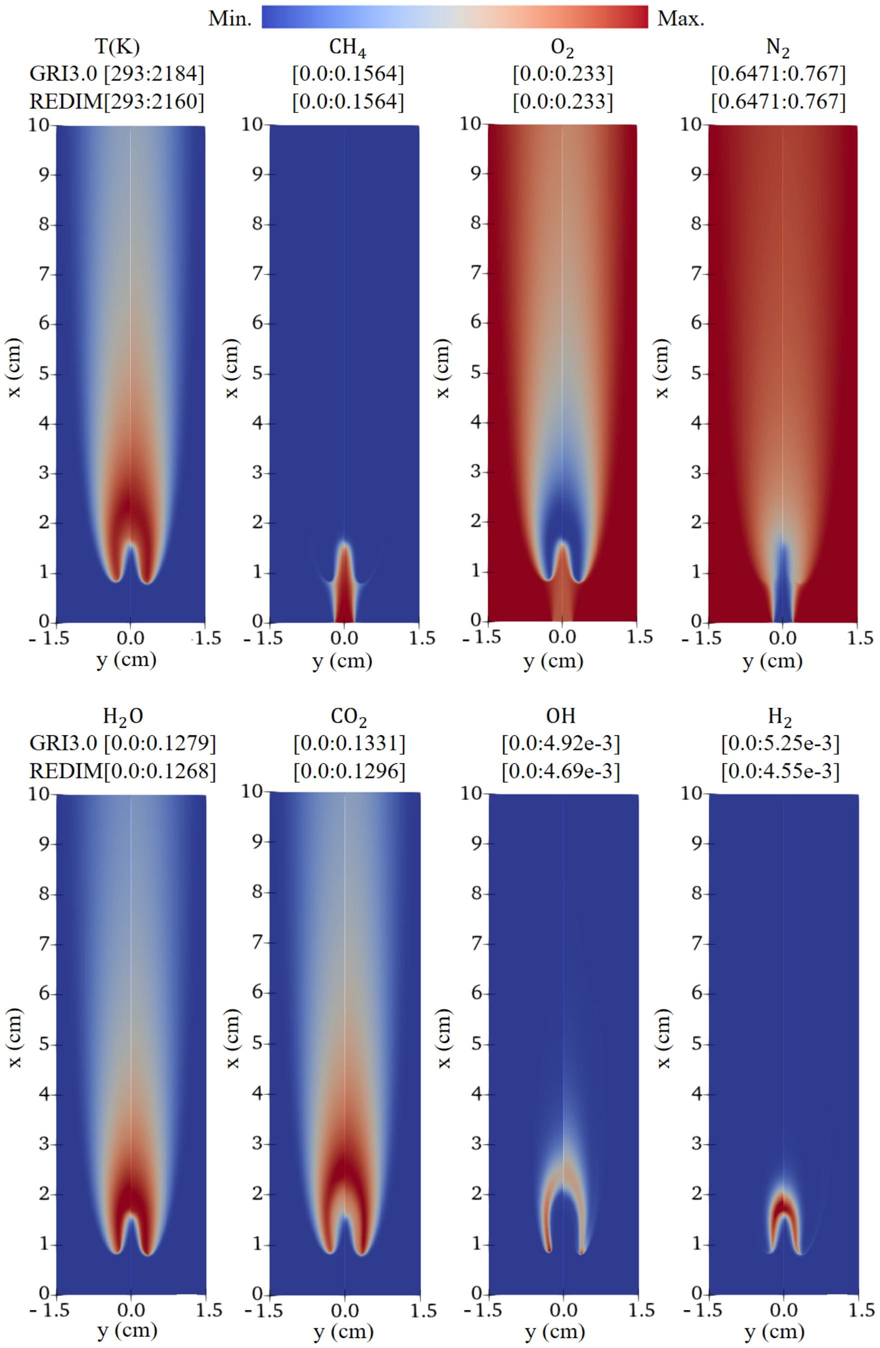

Figure 6.5: Computed isotherms and isopleths of selected species in mass fractions for $U = 0.65$ m/s; left half of each plot: GRI3.0, right half of each plot: REDIM.

6.3.2 Liftoff heights and flame lengths

The phenomenon of flame liftoff has been investigated and explained in much research (details see Refs. [35, 37, 38, 40–42]). The liftoff height x_{liftoff} is the shortest distance between the burner port and the flame front, which will increase with the increasing of inlet velocity until the flame blows out [12]. The measurement method of liftoff height is defined as the lowest x coordinates (throughout the whole flame) at which $T \geq 1000$ K and the flame length x_{length} is defined as the x coordinates of the location along the centerline where the temperature reaches a maximum [107].

Table 6.2: Comparison of liftoff heights computed by the GRI3.0 mechanism and the REDIM reduced chemistry (cm).

	$U = 0.35$ m/s	$U = 0.5$ m/s	$U = 0.65$ m/s
GRI3.0	0.16	0.41	0.83
REDIM	0.13	0.39	0.79

Table 6.3: Comparison of flame lengths computed by the GRI3.0 mechanism and the REDIM reduced chemistry (cm).

	$U = 0.35$ m/s	$U = 0.5$ m/s	$U = 0.65$ m/s
GRI3.0	1.12	1.70	2.36
REDIM	1.00	1.61	2.29

Comparison of liftoff heights and flame lengths for three inlet velocities is listed in tables 6.2 and 6.3. It is obvious that the liftoff heights calculated by the REDIM method are slightly smaller than the results obtained with the detailed mechanism. This result can be attributed to the assumed difference in the extinction strain rates between the two mechanisms. The extinction strain rate of the REDIM reduced chemistry may be a bit higher than that of the GRI 3.0, therefore the flame calculated by the REDIM method can be closer to the burner port, where strain rates are larger. This situation also occurs in the results of Ref. [107], which compared the liftoff heights obtained with the GRI 2.11 and GRI 3.0 mechanisms. It can be seen from the table 6.3 that the flame length increases with the increasing of velocity, which is consistent with the situation described in the related literature [133]. The flame heights obtained with the GRI 3.0 mechanism are a bit larger than the values from the REDIM method. The error in flame heights is larger at the inlet velocity of 0.35 m/s, but decreases as the velocity increases (the errors are 11 %, 5 % and 3 % at $U = 0.35$, 0.5 and 0.65 m/s, respectively). This may be due to the flame being very close to the nozzle at the velocity of 0.35

m/s, which changes the local laminar flame velocity at the stabilization point, but the extent to which this change affects the two mechanisms is slightly different.

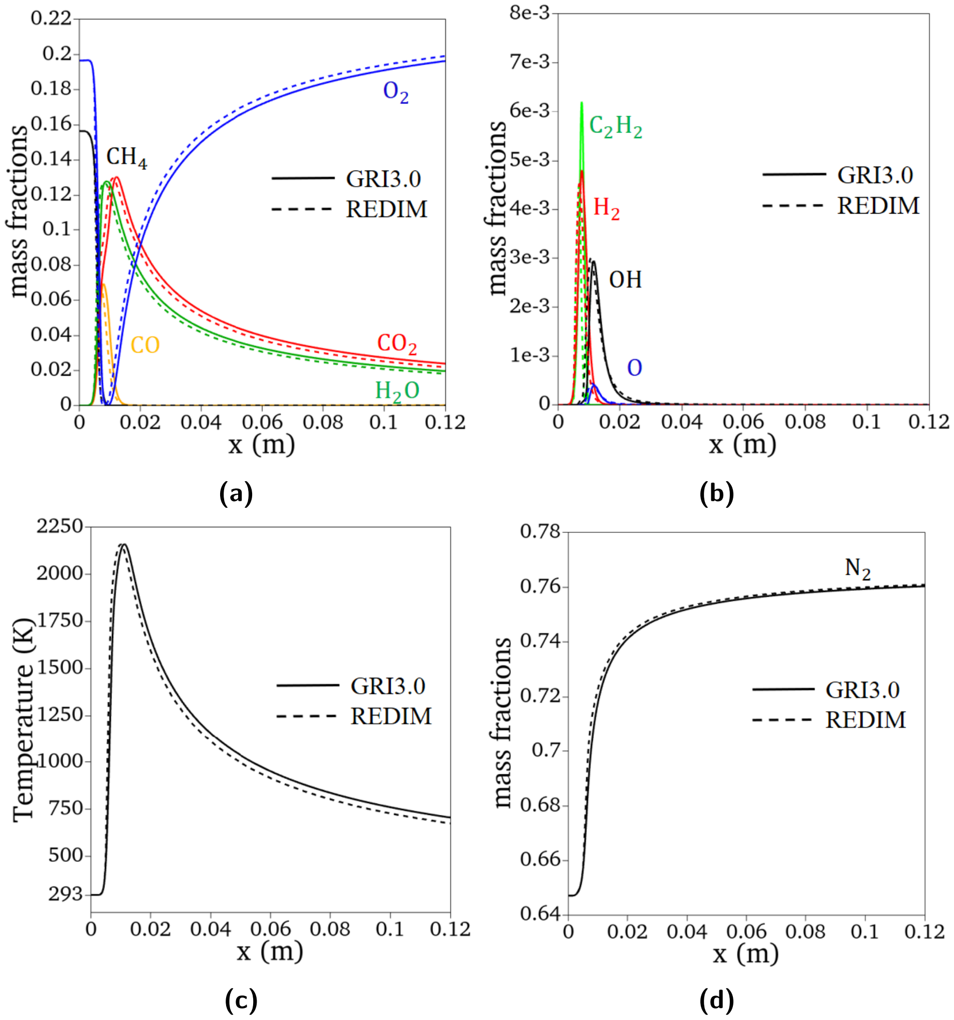

(a) **(b)**

(c) **(d)**

Figure 6.6: Axial profiles of selected species and temperature along the centerline for $U = 0.35$ m/s, solid line: GRI3.0, dashed line: REDIM.

6.3.3 Axial profiles

Figures 6.6, 6.7 and 6.8 show the selected species mass fraction profiles and temperature distribution along the centerline ($y = 0$) for different inlet velocities $U = 0.35$, 0.5 and 0.65 m/s. Comparing the temperature and

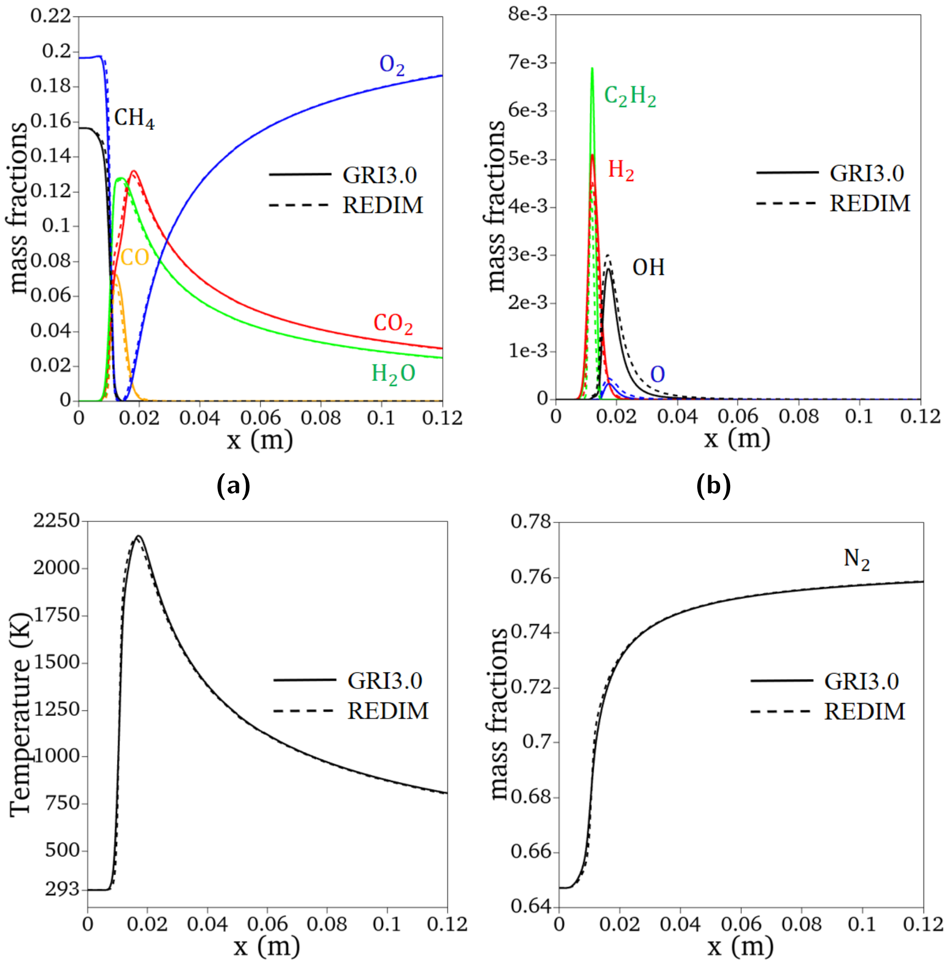

(a) **(b)**

(c) **(d)**

Figure 6.7: Axial profiles of selected species and temperature along the centerline for $U = 0.5$ m/s, solid line: GRI3.0, dashed line: REDIM.

composition distribution of the 2D jet flames along the centerline, it can be seen that the REDIM method describes the flame structure well. Although increasing the inlet velocity will enhance the flame liftoff effect, the REDIM method can still display good results, even for minor species O, OH and H_2.

Here we can see the consumption of the fuel CH_4 with O_2, the appearance of the intermediate species CO and consumed, finally forms CO_2 and H_2O in Figures 6.6a, 6.7a and 6.8a. The CO concentration peaks approximately where the CH_4 and O_2 concentrations approach zero, then continues to reduce as the CO is oxidized, whereas O_2 concentration continues to increase due to the

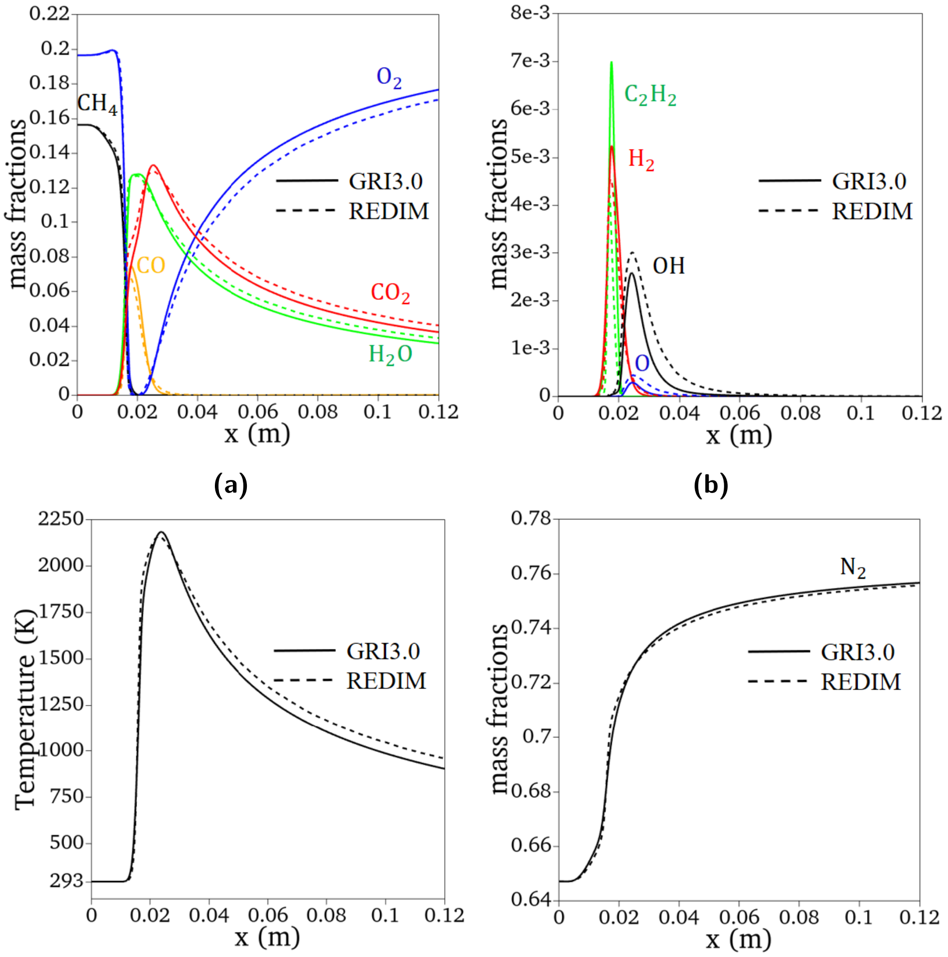

(a) **(b)**

(c) **(d)**

Figure 6.8: Axial profiles of selected species and temperature along the centerline for $U = 0.65$ m/s, solid line: GRI3.0, dashed line: REDIM.

diffusion of the oxidizer stream. This provides an insight that the oxidization of methane in the 2D jet flames follows the sequence $CH_4 \rightarrow CO \rightarrow CO_2$. For the products CO_2 and H_2O, after reaching the peak concentration, they will gradually decrease in the downstream of the flame due to diffusion. Note that the H_2O reaches its peak concentration sooner than the CO_2 in the flame. For the H-intermediates, H_2 and OH in Figures 6.6b, 6.7b and 6.8b, the peak concentration of H_2 occurs apparently earlier than that of OH, while the OH peak concentration appears in the high temperature region. In comparison to OH and H_2, the maximum value of O is significantly lower than the peak values observed for OH and H_2. The temperature profile shows the trend that it first increases, reaches the maximum value and then decreases. The reason for the decrease is the dilution with coflow air. N_2 distribution increases monotonically along the centerline, which is why it is selected as the first process variable.

A small discrepancy appears in the temperature and species O_2 downstream of the flame at $U = 0.65$ m/s, however, the error is still less than 6 %. Moreover, there is difference of minor species C_2H_2, which peak mass fraction obtained by the REDIM method is approximately 35 % smaller than that of the detailed mechanism, while the positions of C_2H_2 described by the two mechanisms are almost identical. We think it will be able to improve the accuracy of the reduced mechanism to calculate the C_2H_2 by using a higher dimensional REDIM.

6.3.4 Radial profiles

Due to the difference in lift height and flame length between detailed and simplified results, direct comparison of radial profiles obtained using the GRI3.0 and the REDIM method at the same specified x coordinates is not meaningful. To better describe the radial profiles of a flame, Bennett *et al.* defines a generalization ζ, which is a non-dimensional axial coordinate whose value ranges from 0 at $x = x_{\text{liftoff}}$ to 1 at $x = x_{\text{length}}$, as follows [107]:

$$\zeta = \frac{x - x_{\text{liftoff}}}{x_{\text{length}} - x_{\text{liftoff}}}. \tag{6.1}$$

Figures 6.9, 6.10 and 6.11 show the computed radial profiles of temperature and selected major species mass fractions of the detailed and reduced mechanisms for three different inlet velocities at four different values of ζ. The radial profiles calculated by the REDIM reduced chemistry have a very good agreement with the results obtained by the GRI3.0 mechanism. In Figures 6.9a, 6.10a and 6.11a, $\zeta = 0.1$, the radial profiles are shown at a x coordinate which is one-tenth of the flame height. The flame front is located at the point where the radial temperature reaches a maximum. The maximum values of CH_4 and O_2 in fuel mixture stream are on the centerline and their values decrease to 0 and a negligible value near the flame front, respectively. Subsequently, the O_2 concentration continues to rise to the value of 0.233 in the coflow stream, attributed to oxidizer diffusion. The maxima of the products H_2O and CO_2 locate near the flame front and reduce to zero outside of the reaction zone, while the peak position of H_2O is closer to the centerline than CO_2. The peak location of CO_2 corresponds approximately to the maximum temperature.

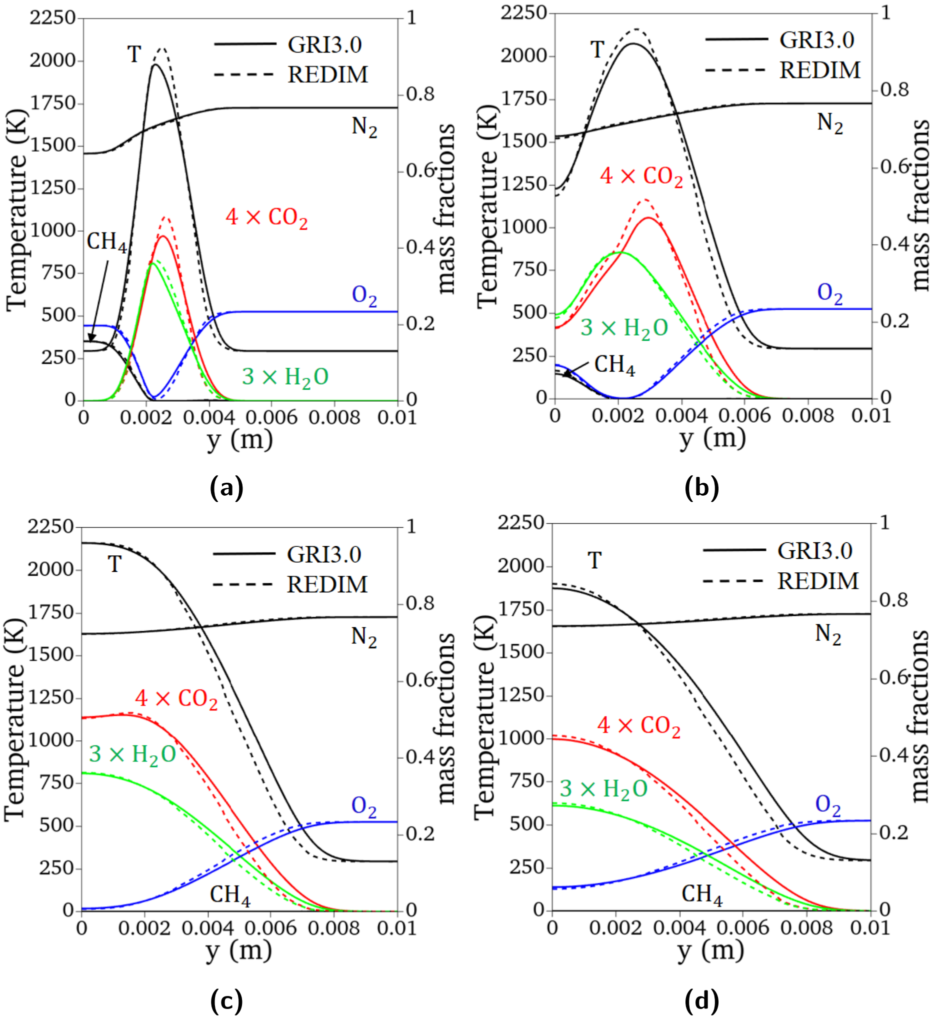

(a) (b) (c) (d)

Figure 6.9: Radial profiles of selected species and temperature for $U = 0.35$ m/s. (a) $\zeta = 0.1$, $x_{\mathrm{GRI3.0}} = 0.26$ cm, $x_{\mathrm{REDIM}} = 0.22$ cm, (b) $\zeta = 0.5$, $x_{\mathrm{GRI3.0}} = 0.64$ cm, $x_{\mathrm{REDIM}} = 0.57$ cm, (c) $\zeta = 1.0$, $x_{\mathrm{GRI3.0}} = 1.12$ cm, $x_{\mathrm{REDIM}} = 1.00$ cm, (d) $\zeta = 1.5$, $x_{\mathrm{GRI3.0}} = 1.60$ cm, $x_{\mathrm{REDIM}} = 1.44$ cm.

In terms of the composition of the reactant stream, as expected, the mass fraction of N_2 increases monotonically from 0.6471 near the centerline (fuel mixture stream) to 0.767 at further radial positions (coflow stream). It is shown that the profiles of $\zeta = 0.5$ in Figures 6.9b, 6.10b and 6.11b locate half of the way up the flame. The change of radial profiles in the temperature and composition at this point is roughly comparable to that of $\zeta = 0.1$, except that the value near the centerline undergoes a corresponding change due to

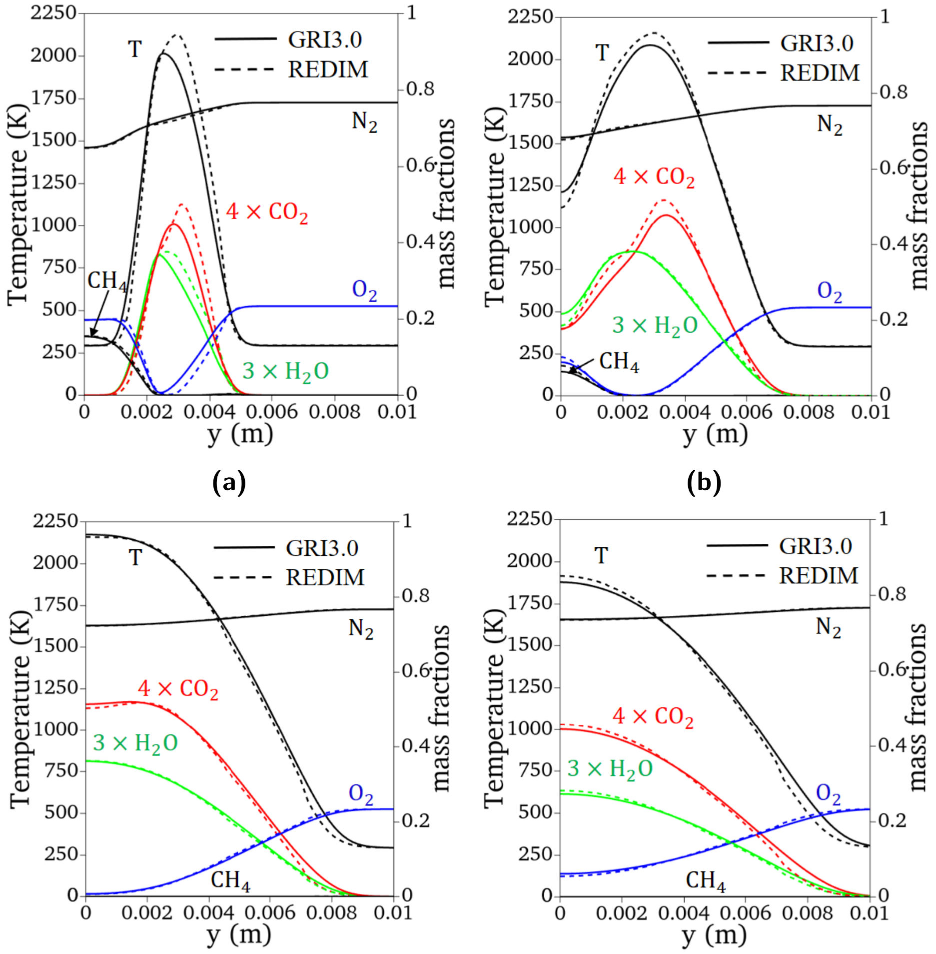

(a) **(b)**

(c) **(d)**

Figure 6.10: Radial profiles of selected species and temperature for $U = 0.5$ m/s. (a) $\zeta = 0.1$, $x_{\mathrm{GRI3.0}} = 0.54$ cm, $x_{\mathrm{REDIM}} = 0.51$ cm, (b) $\zeta = 0.5$, $x_{\mathrm{GRI3.0}} = 1.06$ cm, $x_{\mathrm{REDIM}} = 1.00$ cm, (c) $\zeta = 1.0$, $x_{\mathrm{GRI3.0}} = 1.70$ cm, $x_{\mathrm{REDIM}} = 1.61$ cm, (d) $\zeta = 1.5$, $x_{\mathrm{GRI3.0}} = 2.35$ cm, $x_{\mathrm{REDIM}} = 2.22$ cm.

diffusion and reaction. The values for the temperature, products (H_2O and CO_2) and N_2 increase near the centerline, while the value for the reactants (CH_4 and O_2) decrease. In Figures 6.9c, 6.10c and 6.11c, where $\zeta = 1.0$, the results for temperature and major species are shown at x-levels at which the temperature peaks on the centreline and the fuel is consumed completely. The temperature and products level off on the centerline and decrease with the increasing of y coordinate, while O_2 increases from a negligible value to its value of 0.233 in the coflow stream. Figures 6.9d, 6.10d and 6.11d display the

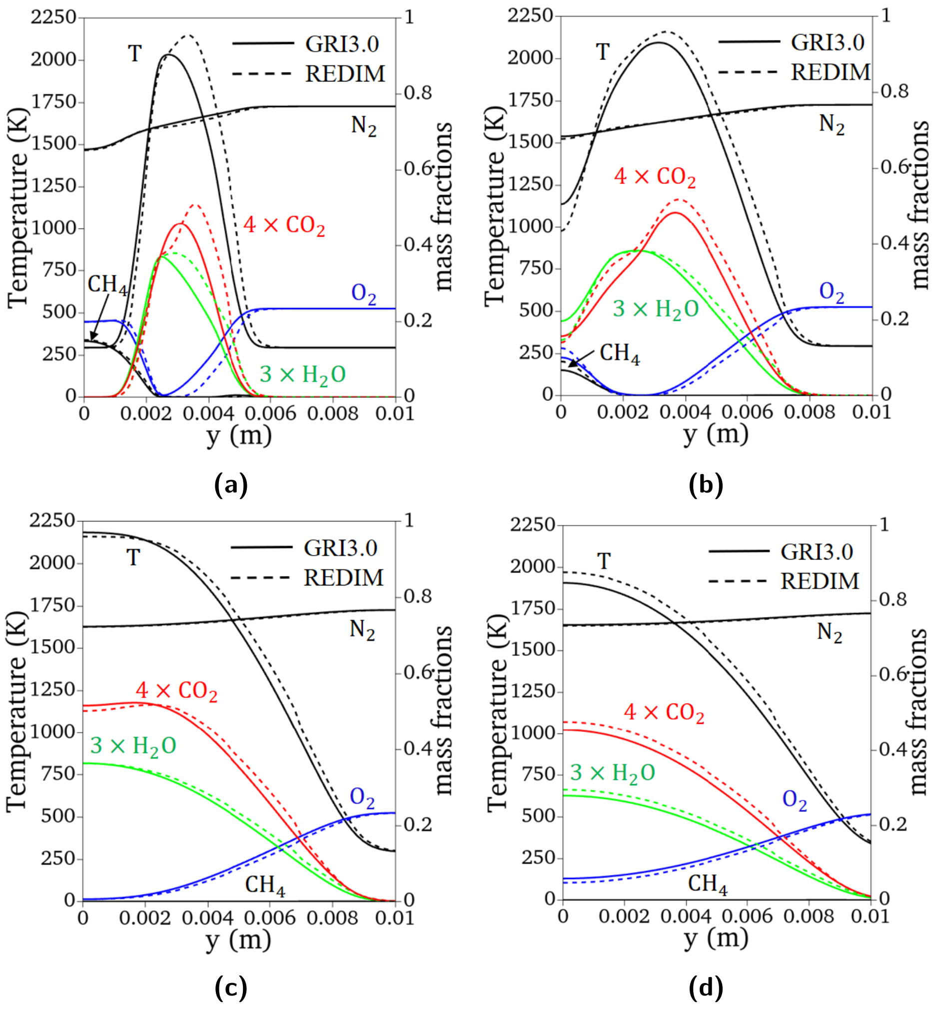

(a) **(b)** **(c)** **(d)**

Figure 6.11: Radial profiles of selected species and temperature for $U = 0.65$ m/s. (a) $\zeta = 0.1$, $x_{\text{GRI3.0}} = 0.98$ cm, $x_{\text{REDIM}} = 0.94$ cm, (b) $\zeta = 0.5$, $x_{\text{GRI3.0}} = 1.60$ cm, $x_{\text{REDIM}} = 1.54$ cm, (c) $\zeta = 1.0$, $x_{\text{GRI3.0}} = 2.36$ cm, $x_{\text{REDIM}} = 2.29$ cm, (d) $\zeta = 1.5$, $x_{\text{GRI3.0}} = 3.13$ cm, $x_{\text{REDIM}} = 3.04$ cm.

results of radial profiles at $\zeta = 1.5$. The temperature and products decrease as y coordinate increases, while O_2 and N_2 increase to the values of 0.233 and 0.767 in the oxidizer.

A small difference occurs in the temperature and species CO_2 at $\zeta = 0.1$ for $U = 0.65$ m/s. The errors for temperature and CO_2 are approximately 6 % and 10 %, respectively. The errors may be caused by the different liftoff height obtained with the detailed and reduced mechanisms, which can not be completely eliminated despite the use of non-dimensional axial coordinates. On the other hand, the gradient estimate from flamelets has small influence on the generation of 2D REDIM as well, which may cause the discrepancy of results. Generally speaking, the REDIM method can well describe the radial profiles of the 2D jet flames.

6.4 Flame structures of non-steady state

6.4.1 Problem formulation

In the previous sections, the calculations are focused on the steady flames, however, most practical combustion devices often work under non-steady state and turbulent conditions. To be able to simulate realistic flame structures, it is essential to incorporate oscillating flow fields into chemical kinetics. Oscillating laminar flame systems bridge the gap between laminar and turbulent combustion [43, 134]. These flames can be used to investigate the complex coupling chemical reaction and fluid flow. In addition, some studies have focused on variation in generation of soot between steady and oscillating flames. For instance, measurements and calculations indicated that the soot production in an oscillating flame is four to five times higher than that in a steady flame with the same average fuel velocity [43–45].

In this section, we mainly show the transient results of the 2D jet flames, where the inlet velocity of the main jet oscillates. The study of the dynamic response of the flame to velocity is of great use in the further investigation of turbulent combustion. The velocity of coflow is set to 0.5 m/s and assumed to be uniform. The inlet velocity of the main jet is defined by:

$$U = U_0 + A\sin(2\pi f t), \tag{6.2}$$

where U_0 = 0.5 m/s, amplitude A = 0.15 m/s (30 % perturbation), and f denotes frequency (from 10 to 1000 Hz). Other numerical set-up for the flames is the same as that used in the steady state flames (see section 6.2). Our goals are to compare the results of detailed and reduced mechanisms at different times within a cycle.

The variation of flame structure with the changing of inlet velocity can be described by the flame length in the steady flames. However, in the oscillating flames, especially in higher frequencies, the flame length becomes no longer sensitive to time-varying velocity, as shown in Figure 6.17 and 6.19. In order to describe the flame variation, Mohammed *et al.* [43] defined the concept of a low-temperature core above the burner along the axis of symmetry. There was no explicit definition of the length of the low-temperature core in Ref. [43]. In this work, we define it as the distance from the first temperature gradient peak along the centerline to the burner nozzle exit in the following. In the steady-state cases, as the fuel mass flow rate increases, the length of low-temperature core increases and the flame length gets longer as well.

6.4.2 Results and discussion

6.4.2.1 Temporal and spatial behaviour

In this section, we examine the flame responses resulting from different oscillating frequencies by conducting a comprehensive analysis of the temporal and spatial behavior of 2D jet flames [135]. This analysis involves results obtained from both detailed and reduced mechanisms to validate the performance of the REDIM method in system dynamics.

Perturbation propagation

When discussing the impact of perturbations on flames, the first aspect to consider is understanding how perturbations reach the flame, whether they undergo alterations in the process (e.g. in amplitude), and whether there are situations in which perturbations fail to reach the flame. An answer to these questions can be obtained by analyzing the temporal variations in the length of the low-temperature core. Figure 6.12 shows the variation of the length of the low-temperature core with the time-varying velocity during 1.25 cycles. The black lines in the figures denote the time-varying inlet velocity of main jet. The blue and red lines represent the lengths of the low-temperature core obtained with the detailed and reduced mechanisms, respectively. There is a phase shift between the oscillating velocity and the lengths of the low-temperature core in Figure 6.12a-6.12d. The peak of the low-temperature core length for 10, 20, 50, and 100 Hz occurs with a noticeable delay after the inlet velocity reaches its maximum. After the occurrence of the maximum of the length of the low-temperature core at 50 Hz and 100 Hz, the length rapidly decreases. At these frequencies, the oscillation is so strong that it can change the flame shape so that the two flame branches temporarily come into contact, causing sharp changes in the low-temperature core length (see Figure 6.17). The amplitude of the length is very small at 200 Hz, although at the higher frequencies, such as above 500 Hz, the length remains constant. The overall low-temperature core length variation obtained with the REDIM reduced chemistry is in very good agreement with the detailed chemistry simulation.

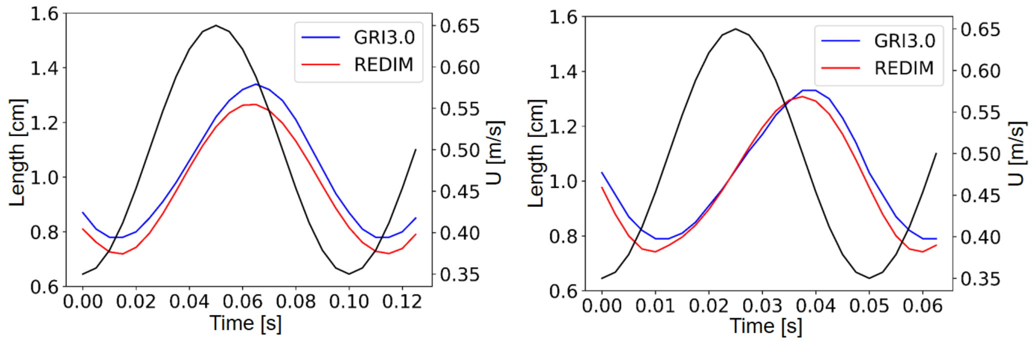

(a) 10 Hz **(b)** 20 Hz

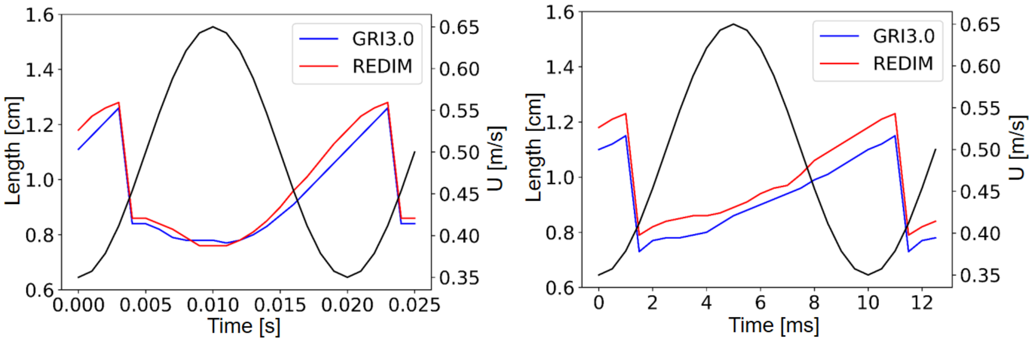

(c) 50 Hz **(d)** 100 Hz

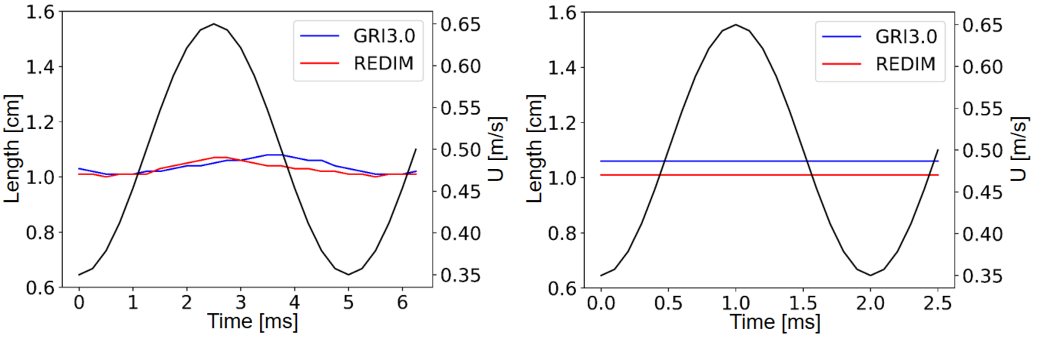

(e) 200 Hz **(f)** 500 Hz

Figure 6.12: Length of low-temperature core above the burner for different frequencies (10, 20, 50, 100, 200 and 500 Hz); blue line: GRI3.0, red line: REDIM, black line: inlet velocity at main jet.

The maximum error for the low-temperature core length is approximately 8.2 %.

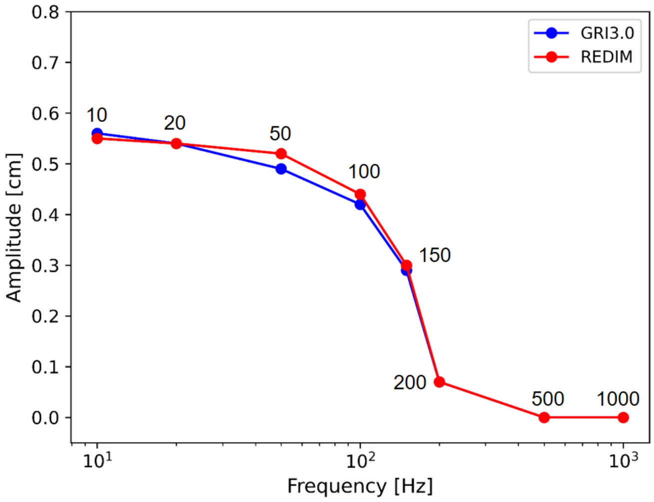

Figure 6.13: Amplitudes of length of low-temperature core over different frequencies (10, 20, 50, 100, 150, 200, 500 and 1000 Hz).

In order to effectively describe the dependence of the low-temperature core length on various frequencies, we plotted the amplitudes of the length (the difference between the maximum and minimum values) for different frequencies in Figure 6.13. The figure clearly illustrates a gradual decrease in amplitude as the frequency increases. When the frequency is more than 100 Hz, the amplitude exhibits a rapid decline, eventually reaching zero at 500 Hz. The REDIM method can describe the variation in the amplitude of the low-temperature core well, and the maximum error is less than 6.1 %. To illustrate the propagation of the oscillation, we analyze the velocity component U_x over the centerline at various time steps and frequencies, as shown in Figure 6.14. At low frequencies (10 Hz and 20 Hz), the velocity perturbation reaching the flame front remains almost constant. As a result, quasi-stationary values of the oscillation move within the flame region. At higher frequencies (50 Hz and 100 Hz), the oscillating velocity corresponds to a wavelike movement. Nevertheless, the amplitude of the oscillating velocity is entirely levelled to a constant mean value before it reaches the flame region at 500 Hz.

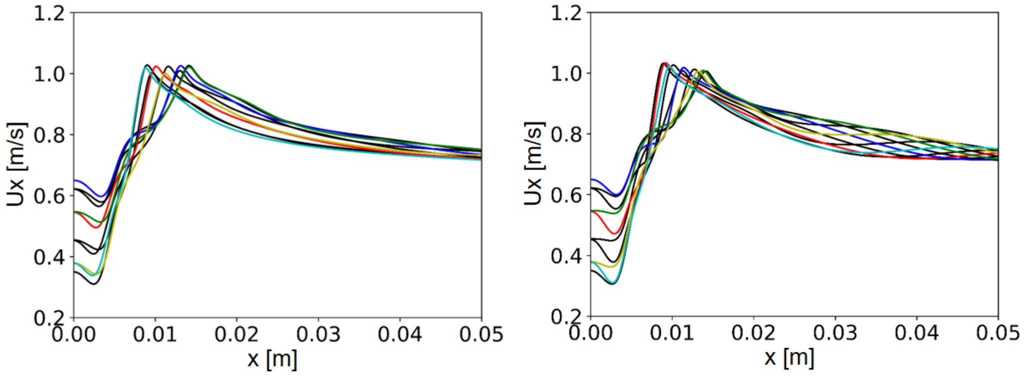

(a) 10 Hz **(b)** 20 Hz

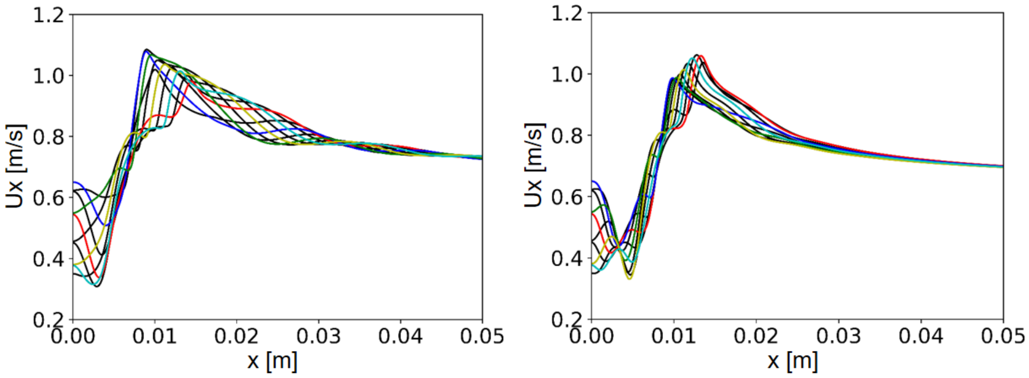

(c) 50 Hz **(d)** 100 Hz

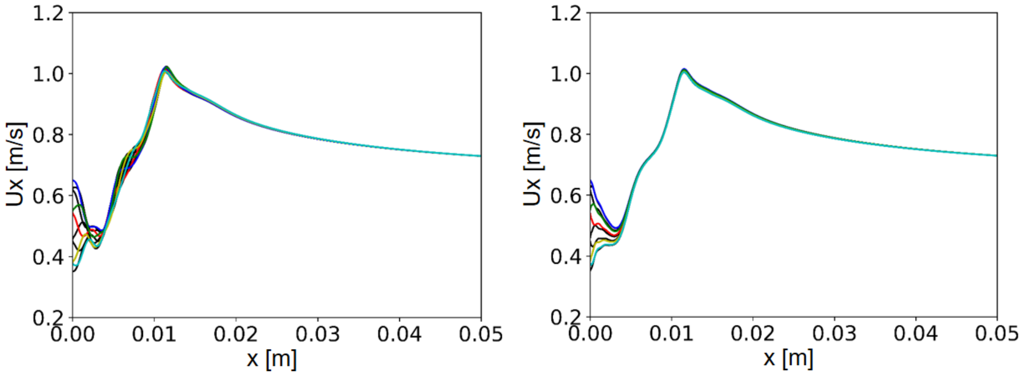

(e) 200 Hz **(f)** 500 Hz

Figure 6.14: Oscillation of velocity component U_x along the centerline for different frequencies (10, 20, 50, 100, 200 and 500 Hz); different color represents different time steps.

The phenomenon of quasi-stationary perturbations at low frequencies and wavelike propagation at high frequencies can be elucidated through the concept of “wavelength”, and the wavelength can be defined as [32]:

$$\lambda = \frac{\bar{U}}{f}, \tag{6.3}$$

where $\bar{U}$ denotes the bulk velocity of the main jet, which can be regarded as constant and is equal to U_0 in this thesis. According to Eqn. (6.3), an increase in the frequency corresponds to a decrease in the wavelength, which results in an amplified curvature of the single wave peak, leading to faster dissipation [7]. At low frequencies (10 Hz and 20 Hz), the wavelength can be exceptionally long and exceeds the system's dimensions, resulting in only quasi-stationary values of the perturbation reaching the flame. Conversely, at higher frequencies (50 Hz and 100 Hz), the wavelength becomes smaller than the system dimensions, allowing a perturbation wave to reach the flame region. Affected by increasing dissipative processes with rising frequency, the faster dissipative processes tend to level the oscillating velocity to a mean value, therefore, the perturbation at very high frequency (200 Hz and 500 Hz) is dissipated on its way to the flame region, as shown in Figure 6.14e and 6.14f.

Comparison of temperature field and soot precursor with detailed and reduced models at 10 Hz

In the following Figures 6.15-6.19, the left half of each plot is the result of the simulation using the detailed reaction mechanism, and the right half is the result of the REDIM reduced mechanism. Figure 6.15 displays the temperature contour plot of the steady and oscillating flames at 10 Hz. The contour plot for the steady flame is shown in Figure 6.15a and Figures 6.15b-6.15f are the results of the oscillating flame at 0.02 s intervals (1/5 of the oscillation period). Analyzing together with Figure 6.12a and Figure 6.15, we can observe that the low-temperature core during the oscillation cycle where the velocity is increasing (Figures 6.15b and 6.15c) and when the velocity is decreasing (Figures 6.15d-6.15f) are qualitatively different, while the transient cases calculated by the REDIM method have good agreement with the results obtained by the GI3.0 mechanism. In all the computed results, the liftoff heights obtained by the detailed and reduced mechanisms vary from 0.33 to 0.44 cm and 0.30 to 0.43 cm, respectively. In contrast, the steady-state results yield liftoff heights of 0.41 cm and 0.39 cm respectively (see section 6.3.2), which are similar to those of the transient results. The simulations demonstrate that the oscillations applied to the inlet velocity of the main jet result in analogous oscillations of all other variables. The total length of the hot downstream plume of the flame serves as a more accurate indicator of the flame's forced oscillatory nature. The change of the total length of the hot plume can also be explained by the exceptionally long wavelength, which is larger than the system dimension and can effect the downstream flow field (see Figure 6.14a).

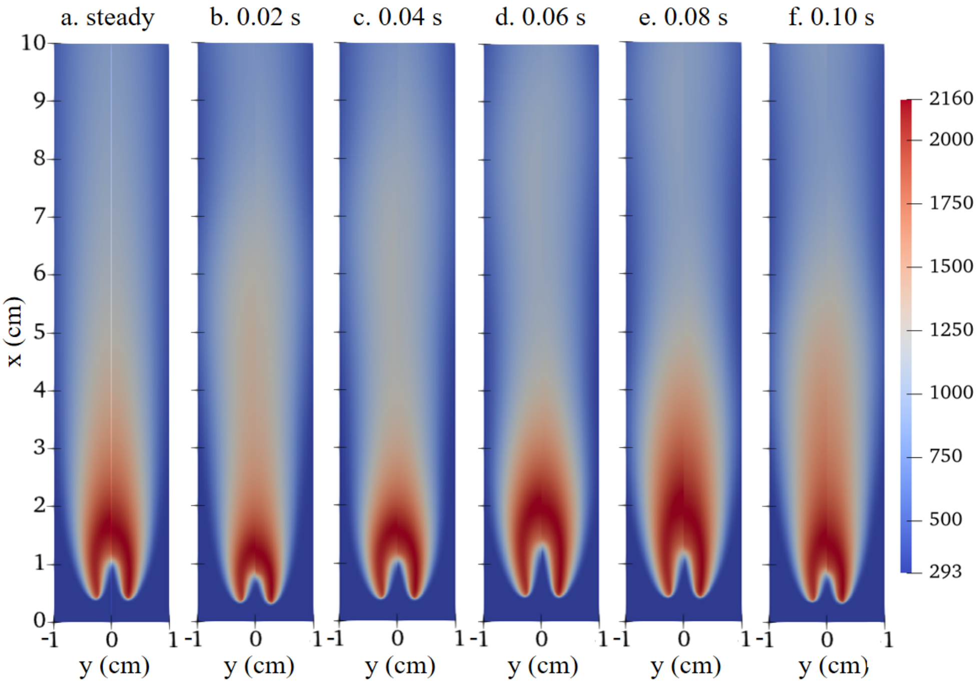

Figure 6.15: Temperature contour plot (units: K) for the steady and oscillating (10 Hz) flames with the detailed and reduced mechanisms; left half of each plot: GRI3.0, right half of each plot: REDIM.

As previously mentioned, a time-varying flame can significantly increase soot production [43, 44]. However, note that a submodel of soot formation is not incorporated into the current mechanisms used in the work. Thus, our focus is primarily on comparing the soot precursor C_2H_2, obtained by the detailed and REDIM reduced mechanisms respectively, to verify the performance of the REDIM method. Table 6.4 shows the variations in C_2H_2 and the liftoff heights of the oscillating flame at different frequencies (10, 100 and 500 Hz) compared to the steady-state results. Figure 6.16 shows the acetylene mass fraction contour plot and the C_2H_2 mass fraction along the centerline of the steady and oscillating flames with the GRI3.0 and the

REDIM method during one oscillation period (10 Hz). The peak C_2H_2 mass fraction increases by 16.0 % compared to the results in the steady state with the same detailed mechanism, and varies by almost 34.1 % during one oscillation period (see Figure 6.16g). It can be observed that the region with C_2H_2 mass fraction ($Y_{C_2H_2} > 0.006$) can increase in area by more than a factor of four during an oscillation. In the reduced mechanism, the peak C_2H_2 mass fraction shows an increase of 18.0 % compared to the results with the REDIM method in steady state, and varies by almost 31.1 % during a period. Additionally, we can observe that the area with C_2H_2 mass fraction ($Y_{C_2H_2} > 0.004$) can increase by at least a factor 4 during a cycle. Since the peak of C_2H_2 mass fraction obtained by the REDIM method is 33.3 % smaller than the result of the detailed mechanism (see Figure 6.16g), the iso-surface with a mass fraction of 0.004 is selected as the comparison of the reduced mechanism between the steady and transient flames. The peak mass fraction of C_2H_2 ($t = 0.06$ s in Figure 6.16) appears after the inlet velocity of the main jet has reached its maximum ($t = 0.05$ s in Fig. 6.12a), which indicates the phase shift between the maximum of the inlet velocity and the maximum of C_2H_2 mass fraction. Despite the reduced mechanism yielding the lower mass fractions of C_2H_2 compared to the full GRI3.0 mechanism, the REDIM method is still capable of predicting the trend of C_2H_2 and thus correctly capturing the impact of transient flows on the flame dynamics. Accuracy could be improved by increasing the dimension of the REDIM.

Table 6.4: Comparison of C_2H_2 mass fraction between steady and oscillating flames.

Cases	Increase of peak	Variation in one cycle	Relative area increase	Liftoff height (cm)
GRI3.0 (10 HZ)	16.0 %	34.1 %	4	[0.33, 0.44]
REDIM (10 Hz)	18.0 %	31.1 %	4	[0.30, 0.43]
GRI3.0 (100 HZ)	9.7 %	29.3 %	6	[0.49, 0.52]
REDIM (100 Hz)	0.2 %	13.2 %	2	[0.50, 0.52]
GRI3.0 (500 HZ)	0 %	0 %	1	0.41
REDIM (500 Hz)	0 %	0 %	1	0.39

Comparison of temperature field and soot precursor with detailed and reduced models at 100 Hz

In Figure 6.17, we present temperature contour plots of the steady and oscillating flames at 100 Hz. The computed contour plot for the steady flame is shown in Figure 6.17a. Figures 6.17b-6.17f are the results of the

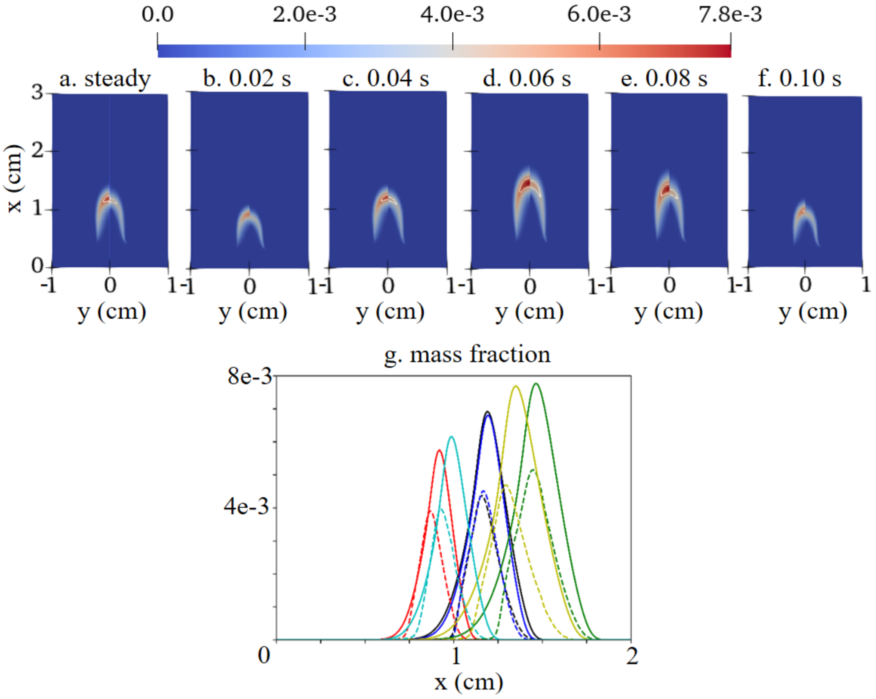

Figure 6.16: C_2H_2 mass fraction contour plot for the steady and oscillating (10 Hz) flames with the detailed and reduced mechanisms (a-f); left half of each plot: GRI3.0, right half of each plot: REDIM; different colored lines in (g) (solid: GRI3.0, dashed: REDIM) denote the steady and oscillating C_2H_2 mass fraction along the centerline, black (a), red (b), blue (c), green (d), yellow (e), cyan (f).

oscillating flame at 2, 3.5, 4.5, 7 and 10 ms intervals. Analyzing together with Figure 6.12d, we can see that the length of the low-temperature core is at its maximum at 10 % of the oscillation period, while its minimum occurs at 15 % of the time of oscillation. In all the computed oscillating results, the liftoff heights obtained by the detailed and reduced mechanisms vary from 0.49 to 0.52 cm and 0.50 to 0.52 cm, respectively. However, the corresponding values in the steady-state results are 0.41 cm and 0.39 cm. It can be clearly seen that the liftoff heights in the oscillating flames are larger than the value in the steady flame. This shows that the oscillation of the main jet at 100 Hz may change the local extinction strain rate. Moreover, the main jet velocity oscillation at 100 Hz also changes the shape of the flame front, compared to the steady-state result (see Figure 6.17). The structure of the flame at 100 Hz deviates from the structure shown in the steady flame, especially for the inner cone. Similar change in flame structure is observed at 50 Hz and 150 Hz (not shown), however the change is less pronounced than in the 100 Hz case. This can explain why the length of the low-temperature core decreases rapidly after reaching its maximum in Figures 6.12c and 6.12d. In comparison to the 10 Hz result, the total length of the flame's hot plume at 100 Hz remains almost unchanged. This observation indicates that, in this scenario, the oscillating velocity exhibits a wavelike movement that dissipates as it passes through the flame region, exerting minimal influence on the downstream flow field (see Figure 6.14d). It is encouraging to note that the REDIM method is capable of accurately describing the changes in the liftoff height and flame shape induced by oscillating velocity.

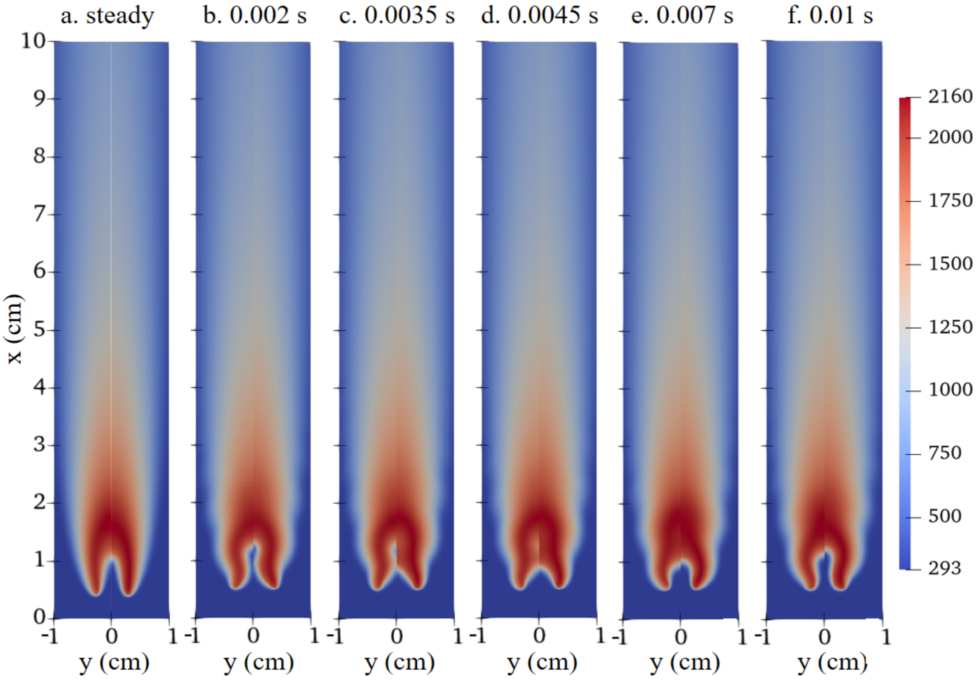

Figure 6.17: Temperature contour plot (units: K) for the steady and oscillating (100 Hz) flames with the detailed and reduced mechanisms; left half of each plot: GRI3.0, right half of each plot: REDIM.

The computed acetylene mass fraction contour plot of the steady and oscillating flames with the GRI3.0 mechanism and the REDIM method during one cycle (100 Hz) are shown in Figure 6.18. The peak C_2H_2 mass fraction increases by 9.7 % compared to the results in the steady state with the GRI3.0 mechanism, and varies by almost 29.3 % during a period (see Figure 6.18g). It can be observed that the region with C_2H_2 mass fraction ($Y_{C_2H_2} > 0.006$) increases in area by more than a factor of 6 during an oscillation. In the reduced mechanism, the peak C_2H_2 mass fraction shows an increase of 0.2 % compared to the results in the steady state with the REDIM reduced chemistry, and varies by almost 13.2 % during a period. Additionally, we can observe that the area with C_2H_2 mass fraction ($Y_{C_2H_2} > 0.0025$) can increase by a factor of 2 during an oscillation. Since the increase of the peak of C_2H_2 mass fraction and variation of C_2H_2 in the reduced mechanism are smaller than the 10 Hz results, in order to compare the changes in area, the iso-surface with a mass fraction of 0.0025 was selected. Although the peak mass fraction of C_2H_2 is lower at 100 Hz, the spatial extent with high mass fractions still increases. This indicates that at 100 Hz, the oscillating flame produces larger amounts of C_2H_2 than that in a steady flame. The REDIM method can still describe the variation of C_2H_2 reasonably although only two progress variables are used.

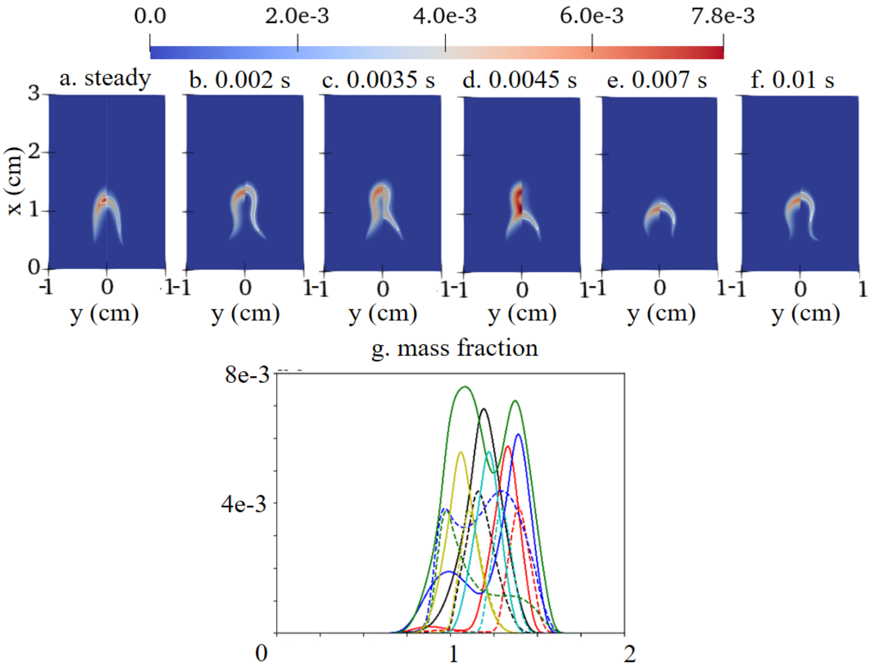

Figure 6.18: C_2H_2 mass fraction contour plot for the steady and oscillating (100 Hz) flames with the detailed and reduced mechanisms (a-f); left half of each plot: GRI3.0, right half of each plot: REDIM; different colored lines in (g) (solid: GRI3.0, dashed: REDIM) denote the steady and oscillating C_2H_2 mass fraction along the centerline, black (a), red (b), blue (c), green (d), yellow (e), cyan (f).

Comparison of temperature field and soot precursor with detailed and reduced models at 1000 Hz

Figure 6.19 shows the contour plots of temperature (left two figures) and C_2H_2 mass fraction (right two figures) of the steady solution and oscillating flame at 1000 Hz. In all the computed transient results, the liftoff heights, temperature and C_2H_2 mass fraction are same as the results of the steady-state flame. This indicates that, in both the reduced and detailed mechanisms, the velocity perturbation dissipates completely within the liftoff height before reaching the flame region at high frequencies, resulting in no impact on the flame itself.

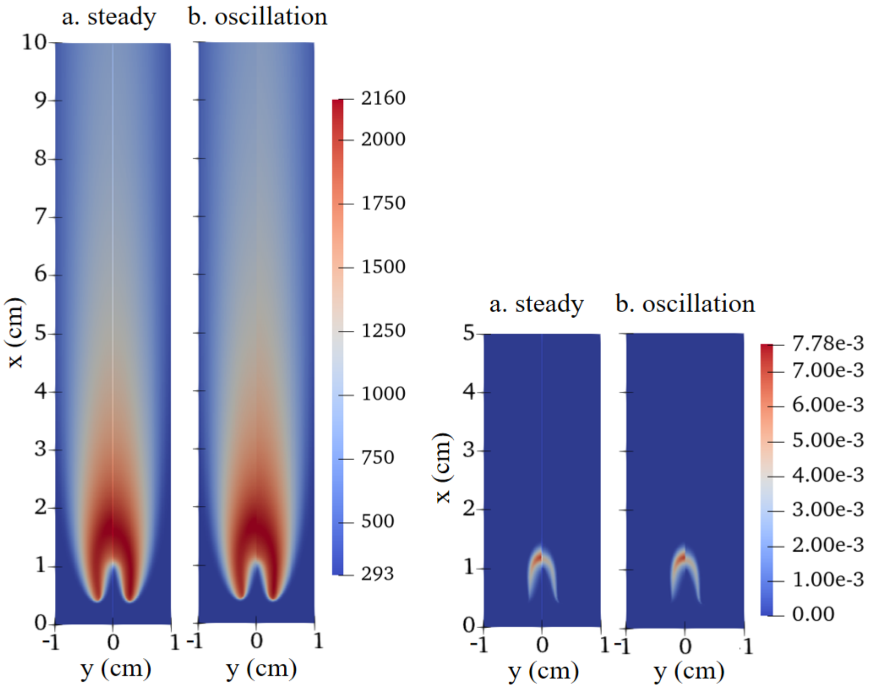

Figure 6.19: Temperature contour plot (units: K) for the steady and oscillating (1000 Hz) flames with the detailed and reduced mechanisms; left half of each plot: GRI3.0, right half of each plot: REDIM.

6.4.2.2 State space behaviour

After investigating the results of detailed and reduced mechanisms in temporal and spacial space, the influence of the oscillating velocity onto the 2D jet flames is studied by analysing different species in state space.

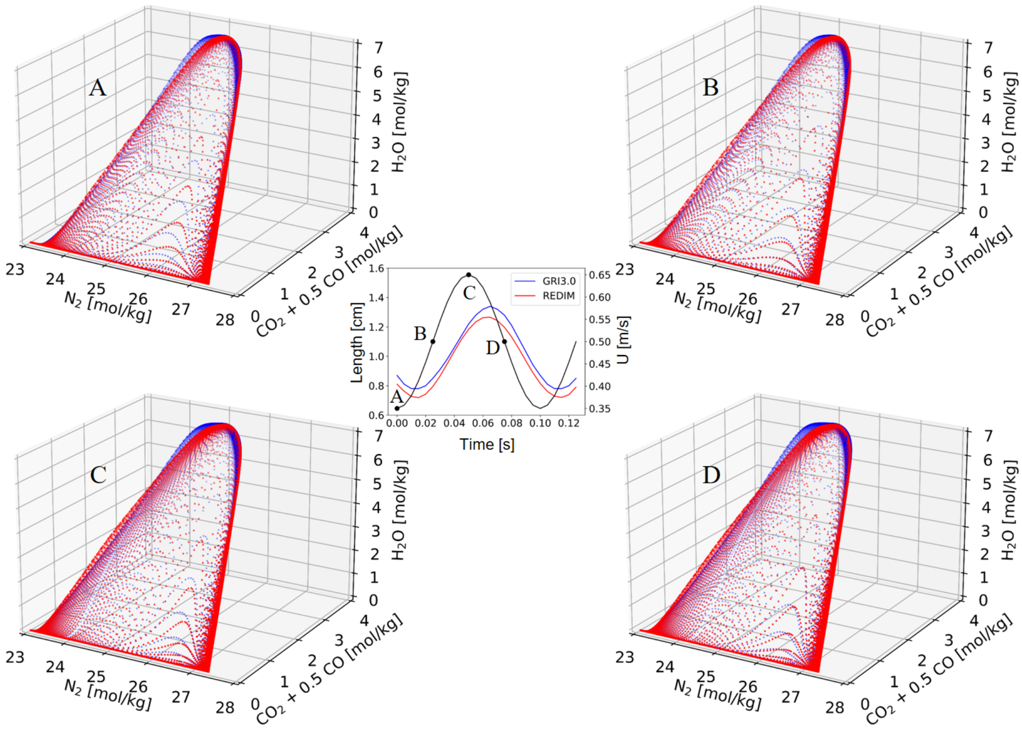

Figure 6.20: H_2O specific mole number computed by the GRI3.0 mechanism and the REDIM method projected on the specific mole number of $(\phi_{N_2}, \phi_{CO_2} + 0.5\phi_{CO})$ at 10 Hz; blue: GRI3.0, red: REDIM.

Figure 6.20 displays H_2O specific mole number for 10 Hz computed by the GRI3.0 mechanism and the REDIM method projected onto the progress variable $(\phi_{N_2}, \phi_{CO_2} + 0.5\phi_{CO})$, in which points A, B, C, and D represent inlet velocities (0.35, 0.5, 0.65, and 0.5 m/s) at different time steps (0, 0.025, 0.05, and 0.075 s). It can be seen that the results with the REDIM reduced chemistry in the state space have very good agreement with the results of detailed mechanism at the four different time steps. In this process, the manifold does not change much with the perturbation of the inlet velocity. Figure 6.21 demonstrates the projection of the manifold of specific mole number H_2O at 100 Hz onto the same progress variable. In this figure, the points A, B, C, and D correspond to the inlet velocities same as those at 10 Hz, with different time steps of 0, 2.5, 5, and 7.5 ms, respectively. In Figure 6.21, it is evident that the manifold at point B exhibits notable difference compared to the other three figures. The result represented by point B (2.5 ms) in the state space is approximately similar to the result depicted in Figure 6.17b with the time step of 2 ms in physical space. The observed phenomenon is attributed to the alteration of the inner cone within the flame structure, which is induced by the oscillating velocity at the fuel nozzle.

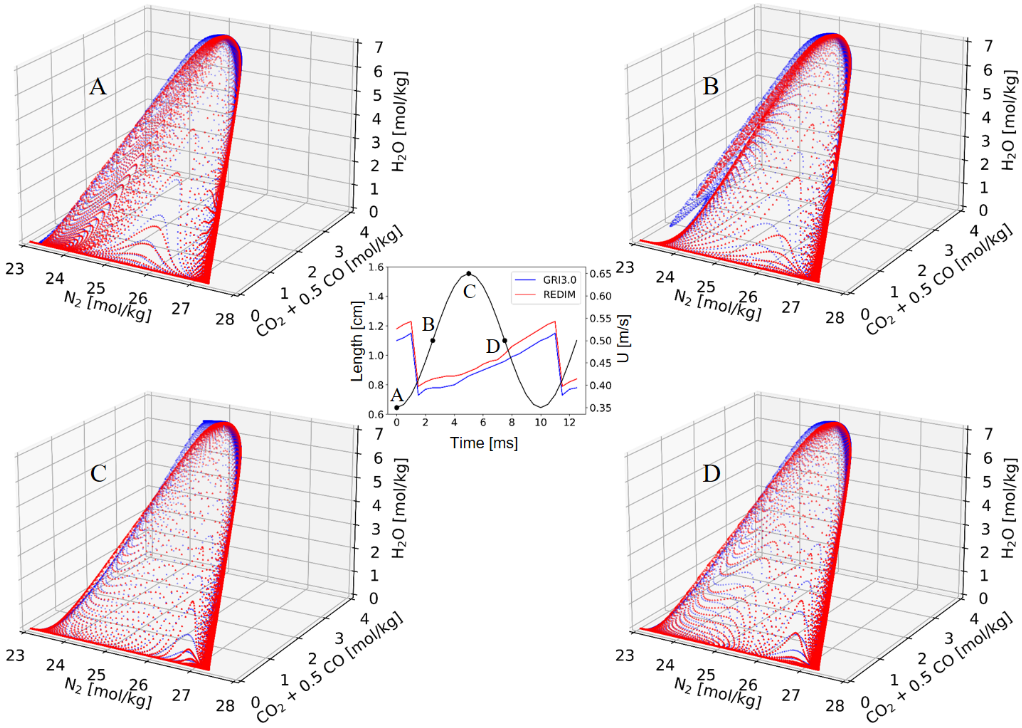

Figure 6.21: H_2O specific mole number computed by the GRI3.0 mechanism and the REDIM method projected on the specific mole number of $(\phi_{N_2}, \phi_{CO_2} + 0.5\phi_{CO})$ at 100 Hz; blue: GRI3.0, red: REDIM.

To provide a clearer depiction of the evolving process of the inner cone within the flame structure, we have plotted figures with smaller time intervals at 100 Hz, illustrating the state space of various species (CH_4 and CO) computed by the GRI3.0 mechanism, as shown in Figures 6.22 and 6.23. Points 1, 2, 3, and 4 correspond to different time steps: 1.5, 2.5, 3.5, and 4.5 ms, respectively. It is noteworthy that point 2 shares the same time step as point B in Figure 6.21. The structural changes in the inner cone of the flame result in the separation of some unburnt methane from the primary fuel flow, as shown in point 1 of Figure 6.22. From point 1 to point 4, there is a gradual decrease in methane concentration, accompanied by an increase in CO concentration. This can be attributed to the oxidation of methane, where it is initially converted into intermediate CO and subsequently formed into CO_2 and H_2O. The analysis of these results reveals that the REDIM method can accurately describe the structural changes occurring at the inner

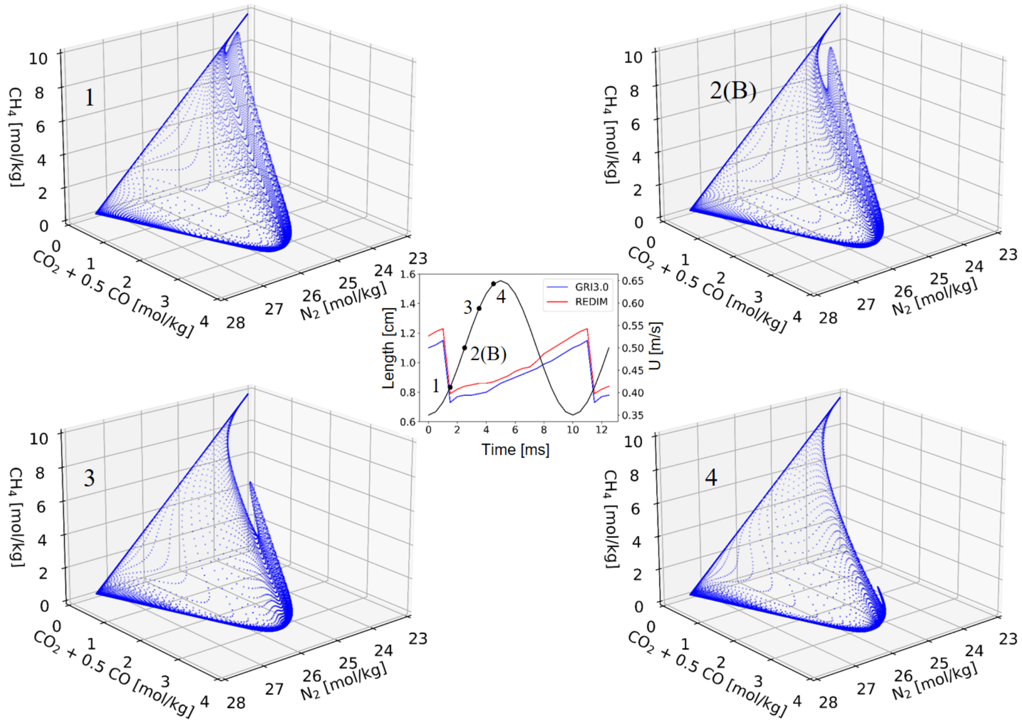

Figure 6.22: CH$_4$ specific mole number of the detailed solution projected on the specific mole number of $(\phi_{N_2}, \phi_{CO_2} + 0.5\phi_{CO})$ at 100 Hz.

cone of the flame at 100 Hz, especially for point B in Figure 6.21. It is able to effectively capture the phenomenon of fuel separation from the main jet and subsequent consumption. However, in the REDIM reduced chemistry, this portion of fuel is consumed approximately 1 ms faster than with the GRI3.0 mechanism (see Figure 6.17).

Consequently, the REDIM reduced chemistry is capable of effectively capturing the response of flame dynamics and structures induced by fuel flow oscillation across a range of frequencies (from 10 to 1000 Hz) by analyzing the results in the physical space and state space. Additionally, the REDIM yields results that have excellent agreement with the detailed mechanism for predicting the soot precursor C_2H_2, and can accurately represent its fluctuation process in response to oscillating velocity. As for the difference of peak mass fraction, future work will increase the dimension of REDIM (e.g. using a 3D REDIM) to capture the C_2H_2, which may yield better results to predict it. As such, the REDIM method is a reliable approach for simulating and predicting the behavior of combustion processes in the 2D jet flames.

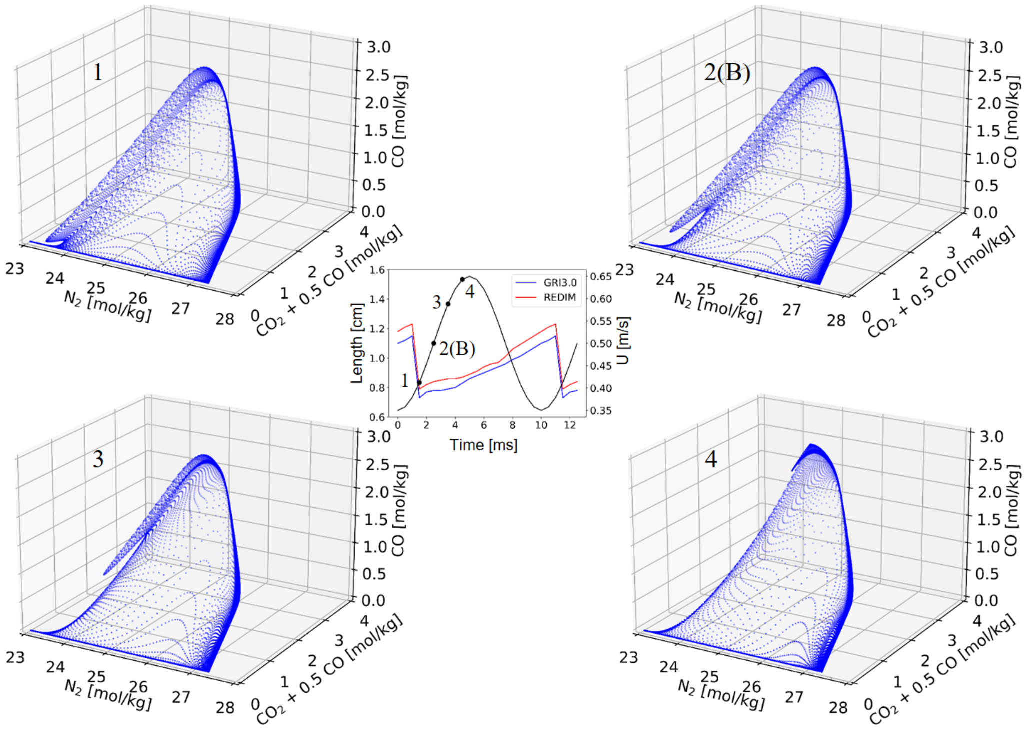

Figure 6.23: CO specific mole number of the detailed solution projected on the specific mole number of $(\phi_{\mathrm{N_2}}, \phi_{\mathrm{CO_2}} + 0.5\phi_{\mathrm{CO}})$ at 100 Hz.

7 Conclusion

In this thesis the REDIM reduced chemistry has been applied to premixed and diffusion flames. The work primarily focuses on evaluating the performance of the REDIM method in steady and transient flames. The REDIM method considers both the chemical reaction effect and the coupling of molecular transport with thermochemical processes in generating an automatically simplified chemistry, and can be applied to different combustion scenarios. Therefore, in comparison to the ILDM method, the REDIM approach can be used in simulations where convection and diffusion have a greater impact on the combustion process, specifically in the low-temperature combustion region. The results indicate that the REDIM reduced chemistry performs very well for both steady and transient processes. Remarkably, the REDIM model can effectively capture the flame dynamics, including ignition and extinction.

In chapter 4, the reliability and accuracy of the EBIdnsFoam solver are demonstrated by its calculation of a laminar coflow flame, which exhibits excellent agreement with the results reported in the literature. The REDIM method in generalized and physical coordinates has been investigated by simulating an adiabatic 1D premixed methane/air free flame. The calculated results based on generalized coordinate have excellent agreement with their corresponding results in physical coordinate, and the CPU time is almost same. Due to the efficiency and the robustness of interpolation during the implementation of REDIM in generalized coordinate, we use the REDIMFoam solver based on generalized coordinate in the thesis.

In chapter 5, the REDIM method is used as a model reduction method to calculate 2D counterflow diffusion flames. The results of the REDIM reduced model obtained with different progress variables are almost the same as the results of the detailed mechanism, which prove that the REDIM method is independent of the choice of the progress variables. Results from the REDIM method are compared for two different detailed mechanisms in the 2D counterflow flames. The REDIM reduced mechanism has good agreement with the detailed solutions, even for most of the minor species. The differences between the REDIM approach and the detailed mechanisms for the same mechanism are much smaller than the ones caused by the different mechanisms themselves. The REDIM method is used to reproduce the flame structures under different global strain rates. It is shown that the 2D REDIM can describe the flame structures of steady and quenching regimes in the 2D counterflow flames very well, while the standard steady flamelet method needs additional extinction regimes to do this.

The implementation of the REDIM reduced chemistry leads to a substantial reduction in computational effort, enabling the handling of more complex burner systems. Chapter 6 demonstrates the capability of the REDIM method to simulate the combustion process in a practical burner (2D jet flame). The phenomenon of flame liftoff has been investigated for the 2D steady and transient flames. The REDIM approach shows good agreement with the detailed mechanism, as evidenced by the temperature, selected species profiles, liftoff heights, and flame lengths computed at three different inlet velocities. The calculations presented in the thesis demonstrate that flame liftoff can result in fuel leakage, and the REDIM method can accurately capture this phenomena. The REDIM reduced chemistry is capable of capturing the flame dynamics induced by fuel flow oscillations across a range of frequencies, from 10 Hz (quasi-steady over strong coupling) up to 1000 Hz (perturbations are damped to an average value). As the frequency increases, the perturbation reaching the flame region diminishes due to the influence of frequency-dependent dissipative processes. These processes can level the oscillating velocity to an average value before reaching the flame zone. The REDIM reduced mechanism is able to effectively capture the phenomenon of fuel separation from the main jet and subsequent consumption at 100 Hz. The REDIM method can describe the variation of flame shape and local extinction rate very well. Additionally, the REDIM method yields results that show reasonable agreement with the detailed mechanism for predicting the soot precursor C_2H_2, and can correctly capture its fluctuation in response to oscillating velocity fields.

The REDIM method offers a significant reduction in computational cost compared to detailed mechanisms in 2D counterflow/jet flames. Specifically, in the 2D counterflow flames, the relative CPU time of the REDIM simulation is approximately 10 % of the CPU time with the detailed mechanism, while the value is approximately 8 % in 2D jet flames. This means that the REDIM method can significantly reduce the computational cost.

In conclusion, it can be stated that the REDIM reduced mechanism is a reliable approach for conducting precise and efficient numerical simulations of premixed or diffusion flames, and it has the potential to serve an effective tool for understanding combustion processes, as well as designing environmentally friendly and highly efficient burner systems.

Bibliography

[1] F. Birol. *World Energy Outlook*. `https://www.iea.org`. Accessed: 27.10.2022.

[2] *BP Energy Outlook 2022 edition*. `https://www.bp.com`. Accessed: 19.07.2022.

[3] S. W. Benson. *Thermochemical Kinetics*. 2nd ed. John Wiley & Sons, 1976.

[4] R. S. Cant and E. Mastorakos. *An Introduction to Turbulent Reacting Flows*. Imperial College Press, 2008.

[5] E. S. Oran and J. P. Boris. *Numerical Simulation of Reactive Flow*. 2nd ed. Cambridge University Press, 2001.

[6] J. A. Miller et al. ‘Combustion chemistry in the twenty-first century: developing theory-informed chemical kinetics models’. In: *Progress in Energy and Combustion Science* 83 (2021), p. 100886.

[7] J. Warnatz, U. Maas and R. W. Dibble. *Combustion: Physical and Chemical Fundamentals, Modeling and Simulation, Experiments, Pollutant Formation*. 4th ed. Springer, 2006.

[8] N. Peters. *Combustion theory (CEFRC Summer School)*. Lecture notes. RWTH Aachen University, 2010.

[9] A. Giusti and E. Mastorakos. ‘Turbulent combustion modelling and experiments: recent trends and developments’. In: *Flow, Turbulence and Combustion* 103.4 (2019), pp. 847–869.

[10] M. Manninen, V. Taivassalo and S. Kallio. *On the mixture model for multiphase flow*. Tech. rep. Nr. VTT-PUB-288. Technical Research Centre of Finland, 1996.

[11] T. Poinsot and D. Veynante. *Theoretical and Numerical Combustion*. 2nd ed. R.T. Edwards, Inc., 2005.

[12] S. R. Turns. *An Introduction to Combustion Concepts and Applications*. 3rd ed. McGraw-Hill, 2011.

[13] C. D. Argyropoulos and N. C. Markatos. ‘Recent advances on the numerical modelling of turbulent flows’. In: *Applied Mathematical Modelling* 39.2 (2015), pp. 693–732.

[14] A. F. Molland and S. R. Turnock. *Marine Rudders and Control Surfaces: Principles, Data, Design and Applications.* Elsevier, 2007.

[15] H. Pitsch and H. Steiner. ‘Large-eddy simulation of a turbulent piloted methane/air diffusion flame (Sandia flame D)’. In: *Physics of Fluids* 12.10 (2000), pp. 2541–2554.

[16] S. B. Pope. *Turbulent Flows.* Cambridge University Press, 2000.

[17] H. Pitsch. ‘Large-eddy simulation of turbulent combustion’. In: *Annual Review of Fluid Mechanics* 38 (2006), pp. 453–482.

[18] T. Lu and C. K. Law. ‘Toward accommodating realistic fuel chemistry in large-scale computations’. In: *Progress in Energy and Combustion Science* 35.2 (2009), pp. 192–215.

[19] O. Herbinet, W. J. Pitz and C. K. Westbrook. ‘Detailed chemical kinetic oxidation mechanism for a biodiesel surrogate’. In: *Combustion and Flame* 154.3 (2008), pp. 507–528.

[20] A. S. Tomlin et al. ‘Mechanism reduction for the oscillatory oxidation of hydrogen: Sensitivity and quasi-steady-state analyses’. In: *Combustion and Flame* 91.2 (1992), pp. 107–130.

[21] T. Turányi. ‘Reduction of large reaction mechanisms’. In: *New Journal of Chemistry* 14 (1990), pp. 795–803.

[22] S. Vajda, P. Valko and T. Turányi. ‘Principal component analysis of kinetic models’. In: *International Journal of Chemical Kinetics* 17.1 (1985), pp. 55–81.

[23] U. Maas and S. B. Pope. ‘Simplifying chemical kinetics: Intrinsic low-dimensional manifolds in composition space’. In: *Combustion and Flame* 88.3 (1992), pp. 239–264.

[24] J. A. van Oijen and L. P. H. de Goey. ‘Modelling of premixed laminar flames using flamelet-generated manifolds’. In: *Combustion Science and Technology* 161.1 (2000), pp. 113–137.

[25] A. N. Gorban and I. V. Karlin. ‘Method of invariant manifold for chemical kinetics’. In: *Chemical Engineering Science* 58.21 (2003), pp. 4751–4768.

[26] O. Gicquel, N. Darabiha and D. Thévenin. ‘Liminar premixed hydrogen/air counterflow flame simulations using flame prolongation of ILDM with differential diffusion’. In: *Proceedings of the Combustion Institute* 28.2 (2000), pp. 1901–1908.

[27] V. Bykov and U. Maas. ‘The extension of the ILDM concept to reaction–diffusion manifolds’. In: *Combustion Theory and Modelling* 11.6 (2007), pp. 839–862.

[28] V. Bykov, A. Neagos and U. Maas. ‘On transient behavior of non-premixed counter-flow diffusion flames within the REDIM based model reduction concept’. In: *Proceedings of the Combustion Institute* 34.1 (2013), pp. 197–203.

[29] A. Neagos, V. Bykov and U. Maas. ‘Study of extinction limits of diluted hydrogen-air counter-flow diffusion flames with the REDIM method’. In: *Combustion Science and Technology* 186.10-11 (2014), pp. 1502–1516.

[30] P. Golda et al. ‘Implementation problems of manifolds-based model reduction and their generic solution’. In: *Combustion Theory and Modelling* 24.3 (2020), pp. 377–406.

[31] C. Yu, F. Minuzzi and U. Maas. ‘REDIM reduced chemistry for the simulation of counterflow diffusion flames with oscillating strain rates’. In: *Combustion Theory and Modelling* 24.4 (2020), pp. 682–704.

[32] K. König, V. Bykov and U. Maas. ‘Investigation of the dynamical response of methane/air counterflow flames to inflow mixture composition and flow field perturbations’. In: *Flow, Turbulence and Combustion* 83.1 (2009), 105–129.

[33] R. De Meester et al. ‘Transported scalar PDF calculations of a swirling bluff body flame (‘SM1’) with a reaction diffusion manifold’. In: *Combustion and Flame* 159.7 (2012), pp. 2415–2429.

[34] P. Wang et al. ‘Large Eddy Simulations and experimental studies of turbulent premixed combustion near extinction’. In: *Proceedings of the Combustion Institute* 34.1 (2013), pp. 1269–1280.

[35] W. M. Pitts. ‘Importance of isothermal mixing processes to the understanding of lift-off and blowout of turbulent jet diffusion flames’. In: *Combustion and Flame* 76.2 (1989), pp. 197–212.

[36] E. J. Weber and F. E. Vandaveer. ‘Gas Burner Design’. In: *Gas Engineers Handbook*. Industrial Press, 1965. Chap. 12, pp. 193–210.

[37] W. M. Pitts. 'Assessment of theories for the behavior and blowout of lifted turbulent jet diffusion flames'. In: *Proceedings of the Combustion Institute* 22.1 (1989), pp. 809–816.

[38] K. Wohl, C. Gazley and N. Kapp. 'Diffusion flames'. In: *Symposium on Combustion and Flame, and Explosion Phenomena* 3.1 (1948), pp. 288–300.

[39] L. Vanquickenborne and A. Van Tiggelen. 'The stabilization mechanism of lifted diffusion flames'. In: *Combustion and Flame* 10.1 (1966), pp. 59–69.

[40] N. Peters. 'Local quenching due to flame stretch and non-premixed turbulent combustion'. In: *Combustion Science and Technology* 30.1-6 (1983), pp. 1–17.

[41] J. Janicka and N. Peters. 'Prediction of turbulent jet diffusion flame lift-off using a PDF transport equation'. In: *Proceedings of the Combustion Institute* 19.1 (1982), pp. 367–374.

[42] J. E. Broadwell, W. J. A. Dahm and M. G. Mungal. 'Blowout of turbulent diffusion flames'. In: *Proceedings of the Combustion Institute* 20.1 (1985), pp. 303–310.

[43] R. K. Mohammed et al. 'Computational and experimental study of a forced, time-varying, axisymmetric, laminar diffusion flame'. In: *Proceedings of the Combustion Institute* 27.1 (1998), pp. 693–702.

[44] K. C. Smyth et al. 'Greatly enhanced soot scattering in flickering CH_4/air diffusion flames'. In: *Combustion and Flame* 95.1 (1993), pp. 229–239.

[45] C. R. Shaddix, J. E. Harrington and K. C. Smyth. 'Quantitative measurements of enhanced soot production in a flickering methane/air diffusion flame'. In: *Combustion and Flame* 99.3 (1994), pp. 723–732.

[46] D. A. Everest, C. R. Shaddix and K. C. Smyth. 'Quantitative two-photon laser-induced fluorescence imaging of CO in flickering CH_4/air diffusion flames'. In: *Proceedings of the Combustion Institute* 26.1 (1996), pp. 1161–1162.

[47] N. Peters. *Turbulent Combustion.* Cambridge University Press, 2000.

[48] G. P. Smith, D. M. Golden, M. Frenklach et al. *GRI-Mech 3.0.* `http://www.me.berkeley.edu/gri_mech`. Accessed: 14.03.2010.

[49] U. Maas and J. Warnatz. 'Ignition processes in hydrogen-oxygen mixtures'. In: *Combustion and Flame* 74.1 (1988), pp. 53–69.

[50] R. J. Kee et al. *PREMIX: A Fortran program for modeling steady one-dimensional premixed flames.* Tech. rep. Nr. SAND85-8240. Sandia National Laboratories, 1985.

[51] R. J. Kee, J .A. Miller and T. H. Jefferson. *CHEMKIN: A general-purpose, problem-independent, transportable, Fortran chemical kinetics code package.* Tech. rep. Nr. SAND80-8003. Sandia National Laboratories, 1980.

[52] D. G. Goodwin et al. *Cantera: An object-oriented software toolkit for chemical kinetics, thermodynamics, and transport processes.* `https://www.cantera.org`. Version 2.2.1. 2016.

[53] C. J. Greenshields. *OpenFOAM User Guide.* `https://cfd.direct/openfoam`. Version 7. 2019.

[54] H. Tsuji. 'Counterflow diffusion flames'. In: *Progress in Energy and Combustion Science* 8.2 (1982), pp. 93–119.

[55] H. Tsuji and I. Yamaoka. 'The counterflow diffusion flame in the forward stagnation region of a porous cylinder'. In: *Proceedings of the Combustion Institute* 11.1 (1967), pp. 979–984.

[56] W. A. Hahn and J. O. L. Wendt. 'The flat laminar opposed jet diffusion flame: a novel tool for kinetic studies of trace species formation'. In: *Chemical Engineering Communications* 9.1-6 (1981), pp. 121–136.

[57] G. Dixon-Lewis et al. 'Calculation of the structure and extinction limit of a methane-air counterflow diffusion flame in the forward stagnation region of a porous cylinder'. In: *Proceedings of the Combustion Institute* 20.1 (1985), pp. 1893–1904.

[58] M. D. Smooke and V. Giovangigli. 'Numerical modeling of axisymmetric laminar diffusion flames'. In: *IMPACT of Computing in Science and Engineering* 4.1 (1992), pp. 46–79.

[59] T. Holzmann. *Mathematics, Numerics, Derivations and OpenFOAM(R).* `https://Holzmann-cfd.de`. Version 7. 2021.

[60] R. B. Bird, W. E. Stewart and E. N. Lightfoot. *Transport Phenomena.* John Wiley & Sons, 2006.

[61] F. Moukalled, L. Mangani and M. Darwish. *The Finite Volume Method in Computational Fluid Dynamics: An Advanced Introduction with OpenFOAM and Matlab.* Springer, 2015.

[62] R. J. LeVeque. *Finite Volume Methods for Hyperbolic Problems.* Cambridge University Press, 2002.

[63] H. Jasak. 'Error analysis and estimation for finite volume method with applications to fluid flow'. PhD thesis. Imperial College London (University of London), 1996.

[64] S. V. Patankar. *Numerical Heat Transfer and Fluid Flow.* Hemisphere Publishing Corporation, 1980.

[65] R. I. Issa. 'Solution of the implicitly discretised fluid flow equations by operator-splitting'. In: *Journal of Computational Physics* 62.1 (1985), pp. 40–65.

[66] R. Courant, K. Friedrichs and H. Lewy. 'Über die partiellen Differenzengleichungen der mathematischen Physik'. In: *Mathematische Annalen* 100.1 (1928), pp. 32–74.

[67] M. J. Pilling. *Low-temperature Combustion and Autoignition.* Elsevier, 1997.

[68] S. Arrhenius. 'Über die Reaktionsgeschwindigkeit bei der Inversion von Rohrzucker durch Säuren'. In: *Zeitschrift für physikalische Chemie* 4.1 (1889), pp. 226–248.

[69] F.A. Williams. *Combustion Theory.* 2nd ed. Westview Press, 1985.

[70] M. Rein. 'The partial-equilibrium approximation in reacting flows'. In: *Physics of Fluids A* 4.5 (1992), pp. 873–886.

[71] C. W. Pyun. 'Steady-state and equilibrium approximations in chemical kinetics'. In: *Journal of Chemical Education* 48.3 (1971), pp. 194–196.

[72] J. Bauer, V. Bykov and U. Maas. 'Implementation of ILDMs based on a representation in generalized coordinate'. In: *European Conference on Computational Fluid Dynamics, ECCOMAS CFD 2006.* Egmond aan Zee, The Netherlands, 2006, pp. 5–8.

[73] G. H. Golub and C. F. Van Loan. *Matrix Computations.* 2nd ed. John Hopkins University Press, 1989.

[74] U. Maas. 'Efficient calculation of intrinsic low-dimensional manifolds for the simplification of chemical kinetics'. In: *Computing and Visualization in Science* 1.2 (1998), pp. 69–81.

[75] U. Maas and S. B. Pope. 'Implementation of simplified chemical kinetics based on intrinsic low-dimensional manifolds'. In: *Proceedings of the Combustion Institute* 24.1 (1992), pp. 103–112.

[76] S. B. Pope and U. Maas. *Simplifying chemical kinetics: trajectory-generated low-dimensional manifolds.* Tech. rep. Nr. FDA 93-11. Cornell University, 1993.

[77] R. L. G. M. Eggels et al. ‘Comparison of conventional and low-dimensional manifold methods to reduce reaction mechanisms’. In: *Combustion science and technology* 123.1-6 (1997), pp. 347–362.

[78] M. J. Davis and R. T. Skodje. ‘Geometric investigation of low-dimensional manifolds in systems approaching equilibrium’. In: *Journal of Chemical Physics* 111.3 (1999), pp. 859–874.

[79] S. S. Girimaji and A. A Ibrahim. ‘Advanced quasi-steady state approximation for chemical kinetics’. In: *Journal of Fluids Engineering* 136.3 (2011), p. 031201.

[80] D. Schmidt, T. Blasenbrey and U. Maas. ‘Intrinsic low-dimensional manifolds of strained and unstrained flames’. In: *Combustion Theory and Modelling* 2.2 (1998), pp. 135–152.

[81] V. Bykov and U. Maas. ‘Extension of the ILDM method to the domain of slow chemistry’. In: *Proceedings of the Combustion Institute* 31.1 (2007), pp. 465–472.

[82] H. Bongers et al. ‘The flamelet generated manifold method applied to steady planar partially permixed counterflow flames’. In: *Combustion Science and Technology* 177.12 (2005), pp. 2373–2393.

[83] P. Nguyen et al. ‘Multidimensional flamelet-generated manifolds for partially premixed combustion’. In: *Combustion and Flame* 157.1 (2010), pp. 43–61.

[84] E. Knudsen and H. Pitsch. ‘Capabilities and limitations of multi-regime flamelet combustion models’. In: *Combustion and Flame* 159.1 (2012), pp. 242–264.

[85] X. Wen et al. ‘A generalized flamelet tabulation method for partially premixed combustion’. In: *Combustion and Flame* 198 (2018), pp. 54–68.

[86] B. Franzelli, B. Fiorina and N. Darabiha. ‘A tabulated chemistry method for spray combustion’. In: *Proceedings of the Combustion Institute* 34.1 (2013), pp. 1659–1666.

[87] D. A. Goussis and U. Maas. ‘Model Reduction for Combustion Chemistry’. In: *Turbulent Combustion Modeling: Advances, New Trends and Perspectives.* Springer, 2011. Chap. 9, pp. 193–220.

[88] Z. Ren et al. ‘Application of the ICE-PIC method for the dimension reduction of chemical kinetics coupled with transport’. In: *Proceedings of the Combustion Institute* 31.1 (2007), pp. 473–481.

[89] U. Maas and V. Bykov. 'The extension of the reaction/diffusion manifold concept to systems with detailed transport models'. In: *Proceedings of the Combustion Institute* 33.1 (2011), pp. 1253–1259.

[90] V. Bykov et al. 'Hierarchical structure of slow manifolds of reacting flows'. In: *Zeitschrift für Physikalische Chemie* 229.6 (2015), pp. 833–856.

[91] C. Yu. 'Numerical simulation of turbulent flames based on reaction-diffusion manifolds (REDIM) reduced chemistry'. PhD thesis. Karlsruhe Institute of Technology, 2020.

[92] V. Bykov and U. Maas. 'Problem adapted reduced models based on reaction-diffusion manifolds (REDIMs)'. In: *Proceedings of the Combustion Institute* 32.1 (2009), pp. 561–568.

[93] C. Strassacker, V. Bykov and U. Maas. 'REDIM reduced modeling of flame quenching at a cold wall – the influence of detailed transport models and detailed mechanisms'. In: *Combustion Science and Technology* 191.2 (2019), pp. 208–222.

[94] R. Schießl et al. 'Implementing multi-directional molecular diffusion terms into reaction diffusion manifolds (REDIMs)'. In: *Proceedings of the Combustion Institute* 36.1 (2017), pp. 673–679.

[95] G. Steinhilber and U. Maas. 'Reaction-diffusion manifolds for unconfined, lean premixed, piloted, turbulent methane/air systems'. In: *Proceedings of the Combustion Institute* 34.1 (2013), pp. 217–224.

[96] A. Neagos, V. Bykov and U. Maas. 'Adaptive hierarchical construction of reaction-diffusion manifolds for simplified chemical kinetics'. In: *Proceedings of the Combustion Institute* 36.1 (2017), pp. 663–672.

[97] G. Stahl and J. Warnatz. 'Numerical investigation of time-dependent properties and extinction of strained methane and propane-air flamelets'. In: *Combustion and Flame* 85.3-4 (1991), pp. 285–299.

[98] T. Zirwes et al. 'Quasi-DNS Dataset of a piloted flame with inhomogeneous inlet conditions'. In: *Flow, Turbulence and Combustion* 104.4 (2020), pp. 997–1027.

[99] T. Zirwes. 'Memory effects in premixed flames: unraveling transient flame dynamics with the flame particle tracking method'. PhD thesis. Karlsruhe Institute of Technology, 2021.

[100] T. Zirwes et al. 'Assessment of numerical accuracy and parallel performance of OpenFOAM and its reacting flow extension EBIdnsFoam'. In: *Flow, Turbulence and Combustion* 111.2 (2023), pp. 567–602.

[101] H. Bonart. 'Implementation and validation of a solver for direct numerical simulations of turbulent reacting flows in OpenFOAM'. Bachelor thesis. Karlsruhe Institute of Technology, 2012.

[102] *SUNDIALS: A suite of nonlinear and differential/algebraic equation solvers.* `https://computing.llnl.gov/projects/sundials/cvode`. Accessed: 02.07.2016.

[103] J. O. Hirschfelder, C. F. Curtiss and R. B. Bird. *Molecular Theory of Gases and Liquids.* John Wiley & Sons, 1964.

[104] B. J. McBride, S. Gordon and M. A. Reno. *Coefficients for calculating thermodynamic and transport properties of individual species.* Tech. rep. Nr. 4513. National Aeronautics and Space Administration, 1993.

[105] T. Zirwes et al. *Manual for the EBI-DNS Solver.* Tech. rep. Engler-Bunte-Institute, Karlsruhe Institute of Technology, 2020.

[106] B. A. V. Bennett and M. D. Smooke. 'Local rectangular refinement with application to axisymmetric laminar flames'. In: *Combustion Theory and Modelling* 2.3 (1998), pp. 221–258.

[107] B. A. V. Bennett et al. 'Computational and experimental study of oxygen-enhanced axisymmetric laminar methane flames'. In: *Combustion Theory and Modelling* 12.3 (2008), pp. 497–527.

[108] R. J. Hall. 'The radiative source term for plane-parallel layers of reacting combustion gases'. In: *Journal of Quantitative Spectroscopy and Radiative Transfer* 49.5 (1993), pp. 517–523.

[109] R J. Hall. 'Radiative dissipation in planar gas-soot mixtures'. In: *Journal of Quantitative Spectroscopy and Radiative Transfer* 51.4 (1994), pp. 635–644.

[110] W. L. Grosshandler. *RADCAL: A narrow-band model for radiation calculations in a combustion environment.* Tech. rep. Nr. 1402. National Institute of Standards and Technology, 1993.

[111] J. Nafe and U. Maas. 'A general algorithm for improving ILDMs'. In: *Combustion Theory and Modelling* 6.4 (2002), pp. 697–709.

[112] *OpenFOAM: The open source CFD toolbox.* `https://www.openfoam.com`. Accessed: 30.06.2020.

[113] P. H. de Almeida Konzen et al. 'Implementation of REDIM reduced chemistry to model an axisymmetric laminar diffusion methane–air flame'. In: *Combustion Theory and Modelling* 15.3 (2011), pp. 299–323.

[114] B. Merci et al. 'Joint scalar PDF simulations of a bluff-body stabilised flame with the REDIM approach'. In: *4th European Combustion Meeting*. Vienna, Austria, 2009.

[115] C. Strassacker, V. Bykov and U. Maas. 'Parametrization and projection strategies for manifold based reduced kinetic models'. In: *Proceedings of the Combustion Institute* 37.1 (2019), pp. 763–770.

[116] U. Prüfert et al. 'A constrained control approach for the automated choice of an optimal progress variable for chemistry tabulation'. In: *Flow, Turbulence and Combustion* 94.3 (2015), pp. 593–617.

[117] A. H. D. Cheng and D. T. Cheng. 'Heritage and early history of the boundary element method'. In: *Engineering Analysis with Boundary Elements* 29.3 (2005), pp. 268–302.

[118] *Chemical-kinetic mechanisms for combustion applications*. San Diego Mechanism web page, Mechanical and Aerospace Engineering (Combustion Research), University of California at San Diego. Accessed: 04.10.2014; Available online: `http://combustion.ucsd.edu`. 2014.

[119] R. S. Barlow et al. 'Piloted methane/air jet flames: transport effects and aspects of scalar structure'. In: *Combustion and Flame* 143.4 (2005), pp. 433–449.

[120] M. Bundy, A. Hamins and K. Y. Lee. 'Suppression limits of low strain rate non-premixed methane flames'. In: *Combustion and Flame* 133.3 (2003), pp. 299–310.

[121] C. B. Oh et al. 'The two-dimensional structure of low strain rate counterflow nonpremixed-methane flames in normal and microgravity'. In: *Combustion Theory and Modelling* 12.2 (2008), pp. 283–302.

[122] H. Pitsch. 'Unsteady flamelet modeling of differential diffusion in turbulent jet diffusion flames'. In: *Combustion and Flame* 123.3 (2000), pp. 358–374.

[123] A. Kronenburg and A. E. Papoutsakis. 'Conditional moment closure modeling of extinction and re-ignition in turbulent non-premixed flames'. In: *Proceedings of the Combustion Institute* 30.1 (2005), pp. 759–766.

[124] H. K. Chelliah et al. ‘An experimental and theoretical investigation of the dilution, pressure and flow-field effects on the extinction condition of methane-air-nitrogen diffusion flames’. In: *Proceedings of the Combustion Institute* 23.1 (1991), pp. 503–511.

[125] R. E. Mitchell, A. F. Sarofim and L. A. Clomburg. ‘Experimental and numerical investigation of confined laminar diffusion flames’. In: *Combustion and flame* 37 (1980), pp. 227–244.

[126] M. D. Smooke, R. E. Mitchell and D. E. Keyes. ‘Numerical solution of two-dimensional axisymmetric laminar diffusion flames’. In: *Combustion Science and Technology* 67.4-6 (1989), pp. 85–122.

[127] A. Cuoci et al. ‘A computational tool for the detailed kinetic modeling of laminar flames: application to C_2H_4/CH_4 coflow flames’. In: *Combustion and Flame* 160.5 (2013), pp. 870–886.

[128] S. Cao et al. ‘Effects of pressure and fuel dilution on coflow laminar methane–air diffusion flames: a computational and experimental study’. In: *Combustion Theory and Modelling* 22.2 (2018), pp. 316–337.

[129] B. A. V. Bennett et al. ‘Computational and experimental study of axisymmetric coflow partially premixed ethylene/air flames’. In: *Combustion and Flame* 127.1 (2001), pp. 2004–2022.

[130] N. Li et al. ‘Application of reaction-diffusion manifolds (REDIM) for the simulation of two-dimensional axisymmetric laminar diffusion flames’. In: *10th European Combustion Meeting.* Napoli, Italy, 2021.

[131] M. D. Smooke et al. ‘Computational and experimental study of NO in an axisymmetric laminar diffusion flame’. In: *Proceedings of the Combustion Institute* 26.2 (1996), pp. 2161–2170.

[132] M. D. Smooke et al. ‘Computational and experimental study of OH and CH radicals in axisymmetric laminar diffusion flames’. In: *Proceedings of the Combustion Institute* 24.1 (1992), pp. 813–821.

[133] F. G. Roper. ‘The prediction of laminar jet diffusion flame sizes: Part I. Theoretical model’. In: *Combustion and Flame* 29 (1977), pp. 219–226.

[134] S. B. Dworkin et al. ‘Computational and experimental study of a forced, time-dependent, methane-air coflow diffusion flame’. In: *Proceedings of the Combustion Institute* 31.1 (2007), pp. 971–978.

[135] N. Li, T. Zirwes and U. Maas. ‘Application of reaction-diffusion manifolds (REDIM) to an oscillating methane-air jet diffusion flame’. In: *Submitted to Proceedings of the Combustion Institute* (2024).

List of publications

Journal publications

N. Li, T. Zirwes and U. Maas. ‘Application of reaction-diffusion manifolds (REDIM) to an oscillating methane-air jet diffusion flame’. In: *Submitted to Proceedings of the Combustion Institute*, Milan, Italy, 2024.

N. Li, V. Bykov, T. Zirwes, A. Moroshkina, E. Sereshchenko and V. Gubernov. ‘Secondary diffusion flame suppression by co-flows in oscillating burner-stabilized methane-air flames’. In: *Submitted to Proceedings of the Combustion Institute*, Milan, Italy, 2024.

Conference publications

N. Li, C. Yu, T. Zirwes and U. Maas. ‘Application of reaction-diffusion manifolds (REDIM) for the simulation of two-dimensional axisymmetric laminar diffusion flames’. In: *10th European Combustion Meeting*, Napoli, Italy, 2021.